ABSTRACT

EXPERIMENTAL AND MODELING STUDIES IN MEMBRANE DISTILLATION

by
Lin Li

A variety of microporous hydrophobic flat sheet membranes of polyvinylidene fluoride (PVDF) and expanded-polytetrafluoroethylene (e-PTFE) are studied to evaluate the influence of membrane properties on their performance in desalination by direct contact membrane distillation (DCMD) and vacuum membrane distillation (VMD) processes. The membrane thickness is varied between 23 μm to 125 μm; the pore size is varied from 0.05 μm to 0.45 μm. The porosity is generally high in the range of 0.7 - 0.8. DCMD experiments are performed over a hot brine temperature range of 65 ℃ to 85 ℃ and distillate temperature at 25 ℃ for various brine flow rates and distillate flow rates in a circular stainless steel cell and a rectangular chlorinated polyvinyl chloride (CPVC) cell. Boundary layer heat transfer resistances in the membrane cell on both sides of the membrane and the two membrane surface temperatures are determined from the experimental data over a range of hot brine and cold distillate flow rates by the Wilson plot technique. Membrane properties such as the maximum pore size and tortuosity are characterized and employed in checking out model assumptions and model results for water vapor transport in the Knudsen regime and the transition region. Good agreements (within 5% deviation) of the membrane mass transfer coefficient of water vapor and the observed water vapor fluxes are obtained between the experimental values and the

simulated results predicted for either the Knudsen regime or the transition region. Pore size distribution (PSD) does not matter if the membrane pore size variation falls entirely in the Knudsen diffusion or the transition regime. However, for membranes having nominal pore size ≅ 0.1 μm, K_n ≅ 1, PSD plays an important role in DCMD. The effects of membrane thickness on water vapor flux and thermal efficiency are also simulated and compared with the experimental results. The same membranes are studied in the CPVC cell for VMD behavior using the Wilson plot method over a hot brine temperature range of 65 ℃ to 85 ℃ for various feed flow rates and various vacuum levels. Liquid entry pressure (LEP) is experimentally determined. Water vapor fluxes are predicted and compared using two models: the Knudsen diffusion and the dusty-gas model (DGM). The deviation between the two models is within 1.3%. Knudsen diffusion is the dominant regime in VMD transport since the values of Knudsen number, K_n, for all membranes are larger than 1 at all temperatures. The boundary layer heat transfer resistance in the membrane cell and the membrane surface temperature are determined from experimental data via Wilson plot. Good agreements of membrane mass transfer coefficients and water vapor fluxes are found between the DGM simulations and the experimental results (deviation within 5%). The performance estimates for larger hollow fiber-based MD devices are also analyzed using mathematical models developed and numerically solved in MATLAB.

EXPERIMENTAL AND MODELING STUDIES IN MEMBRANE DISTILLATION

by
Lin Li

A Dissertation
Submitted to the Faculty of
New Jersey Institute of Technology
in Partial Fulfillment of the Requirements for the Degree of
Doctor of Philosophy in Chemical Engineering

Otto H. York Department of
Chemical, Biological and Pharmaceutical Engineering

May 2016

.

APPROVAL PAGE

EXPERIMENTAL AND MODELING STUDIES IN MEMBRANE DISTILLATION

Lin Li

Dr. Kamalesh Sirkar, Dissertation Advisor Date
Distinguished Professor of Chemical, Biological, and Pharmaceutical Engineering, NJIT

Dr. Piero Armenante, Committee Member Date
Distinguished Professor of Chemical, Biological, and Pharmaceutical Engineering, NJIT

Dr. Boris Khusid, Committee Member Date
Professor of Chemical, Biological, and Pharmaceutical Engineering, NJIT

Dr. Sagnik Basuray, Committee Member Date
Assistant Professor of Chemical, Biological, and Pharmaceutical Engineering, NJIT

Dr. Wen Zhang, Committee Member Date
Assistant Professor of Civil and Environmental Engineering, NJIT

BIOGRAPHICAL SKETCH

Author: Lin Li

Degree: Doctor of Philosophy

Date: May 2016

Undergraduate and Graduate Education:

- Doctor of Philosophy in Chemical Engineering,
  New Jersey Institute of Technology, Newark, NJ, 2016

- Master of Science in Pharmaceutical Engineering,
  New Jersey Institute of Technology, Newark, NJ, 2012

- Bachelor of Science in Pharmacy,
  Zhejiang University, Zhejiang, P. R. China, 2010

Major: Chemical Engineering

Presentations and Publications:

Lin Li, Kamalesh K Sirkar. Influence of Microporous Membrane Properties on the Desalination Performance in Direct Contact Membrane Distillation, manuscript accepted by Journal of Membrane Science. DOI: http://dx.doi.org/10.1016/j.memsci.2016.04.015.

Lin Li, Kamalesh K Sirkar. Studies in Vacuum Membrane Distillation with Flat Membranes, manuscript submitted for publication.

Lin Li, Kamalesh K Sirkar. Influence of Microporous Membrane Properties on DCMD, oral presentation, AIChE (American Institute of Chemical Engineers) Annual Meeting, Salt Lake city, Utah, November 2015.

Lin Li, Kamalesh K Sirkar. Influence of Microporous Membrane Properties on DCMD, poster presentation, NAMS (North America Membrane Society) 25th Annual Meeting, Boston, Massachusetts, June 2015.

To my father, Xinzhao; my mother, Yunlan; and my boyfriend, Bo;
for their encouragement, infinite love and support.

致
我的父亲，李新钊
我的母亲，徐云兰
谢谢你们无尽的爱
抚养我长大
培养我成才
你们是最伟大的人

致
我的男友，张渤
谢谢你的鼓励和耐心
你是我最好的朋友

ACKNOWLEDGMENT

I would like to express my deep sense of gratitude to my advisor, Professor Kamalesh Sirkar for providing me patient guidance and mentorship, all the way from beginning of my Ph.D. degree to completion of this research. Without his immense knowledge and guidance, this dissertation would not have been possible.

I also would like to thank the members of my dissertation committee, Prof. Piero Armenante, Prof. Boris Khusid, Prof. Sagnik Basuray and Prof. Wen Zhang for their constructive criticism and invaluable mentorship throughout different stages in carrying out this research.

Further thanks are needed to be given to the Center of Membrane Technology at NJIT, National Science Foundation, Membrane Science, Engineering & Technology Center (MAST Center), US Bureau of Reclamation, for providing me research opportunities. I acknowledge the research assistantship awarded to me by MAST #13-1 project and US Bureau of Reclamation contact to NJIT.

Finally, I would like to thank Dr. Gordana Obuskovic, Dr. Dhananjay Singh, Dr. John Chau, Dr. John Tang, Dr. Tripula Mulukutla, Jose Sousa and Na Yao for all their help and support.

TABLE OF CONTENTS

TABLE OF CONTENTS
(Continued)

Chapter **Page**

TABLE OF CONTENTS
(Continued)

Chapter **Page**

TABLE OF CONTENTS
(Continued)

Chapter **Page**

TABLE OF CONTENTS
(Continued)

Chapter **Page**

LIST OF TABLES

LIST OF TABLES
(Continued)

Table **Page**

LIST OF FIGURES

LIST OF FIGURES
(Continued)

Figure **Page**

LIST OF FIGURES
(Continued)

Figure **Page**

LIST OF FIGURES
(Continued)

LIST OF FIGURES
(Continued)

LIST OF SYMBOLS

A_m	membrane area (m^2)
A_{rf}	membrane area ratio for heat transfer through fiber outside surface ($=d_o/d_i$)
A_{rln}	membrane area ratio for heat/mass transfer through the fiber based on logarithmic mean diameter-based surface ($=d_{lm}/d_i$)
A_{rp}	membrane area ratio for heat transfer through fiber inside surface ($=d_i/d_i$)
b	constant, defined in Eq.(2.29)
C_p	heat capacity of water (J/K-g)
C_{pb}	heat capacity of brine (J/K-g)
C_v	heat capacity of water vapor (J/K-g)
D_{CO2}	diffusivity of CO_2 through water (m^2/s)
D_{Kn}	Knudsen diffusivity (m^2/s)
D_{w-a}	diffusion coefficient of water vapor and air (m^2/s)
d_i	fiber inside diameter (m)
d_{lm}	logarithmic mean diameter of fiber (m)
d_M	membrane pore diameter (μm)
d_{max}	maximum membrane pore size (μm)
d_o	fiber outside diameter (m)
d_p	nominal membrane pore diameter (μm)

LIST OF SYMBOLS

F	volumetric liquid flow rate (mL/min)
F_c	correction factor
H_f	hollow fiber module frame height
$H_v(T)$	Enthalpy of water vapor (kJ/kg)
h	heat transfer coefficient (W/m^2-K)
h_m	membrane heat transfer coefficient (W/m^2-K)
h_{mg}	heat transfer coefficient across the membrane pore gas phase (W/m^2-K)
h_{ms}	heat transfer coefficient for the solid polymeric matrix (W/m^2-K)
J	water vapor flux (kg/m^2-h)
K_n	Knudsen number
K_0	function of membrane properties
k_B	Boltzmann's constant (J/K)
k_m	membrane mass transfer coefficient (kg/m^2-h-Pa)
k_{mt}	thermal conductivity (W/m-K)
k_v	thermal conductivity of gas in the membrane pores (W/m-K)
L	fiber total length (m)
L_f	hollow fiber module frame length

LIST OF SYMBOLS

M	molecular weight (kg/mol)
m	number of fiber layers
n	fiber number per layer
N	total fiber numbers
N_v	water vapor flux (kg/(m^2 -h))
P_{BP}	bubble point pressure (Pa)
p_{fm}	water vapor partial pressure at the membrane surface on the shell side (Pa)
P_m	mean partial pressure of water vapor on two sides of membrane
p_{pm}	water vapor partial pressure at the membrane surface on the tube side (Pa)
P_T	total pressure in the membrane pore (Pa)
$P_{w,1}$	water vapor partial pressure on the feed side of the membrane surface (Pa)
$P_{w,2}$	water vapor partial pressure on the distillate side of the membrane surface (Pa)
P_v	vacuum pressure (Pa)
P_1^0	actual water vapor pressure
Pr	Prandtl number (C_p/k)
Q	rate of heat transfer (J/min)
Q_{co2}	permeability of the soluble CO_2 through water in the pores (m^3(STP)-m/ m^2-s-Pa)

LIST OF SYMBOLS

q	heat flux (W/m^2)
q_m	heat flux through membrane (W/m^2)
q^t	total heat flux (W/m^2)
R	gas constant (J/mol-K)
Re	Reynolds number
R_{CO2}	volumetric permeation rate of the CO_2 (m^3(STP)/s)
R_{total}	volumetric permeation rate of total gas (m^3(STP)/s)
S_{CO2}	solubility of CO_2 in pure water ($mol/m^3/Pa$)
T	temperature (K)
T_{bi}	brine inlet temperature (K)
T_{b0}	brine feed temperature (℃)
T_{d0}	distillate feed temperature (℃)
T_{di}	distillate inlet temperature (℃)
T_{do}	distillate outlet temperature (℃)
T_f	brine bulk temperature (℃)
T_{f0}	brine feed temperature (◦C)
T_{fm}	brine temperature at the hollow fiber membrane surface (℃)
T_p	distillate bulk temperature (℃)

LIST OF SYMBOLS

x	length along membrane thickness, position along the fiber length
x_w	mole fraction of water on the membrane surface
T_{p0}	distillate feed temperature for one layer (℃)
T_{p1}	distillate outlet temperature for one layer (℃)
T_{pm}	distillate temperature at the hollow fiber membrane surface (℃)
T_0	reference temperature (273.15 K, 0 ℃)
T_1	membrane surface temperature on the feed side (K)
T_2	membrane surface temperature on the distillate side (K)
T_m	membrane mean surface temperature (K)
v	flow velocity (m/s)
v_I	interstitial velocity on shell side (m/s)
v_L	linear velocity on tube side (m/s)
V_{b0}	brine inlet volumetric flow rate (L/min)
V_{b1}	brine outlet volumetric flow rate (L/min)
V'_{f0}	local brine inlet volumetric flowrate per unit length of fiber (L/(m-min))
V'_{f1}	local brine outlet volumetric flow rate per unit length of fiber (L/(m-min))
V_{d0}	distillate inlet volumetric flow rate (L/min)
V_{d1}	distillate outlet volumetric flow rate (L/min)
V_{p0}	distillate inlet volumetric flow rate for one fiber layer (L/min)

LIST OF SYMBOLS

V_{p1} distillate outlet volumetric flow rate for one fiber layer (L/min)

W_f hollow fiber module frame width (cm)

Greek letters

α effect of air flux

γ surface tension of IPA (0.0217 N/m at 20 ℃)

γ_w activity coefficient of water on the membrane surface

ΔP_{CO2} partial pressure difference of CO_2 on two sides of the membrane (Pa)

δ_M membrane thickness (m)

ε_M membrane porosity

η thermal efficiency

θ contact angle between IPA and the membrane surface

μ water vapor viscosity

λ mean free path (m)

λ_w mean free path of water vapor (m)

λ_H latent heat of water vapor (2260 kJ/kg)

ρ liquid density (kg/m^3)

χ_M membrane tortuosity

LIST OF SYMBOLS

1	outlet (flow rate, temperature, density, heat capacity)
b	brine
d	distillate
f	feed, frame
i	inlet
j	the jth fiber layer
o	outlet
p	distillate or fiber lumen side
m	mean, membrane
s	polymer
t	total
v	water vapor
w-a	water vapor and air

Superscripts

m	constant, defined in Eq.(2.29)
n	constant in Eq.(2.27)

CHAPTER 1

INTRODUCTION

This dissertation is concerned with experimental and modeling studies in membrane distillation (MD), specifically direct contact membrane distillation (DCMD) and vacuum membrane distillation (VMD). A brief introduction to four different membrane distillation techniques will be provided first. It will be followed by a description of various types of membrane modules and membranes used for MD techniques and the characterization methods adopted to determine various membrane properties. Then the objectives of this dissertation will be described and deliberated on.

1.1 Background Information

Membrane separation technologies are very important in separation and purification activities undertaken in industrial operations. Ultrafiltration, microfiltration and reverse osmosis (RO) are now standard unit operations in process industries. Dialysis is widely used in the medical field. Membrane separation processes can be divided into four categories depending on the driving force employed for selective membrane transport: pressure difference, concentration difference, temperature difference and electrical potential difference.

Membrane distillation (MD) is a thermally-driven membrane separation process. A major application of MD is desalination, because there is minimal amount of volatile solute in salt water, and the permeate purity will be high. It has gained interest among modern separation technologies for its capability in water purification utilizing renewable energies. A considerable number of studies have been conducted and are being conducted in membrane distillation in order to successfully compete with conventional desalination technologies, namely RO and multi-stage flash distillation (MSF).

1.1.1 MD Variations and Applications

In the membrane distillation process for desalination, hot brine is passed on one side of a porous hydrophobic membrane. Liquid penetration into membrane pores can be prevented if the surface tension of the liquid is higher than the critical surface tension of the membrane polymer. Evaporation occurs when the thermal motion of a water molecule in brine overcomes the liquid surface tension. Vapor-liquid equilibrium occurs at every pore entrance at the membrane surface. The vapor pressure of water at hot brine–membrane pore interface is much higher than that at the condenser surface; it results in pure water vapor diffusion from one side of the membrane to the other side. The partial pressure difference of water vapor between two sides of the membrane is the driving force for water vapor transfer. Higher temperature and/or brine side flow rates, results in a higher driving force and higher evaporation rate.

There are four types of the condenser surfaces to recover pure water vapor, which defines four types of MD technologies (Figure 1.1):

1.1.1.1 DCMD. In direct contact MD (DCMD), hot brine passing over one side of a porous hydrophobic membrane creates a surface for vaporization of water, while cold distillate is passed over the other side of the membrane creating condensation of this water vapor (Figure 1a). Vapor liquid interface occurs at every entrance of the membrane pores as a result of the hydrophobic nature of the porous membrane. The difference in water vapor partial pressure due to temperature difference on both sides of the membrane is the driving force for water vapor transfer. DCMD is the simplest MD configuration, and is widely employed in desalination processes [1]. The main drawback of DCMD is that some of the brine heat is lost by conduction across the membrane and is therefore not available for evaporation.

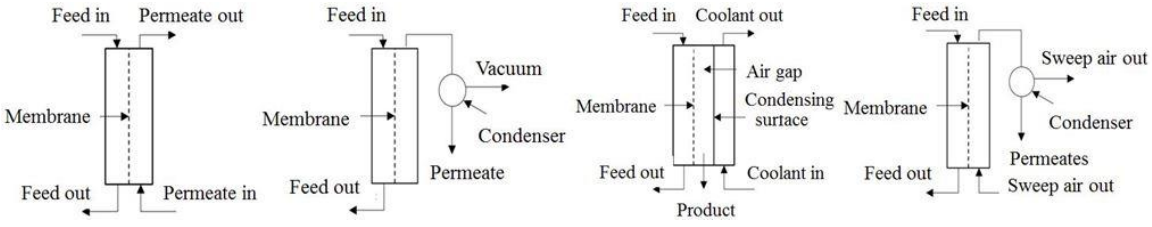

Figure 1.1 Four types of membrane distillation (MD): (a) Direct contact MD (DCMD); (b) Vacuum MD (VMD); (c) Air gap MD (AGMD); (d) Sweep gas MD (SGMD).

1.1.1.2 VMD. In Vacuum MD (VMD), a vacuum pump is used to create vacuum in the permeate membrane side (Figure 1b). Condensation takes place outside the membrane module. The heat loss due to conduction across the membrane is minimal in VMD; higher water vapor flux can be achieved if a sufficiently high vacuum level is applied to the permeate side [2–4]. Extensive studies have been conducted in the past for various applications in VMD mostly in desalination but also in processes such as ethanol/water separation, removal of trace gases and volatile organic compounds (VOCs) from water. One of the major deficiencies of current VMD technologies is lacking of guidance on the membrane properties and operating conditions for optimum performance of water vapor flux and energy consumption.

1.1.1.3 AGMD. Figure 1.1c shows the schematic of air gap MD (AGMD); water vapor is condensed on a cold surface separated by a thin air gap [5,6]. The feed solution is in direct contact with the hot side of the membrane surface. Stagnant air exists between the membrane and the condensation surface. The vapor crosses the air gap to condense over the cold surface inside the membrane cell. The benefit of this design is reduced heat loss by conduction. Further, the cold surface can be cooled by brine itself. This removes the need for distilled water (needed in DCMD). However, the air gap creates additional resistance to mass transfer; the air gap thickness is a critical factor that controls MD performances and yet it is not variable.

1.1.1.4 SGMD. Figure 1.1d represents sweep gas MD (SGMD); an inert gas (e.g., air) is used to sweep the water vapor at the permeate membrane side to condense outside

the membrane module [7]. The inert gas serves as a gas barrier between the feed surface and the condenser surface to reduce the heat loss. Unlike AGMD, this gas barrier is not stationary, which enhances the mass transfer coefficient. The main disadvantage of this configuration is that a small volume of permeate diffuses into a large inert sweep gas volume which needs a large external condenser to recover water vapor by condensation.

Membrane distillation process has a number of potential advantages, namely, low operating temperature and hydraulic pressure, high rejection of non-volatile solutes, smaller footprint and potentially high permeate flux, for example in DCMD compared to that in conventional thermal separation processes. For such reasons, MD has been considered as an emerging desalination technology for producing fresh water from brines. A most important advantage of MD technique over RO is that it can recover water with a high flux even when the salt concentration is as high as 25% close to saturation since MD does not suffer from limitations of osmotic pressure which is a major limitation of RO.

1.1.2 MD Membranes

Microporous hydrophobic (non-wetting) membranes are used as a barrier between two liquid phases or one liquid and one gas phase in the MD process. Commercially available hydrophobic membranes are usually made from polytetrafluoroethylene (PTFE), polyvinylidene fluoride (PVDF) or polypropylene (PP). MD membranes can be used with or without supports. The membranes are generally supported on woven or matted matrix to provide mechanical strength. Most of the MD membranes are assumed isotropic, as the

pore geometry is almost uniform across the entire membrane. However, there are still some complications in membrane properties such as membrane pore size, porosity, tortuosity and thickness. Among these complications, pore size distribution is a very important factor contributing to MD performances since it determines the mass transfer mechanisms inside the membrane pores.

In general, the membrane used in the MD system should have low resistance to mass transfer and low thermal conductivity to prevent heat loss across the membrane. In addition, the membrane should have good thermal stability in extreme temperatures; high resistance to chemicals, such as acids and bases; good mechanical strength and flexibility.

1.1.3 MD Modules

1.1.3.1 Flat Sheet Membrane Cell. The membrane and the spacers are layered together between two plates (e.g. flat sheet). The flat sheet membrane configuration is widely used on laboratory scale, because it is easy to clean and replace. The flow pattern is generally cross flow. However, a membrane support is required. The channels inside the membrane cell are complex and thus make it difficult to determine the values to be used for dimensionless numbers for heat transfer analysis.

1.1.3.2 Hollow Fiber Module. The hollow fiber module is generally a hollow tubular shell sealed appropriately at both ends and contains a bundle of hollow fiber membrane. The feed solution flows through the hollow fiber bore and the permeate is collected on the outside of the membrane fiber; alternately the feed solution flows on the

outside of hollow fibers and the permeate is collected inside the hollow fiber. The main advantages of the hollow fiber module are very high packing density creating a high surface area per unit device volume and supposedly low energy consumption. On the other hand, it has high tendency to fouling and is difficult to clean once feed solution penetrates the membrane pores.

1.1.3.3 Tubular Membrane. In this type of module, the membrane is a tube and inserted between two cylindrical chambers (hot and cold fluid chambers). In the commercial field, the tubular module is more attractive, because it has low tendency to foul, easy to clean and has a high effective area. However, the packing density of this module is low and it has a high operating cost.

1.1.3.4 Spiral Wound Module. In this type of module, flat sheet membrane and spacers are enveloped and rolled around a perforated central collection tube. The feed moves across the membrane surface in an axial direction, while the permeate flows radially to the center and exits through the collection tube. The spiral wound membrane has a low but reasonable packing density, average tendency to fouling and acceptable energy consumption. But it is difficult to clean, maintain and troubleshoot.

1.1.4 Membrane Properties

1.1.4.1 Membrane Pore Size (d_M) and Pore Size Distribution. The nominal membrane pore size (d_M) and especially the maximum membrane pore size (d_{max}) are critical; it should be large enough to deliver high membrane permeability, but should be

relatively small to prevent pore wetting. Commercial MD membranes have their nominal pore size in the range of 0.1 to 0.5 μm.

1.1.4.2 Membrane Porosity (ε) and Tortuosity (χ). Membrane porosity (ε) refers to the void volume fraction of the membrane, which is the volume of the pores divided by the total volume of the membrane. Higher porosity membranes have a larger evaporation surface area. Commercial MD membrane porosity usually ranges from 60% to 80%. Membrane tortuosity is the deviation of the pore structure from the straight cylindrical shape. As a result, the higher the tortuosity value, the lower the permeate flux. The pore tortuosity (χ) can be estimated by CO_2 diffusion through water immobilized in the pores by an exchange method [8-9].

1.1.4.3 Membrane Thickness (δ_M). The membrane thickness is an important property in the MD system. Permeate water vapor flux is inversely proportional to membrane thickness since mass transfer resistance increases linearly with the membrane thickness. On the other hand, heat loss is reduced as the membrane thickness increases. Commercial MD membrane thickness usually ranges from 60 μm to 200 μm.

1.1.4.4 Characterization Methods. The characterization methods employed to find out various membrane properties include liquid entry pressure (LEP), bubble point and electron microscopy.

1.2 Previous Work

Membrane distillation as a technology has more than 50 years' history. Membrane distillation was first proposed by Bodell [10-11] in 1963 in the form of SGMD where the outer surface of a hydrophobic capillary silicone rubber tube was in contact with warm aqueous solution. Water vapor passed through the membrane into the air stream on the other side of the silicone rubber tube and was condensed in an external condenser. Findley [12] concluded MD will become an important possibility to desalination if "low cost, high temperature, long-life membranes with desirable characteristics" can be obtained. However, this was not achieved until 1980s when membrane manufacturing techniques were advanced and the industry began to show interest in MD. Gore [13] published details of Gore-tex MD systems based on expanded PTFE (ePTFE) membranes in spiral-wound modules. However, this technology was abandoned because of poor heat transfer and water vapor transport.

More and more studies have been focused on MD wetting, fouling and flux performance after 1985 in various applications: desalination, concentration of dissolved ions, macromolecules, colloids and low concentration of organics; concentration of fruit juices, milk and industrial waste water.

Water vapor transport mechanisms for MD have been extensively analyzed in the literature [1]. Different types of mechanisms have been proposed for the transport, namely, Knudsen flow model, viscous flow model, ordinary molecular diffusion model,

and the combination thereof by the dusty gas model (DGM) [14–16] and those by Schofield et al. [17-18].

Using these models, there have been a number of studies which have modeled the transport of water vapor through a membrane in MD. In such cases, the heat transfer coefficients in the fluid are generally known so that the temperatures on the two surfaces of the membrane could be easily isolated. Knowing these temperatures one can determine the membrane mass transfer coefficient and check it against any proposed model. In real-life applications, the fluid mechanics on the two sides may be complex and the convective heat transfer coefficients unknown.

Membrane surface temperature is not easily and directly measurable. It was attempted to directly measure the interfacial temperature using miniature PT100 sensors [19]. Further investigation is needed to determine the effect of sensors on the thermal boundary layer conditions. Thermochromic Liquid Crystals (TLCs) have been applied to measure the temperatures distribution inside the module channels by recording the color change; further investigations are needed to characterize mixing and heat transfer phenomena [20]. Computational Fluid Dynamics (CFD) is being applied to model the transport phenomena in DCMD with the high cost of larger computational power requirements [21]. Extensive empirical heat transfer correlations on the boundary layers have been applied by various MD investigators to determine the membrane surface temperature. However, the dimensionless involved parameters (i.e., Reynolds numbers),

especially for flat membrane-based cells, are difficult to calculate in the presence of supports and channel spacers [2, 22–25].

Previous studies have generally focused on a few membranes with most likely a limited variation in membrane pore size [26–28]. Limited yet increasing numbers of membrane distillation (MD) publications in past decade have been statistically analyzed via Scopus database and it is shown in Figure 1.2. It would be useful to demonstrate a general procedure to determine the membrane mass transfer coefficient under such conditions, and then check the utility of the existing mass transfer models.

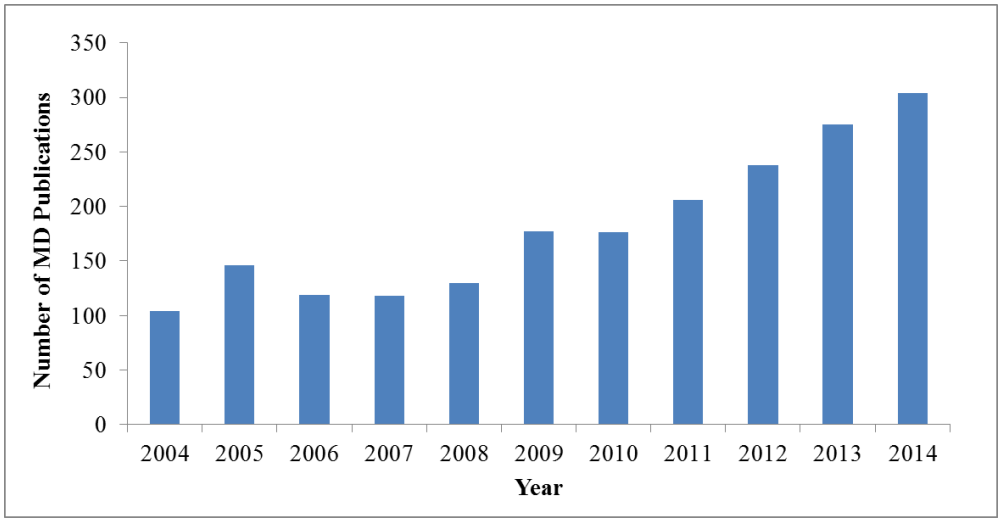

Figure 1.2 Limited yet increasing number of membrane distillation (MD) publications (journal articles, conference papers, and patents) between the years 2004 and 2014 (Data retrieved from Scopus database search).

A variety of membranes are available with considerable variations in membrane thickness, pore size, pore size distribution, porosity, pore tortuosity, material etc. It will be useful if such a variety of membranes can be characterized and the usefulness of MD

transport models verified. This is intimately connected with the loss of sensible heat in the hot brine to the distillate by heat conduction.

1.3 Objectives of this Dissertation

The goal of this dissertation is to examine the fundamental aspects of heat transfer and membrane mass transfer in DCMD and VMD. Eight different flat membranes of two different materials, PVDF and ePTFE were studied. The membrane thickness was varied between 23 μm to 125 μm; the pore size was varied from 0.05 μm to 0.45 μm. The porosity was generally high in the range of 0.7-0.8.

In DCMD, the hot brine temperature was varied between 65 ℃ to 85 ℃ with the membrane mean temperature varying between 40 ℃ to 60 ℃ since the distillate was at 20 ℃. In VMD, brine side flow temperatures and flow rates was kept the same as DCMD. Knudsen diffusion and the transition region models were employed to predict the membrane transport coefficient for water vapor. Heat transfer coefficients of the boundary layers on two sides of the membrane were empirically characterized for DCMD via the Wilson plot method. The behavior of the observed water vapor flux was simulated as a function of the flow conditions on two sides of the membrane, brine temperature and membrane properties. The effects of membrane properties (pore size, thickness, porosity and tortuosity) for all eight membranes and operating conditions on thermal efficiency and water vapor fluxes for small scale DCMD and VMD were determined.

The performance estimates for larger hollow fiber-based MD devices were analyzed for experimental conditions from a previous pilot plant study [29] using the mathematical models developed and numerically solved in MATLAB. The key issue was using membrane properties to predict membrane mass transfer coefficient k_m instead of using k_m as an empirically adjustable parameter to describe the observed pilot plant flux data.

The objective of this dissertation is to review the literature on desalination by the thermal distillation method of membrane distillation (MD) regarding water vapor flux and thermal efficiency, develop mass and heat transport models for a variety of MD membranes and techniques, experimentally investigate the utility of a variety of membrane transport models, define ideal membranes for different MD processes and develop performance estimates for larger MD devices. This is to be implemented with a focus on two MD techniques, DCMD and VMD.

1.4 Chapter Summaries

Chapters 2 and 3 develops the fundamental heat and mass transfer equations in water vaporization, boundary layer heat transfer, thermal conductions across the membrane and combined heat and mass transfer models in DCMD and VMD, respectively. Membrane and membrane cells, chemicals and characterization instruments as well as experimental procedures are also described. The influence of microporous membrane properties and operating conditions on the process performances is discussed.

Performance estimates for larger hollow fiber-based DCMD devices such as water vapor flux, brine/distillate outlet temperatures, membrane mass transfer coefficient were simulated in Chapter 4 using the models found to be useful in Chapter 2.

CHAPTER 2

DIRECT CONTACT MEMBRANE DISTILLATION (DCMD)

2.1 Theory

In DCMD - based desalination, hot brine passing over one side of a porous hydrophobic membrane creates a surface for vaporization of water, while cold distillate is passed over the other side of the membrane creating condensation of this water vapor (Figure 2.1A). Vapor liquid interface occurs at every entrance of the membrane pores as a result of the hydrophobic nature of the porous membrane. The difference in water vapor partial pressure due to temperature difference on both sides of the membrane is the driving force for water vapor transfer.

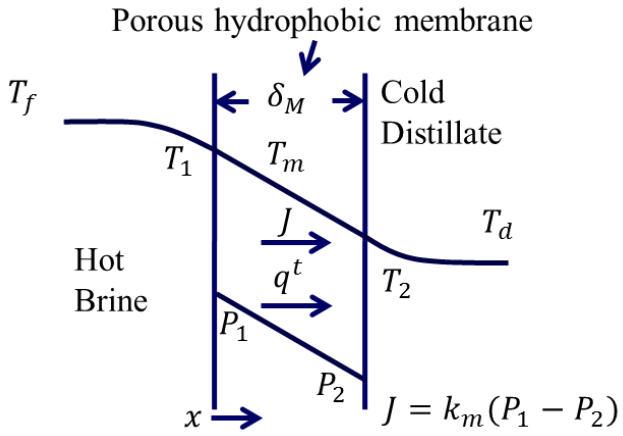

Figure 2.1A Direct contact membrane distillation (DCMD).

2.1.1 Mass Transfer

Mass transfer of water vapor through a membrane depends among others on the membrane pore size, porosity, thickness and tortuosity. In DCMD, both feed and

permeate solutions are in direct contact with the membrane under essentially atmospheric conditions. The total pressure is assumed to be maintained at ~1 atm; viscous flow is therefore negligible. Schofield et al. [30] have shown that in DCMD applications, the net flux of air across the membrane is extremely small relative to the flux of water vapor, and viscous flux can be neglected.

The mass transfer mechanisms strongly depend on the Knudsen number (K_n):

$$K_n = \frac{\lambda_{w-a}}{d_p} \tag{2.1}$$

where λ_{w-a} is the mean free path of water vapor and air and d_p is the nominal membrane pore diameter. For a binary mixture of water vapor and air, the mean free path is expressed by

$$\lambda_{w-a} = \frac{k_B T_m}{\pi P_T \left(\frac{(\sigma_w + \sigma_a)}{2}\right)^2} \frac{1}{\sqrt{1 + \frac{M_w}{M_a}}} \tag{2.2}$$

where k_B is the Boltzmann constant, P_T is the total pressure (1 atm), σ_w and σ_a are the collision diameters for water vapor (2.641×10^{-10} m) and air (3.711×10^{-10} m), respectively [31,32]; T_m is the membrane mean surface temperature, $T_m = ((T_1 + T_2)/2)$. Values of the mean free path for a binary mixture of water vapor and air at different membrane mean surface temperatures (T_m) are listed in Table 2.1 for a range of membrane pore size from 0.05 μm to 0.45 μm used in this study.

If the mean free path of the molecules is larger than membrane pore size (K_n>1, d_p<λ), molecule – pore wall collisions are dominant and Knudsen diffusion model should

be considered. If K_n<0.01, d_p>100 λ, molecular diffusion is used to describe the mass transport in the continuum region; consider stagnant air trapped within membrane pores due to the low solubility of air in water. If 0.01<K_n <1, λ <d_p<100λ, the mass transport mechanism is in transitional region which could be described by combined Knudsen diffusion model and ordinary molecular diffusion flow model. Since mean free path for binary mixture of water vapor and air at T_m from 40 ℃ - 60 ℃ is around 0.11 μm, Knudsen diffusion or combined Knudsen/molecular diffusion model is considered for membranes having pore sizes in the range of 0.05 μm - 0.45 μm.

Table 2.1 Mean Free Path for Binary Mixture of Water Vapor and Air For Different Values of T_m

P_T (Pa)	T_m (℃)	λ_{w-a} (μm)	d_p (μm)	K_n
101325	40	0.106	0.05	2.116
			0.1	1.058
			0.2	0.529
			0.45	0.235
	50	0.109	0.05	2.183
			0.1	1.092
			0.2	0.546
			0.45	0.243
	60	0.113	0.05	2.251
			0.1	1.125
			0.2	0.563
			0.45	0.250

The general mass transfer expression for water vapor flux J in DCMD can be expressed by

$$J = k_m\,(P_{w,1} - P_{w,2}) \tag{2.3}$$

where $P_{w,1}$ is water vapor partial pressure at the brine side of the membrane surface; $P_{w,2}$ is water vapor partial pressure at the distillate side of the membrane surface; T_1 is the membrane surface temperature on the brine side of the membrane; T_2 is the surface temperature on the distillate side of the membrane. The values of $P_{w,1}$ and $P_{w,2}$ are calculated from T_1 and T_2 by Antoine equation (by neglecting the very limited effect of salt on water vaporization for 1 wt% brine used here)

$$\log_{10} P(mm\,Hg) = 8.017 - \frac{1730.6}{233.426 + T(℃)} \tag{2.4}$$

The DCMD mass transfer model for Knudsen diffusion (K_n>1, d_p<λ) can be expressed for a membrane of thickness δ_M by

$$J = \frac{D_{Kn}}{RT_m} \times \frac{\left(P_{w,1} - P_{w,2}\right)}{\delta_M} \tag{2.5}$$

where D_{Kn} is the Knudsen diffusivity,

$$D_{Kn} = \frac{4}{3}\frac{\varepsilon_M d_p}{\chi_M}\sqrt{\frac{RT_m}{2\pi M_w}} \tag{2.6}$$

M_w is molecular weight of water 18.015 g/mol, R is the universal gas constant 8.314 J/mol-K. Here, we assume [33]

$$\chi_M = \frac{1}{\varepsilon_M} \tag{2.7}$$

where χ_M is the membrane tortuosity, ε_M is the membrane porosity. Since all membranes in this study have $\varepsilon_M \geq 0.70$, this is a reasonable assumption. This assumption has been checked here by experimentally measuring the membrane tortuosity.

The DCMD mass transfer model for transition region between Knudsen and molecular diffusion ($0.01< K_n <1$, $\lambda < d_p < 100\lambda$) can be expressed by [27]:

$$J = \frac{(\varepsilon_M/\chi_M)P_t D_{w-a}}{\delta_M R T_m} \times \ln\left(\frac{D_{Kn}(P_t - P_{w,2}) + \left(\frac{\varepsilon_M}{\chi_M}\right)P_t D_{w-a}}{D_{Kn}(P_t - P_{w,1}) + \left(\frac{\varepsilon_M}{\chi_M}\right)P_t D_{w-a}}\right) \quad (2.8)$$

$$P_t D_{w-a} = (1.895 \times 10^{-5}){T_m}^{2.072} \quad (2.9)$$

The diffusion coefficient for water vapor in air is given by equation (2.9) [30]. Here P_t (the total pressure in the pores) is assumed to be 101.3 kPa (1 atm).

2.1.2 Heat Transfer

In DCMD, sensible heat supplied by hot brine leads to water evaporation as well as heat conduction through the membrane structure and vapor/gas-filled membrane pores. Heat conduction is considered heat loss in DCMD because it does not lead to water evaporation; it reduces the thermal efficiency. Water evaporated from the hot brine reduces the membrane surface temperature from the bulk brine temperature; water vapor condensed into cold distillate increases the membrane surface temperature from the bulk distillate temperature. The fact that the membrane surface temperature on the hot side is lower than the bulk temperature of hot brine is identified as one source of temperature polarization; it results in decreased water vapor partial pressure difference across the membrane thus decreasing the water vapor flux.

In case of no heat loss to the ambient, the total heat transfer rate Q_t (J/min) is equal to the brine side heat transfer rate; it is also equal to the distillate side heat transfer rate:

$$Q_t = \mathrm{q}^t \times A_m \tag{2.10}$$

$$Q_b = \rho_b C_{pb} F_{bi} T_{bi} - \rho_b C_{pb} F_{bo} T_{bo} \tag{2.11}$$

$$Q_d = \rho_w C_{pw} F_{do} T_{do} - \rho_w C_{pw} F_{di} T_{di} \tag{2.12}$$

$$Q_t = Q_b = Q_d \tag{2.13}$$

Further

$$F_p = F_{do} - F_{di} = F_{bi} - F_{bo} \tag{2.14}$$

where F_p is the collected permeate flow rate (mL/min).

Here, we use the total heat flux q^t based on the distillate side heat flux to account for any heat loss to ambient from the hot brine:

$$\mathrm{q}^t = \frac{\rho_w C_{pw} F_{do} T_{do} - \rho_w C_{pw} F_{di} T_{di}}{A_m} \tag{2.15}$$

$$\mathrm{q}^t = h_0\left(T_f - T_d\right) \tag{2.16}$$

$$q_d = h_d(T_2 - T_d) \tag{2.17}$$

$$q_f = h_f(T_f - T_1) \tag{2.18}$$

$$q_m = h_m(T_1 - T_2) \tag{2.19}$$

$$\mathrm{q}^t = q_d = q_f = q_m \tag{2.20}$$

We further assume: the hot brine side average temperature (K) is

$$T_f = (T_{bi} + T_{bo})/2 \tag{2.21}$$

T_d is the distillate side average temperature (K); $T_d = (T_{di} + T_{do})/2$ (2.22)

In addition, h_0 is the overall heat transfer coefficient, h_d is the distillate side heat transfer coefficient, h_f is the brine side heat transfer coefficient and h_m is the membrane heat transfer coefficient.

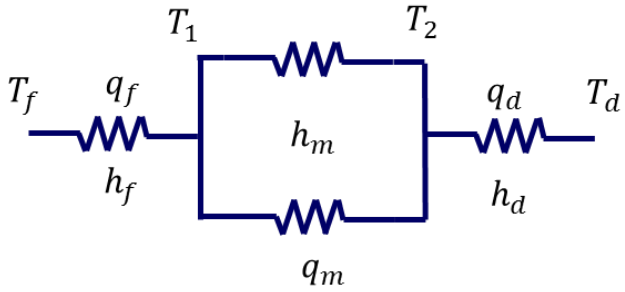

Figure 2.1B Heat transfer resistances in DCMD.

The total heat transfer resistance has three contributions: brine side heat transfer resistance, membrane heat transfer resistance, and distillate side heat transfer resistance (Figure 2.1B):

$$\frac{1}{h_0} = \frac{1}{h_f} + \frac{1}{h_m} + \frac{1}{h_d} \tag{2.23}$$

High brine side heat transfer coefficient reduces temperature polarization leading to a higher water vapor transport rate; similarly, on the distillate side to a lesser extent.

Heat transfer across the membrane occurs via latent heat and sensible heat transfer associated with water vapor flux; the heat transfer across the membrane is given by:

$$q_m = JH_v(T) - k_{mt}\frac{dT}{dx} \tag{2.24}$$

where $H_v(T)$ is the enthalpy of water vapor which includes the latent heat of vaporization for water and sensible heat above 0 ℃, k_{mt} is the thermal conductivity of the membrane, which is commonly expressed by the Isostrain (parallel) model or by the Isostress (series) model [34]

Isostrain (parallel) model: $$k_{mt} = (1 - \varepsilon_M)k_s + \varepsilon_M k_v \quad (2.25)$$

Isostress (series) model: $$k_{mt} = \left[\frac{1-\varepsilon_M}{k_s} + \frac{\varepsilon_M}{k_v}\right]^{-1} \quad (2.26)$$

Here k_s is the thermal conductivity of the polymer. It is 0.17-0.19 W/m-K for PVDF material and 0.25-0.27W/m-K for PTFE material [35]. The value of the thermal conductivity of the air, k_v, is 0.0271 W/m-K at 313K and 0.0285 W/m-K at 333K; for saturated water vapor, k_v is 0.001948 W/m-K at 313K and 0.002110 W/m-K at 333K [36]. Equation (2.25) has been employed here.

In this dissertation, Wilson plot method (Figures 2.2A&2.2B) is employed to determine the boundary layer heat transfer coefficients (h_f, h_d) and the membrane surface temperatures (T_1, T_2). Wilson plot method [37] was developed to evaluate the convective heat transfer coefficients in shell and tube condensers. Wilson method avoids the direct measurement of the surface temperature and consequently the disturbance to the fluid flow. The overall thermal resistance in DCMD has been expressed by Equation (2.23).

The thermal resistance due to any fluid fouling has been neglected in Equation (2.23). The membrane thermal resistance ($1/h_m$) is considered constant for a given membrane. For brine side Wilson plot (Figure 2.2A), by varying only the brine side flow

rate, the change in the overall thermal resistance $(1/h_0)$ would be due to the variation of brine side resistance $(1/h_f)$ since the remaining thermal resistances $(1/h_d, 1/h_m)$ in Equation (2.23) remain constant. For fully developed flow, the heat transfer coefficient may be assumed to be proportional to a power of the velocity which could be expressed by [37]

$$h_f = a{v_f}^n \tag{2.27}$$

where a is a constant, v_f is the brine side velocity and n is the corresponding velocity exponent.

Combining Equation (2.23) and Equation (2.27), the overall thermal resistance becomes a linear function of ${v_f}^{-n}$,

$$\frac{1}{h_0} = \frac{1}{a}{v_f}^{-n} + \frac{1}{h_m} + \frac{1}{h_d} \tag{2.28}$$

The data obtained are fitted first with a suitable n. Then a plot of $(1/h_0)$ against ${v_f}^{-n}$ will yield $(1/h_m) + (1/h_d)$ as an intercept which allows determination of $(1/h_f)$ at

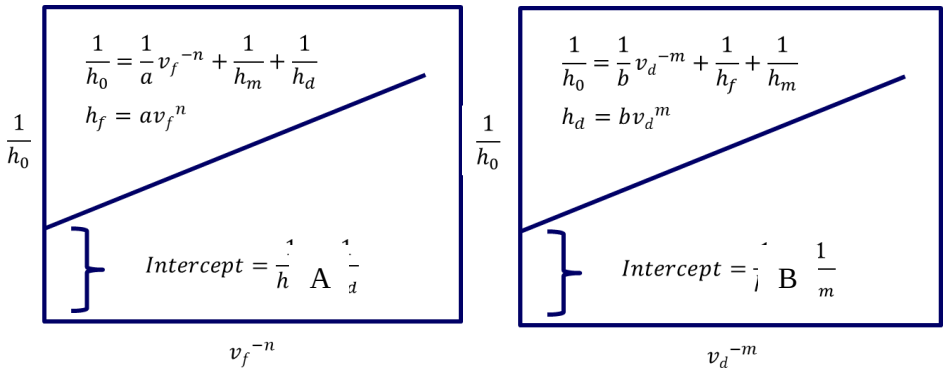

Figure 2.2A Brine side Wilson plot. **B** Distillate side Wilson plot. v_f ~ Brine velocity, ${v_f}^{-n} \Rightarrow {Q_f}^{-n}$; v_d ~ Distillate velocity, ${v_d}^{-m} \Rightarrow {Q_d}^{-m}$.

various values of v_f. For distillate side Wilson plot (Figure 2.2B), the overall thermal resistance is similarly a linear function of ${v_d}^{-m}$,

$$\frac{1}{h_0} = \frac{1}{b}{v_d}^{-m} + \frac{1}{h_f} + \frac{1}{h_m} \tag{2.29}$$

where v_d is the distillate side velocity and m is the corresponding velocity exponent. The procedure followed here is similar to that for the brine side. After the determination of a suitable m fitted to data, one obtains from the intercept $(1/h_f) + (1/h_m)$ which allows one to determine $1/h_d$ at various value of v_d. Therefore h_m can be determined easily.

2.2 Experimental

2.2.1 Materials and Chemicals

2.2.1.1 Membranes. Various porous hydrophobic PVDF and expanded-PTFE (ePTFE) flat sheet membranes employed in DCMD are listed in Table 2.2. The PVDF membranes are available as 47 mm circular flat sheet membranes. The ePTFE membranes were available as a large sheet and were cut out using a circular punch (47 mm, Brettuns Village, Inc., Lewiston, ME) and a brass hammer (Part No. 5978A12, McMaster-Carr, Robbinsville, NJ).

2.2.1.2 Membrane Cells. Two cells were used: a cylindrical stainless steel cell (Figure 2.3) and a rectangular CPVC (chlorinated polyvinyl chloride) plastic cell (Figure 2.4).

Table 2.2 Hydrophobic Membranes Used

Membrane	$\mathbf{d_M}$ (μm)	$\boldsymbol{\varepsilon_M}$ (%)	$\boldsymbol{\delta_M}$ (μm)	$\mathbf{k_{mt}}$ (W/m-K)
PVDF* (VVHP04700)	0.1	70	125	0.0673
PVDF* (GVHP04700)	0.22	75	125	0.0600
PVDF* (HVHP04700)	0.45	75	125	0.0600
ePTFE** (M-005)	0.05	80	23	0.0686
ePTFE** (M-010)	0.1	80	85	0.0686
ePTFE** (M-020A)	0.2	80	70	0.0686
ePTFE** (M-020B)	0.2	80	30	0.0686
ePTFE** (M-045)	0.45	80	98	0.0686

* EMD Millipore, Billerica, MA

** W. L. Gore & Associates, Inc., Elkton, DE

The stainless steel cell had an effective membrane area of 9 cm^2. Figure 2.3A shows the photographs of the cell. Figure 2.3B shows the upper part of the cell and Figure 2.3C shows the bottom part of the cell. The original upper part of the cell was modified to enlarge the entrance of feed brine to reduce the brine side pressure drop and to solve the membrane deformation problem as small bumps developed in the brine side for thin ePTFE membranes.

A rectangular CPVC cell was designed and modeled in AutoCAD 2009 by Autodesk (San Rafael, CA) to reduce the brine side heat loss and to solve the membrane deformation problem. The cell had an effective membrane area of 11 cm^2. The CPVC cell

consists of two identical parts. Figure 2.5 shows a 3D AutoCAD drawing for bottom part of the cell. Top view and side view of the cell design are shown in Figure 2.6 and Figure 2.7, respectively. A cell configuration of CPVC overview is shown in Figure 2.8. There is a mesh space having a depth of 0.015'' in the middle of this part; accordingly, the membrane spacer thickness ranged from 0.012 to 0.018''. Channels are on the edges of the mesh space to prevent dead corner. The space between two channels is blocked (no flow). Feed brine inlet and outlet were located in both short sides of the cell. After the feed brine came into the cell, it came out from the channel towards the inlet and was exposed to membrane. Then, feed brine went back to the channel towards outlet and came out from the outlet. There is a specific square shape with round corners design for o-ring groove right outside the mesh space. There are four stainless pins on the edges of the cell in order to secure two parts of the cell.

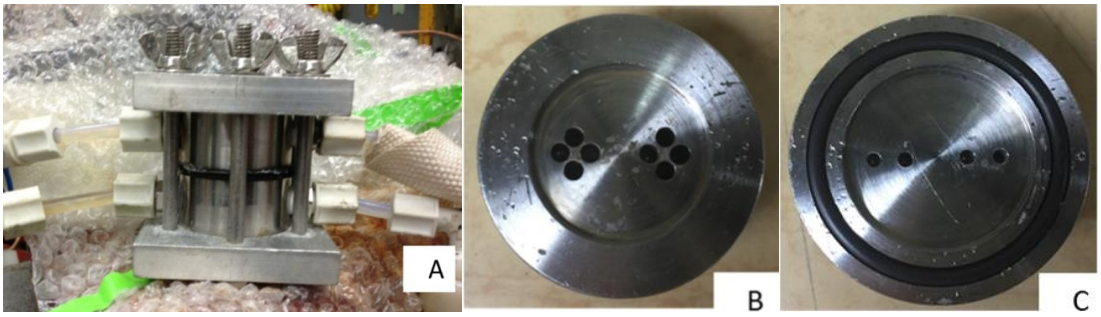

Figure 2.3 Photographs of (A) stainless steel cell, (B) brine side of the cell, (C) distillate side of the cell. Membrane area: 9 cm^2.

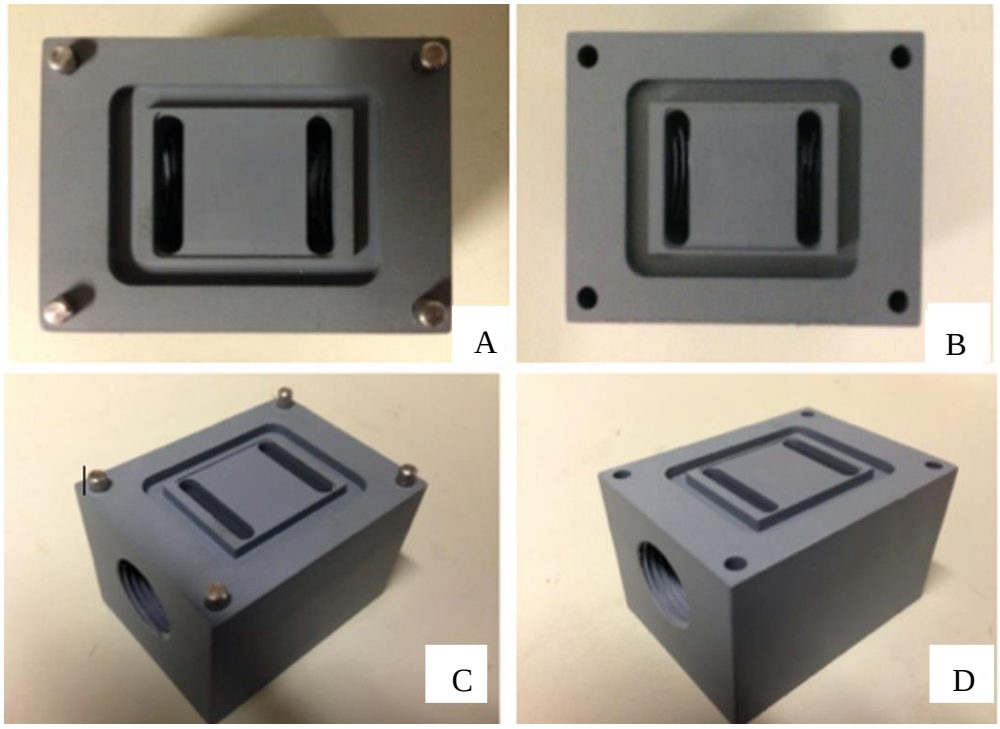

Figure 2.4 (A) & (C) Photos of the brine side of the plastic cell; (B) & (D) Photos of the distillate side of the plastic cell. Membrane area: 11 cm^2.

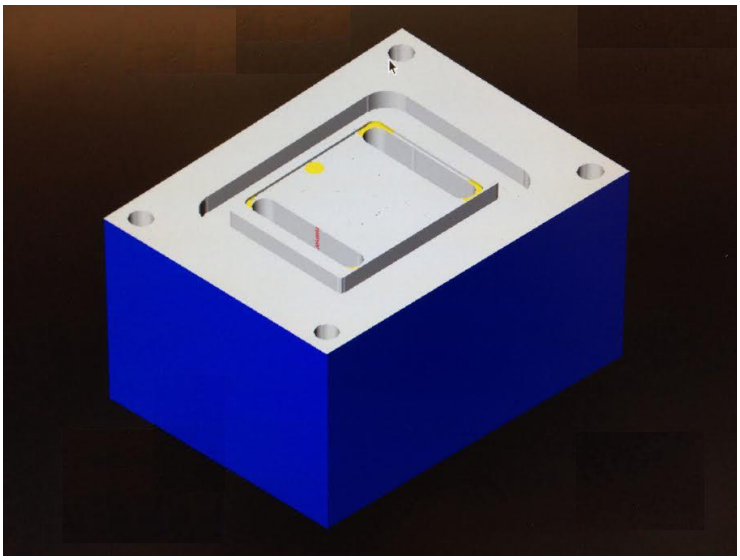

Figure 2.5 3D AutoCAD drawing for bottom part of the CPVC cell.

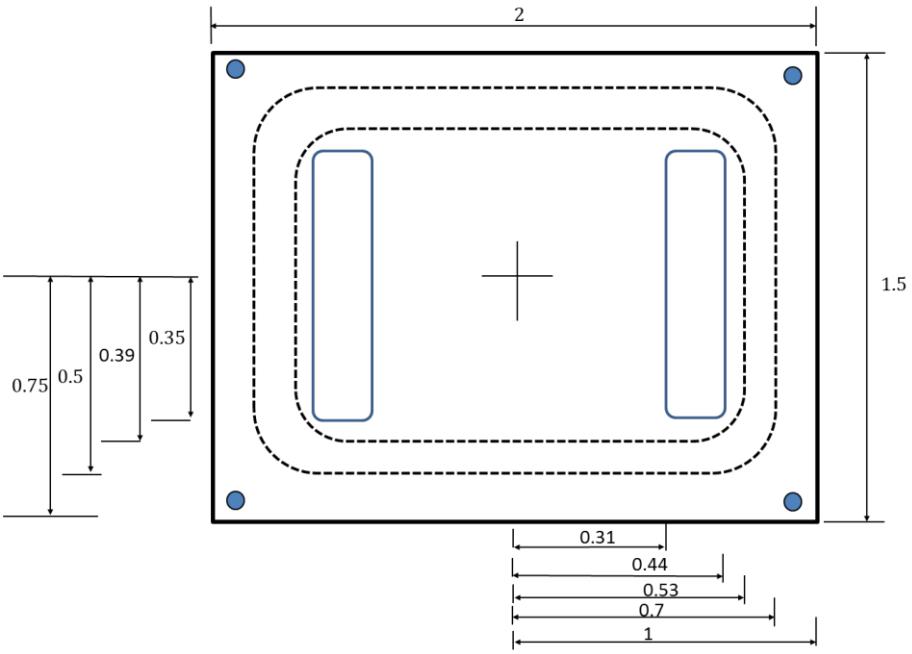

Figure 2.6 Cell top view: 2 in × 1.5 in; Cell dimension: 2 in × 1.5 in × 1 in; Membrane area: 1.4 in × 1 in; Membrane support area: 1.06 in × 0.78 in × 0.015 in; Cell alignment rod diameter: 0.125 in, length 0.25 in; Channel: 0.125 in × 0.7 in.

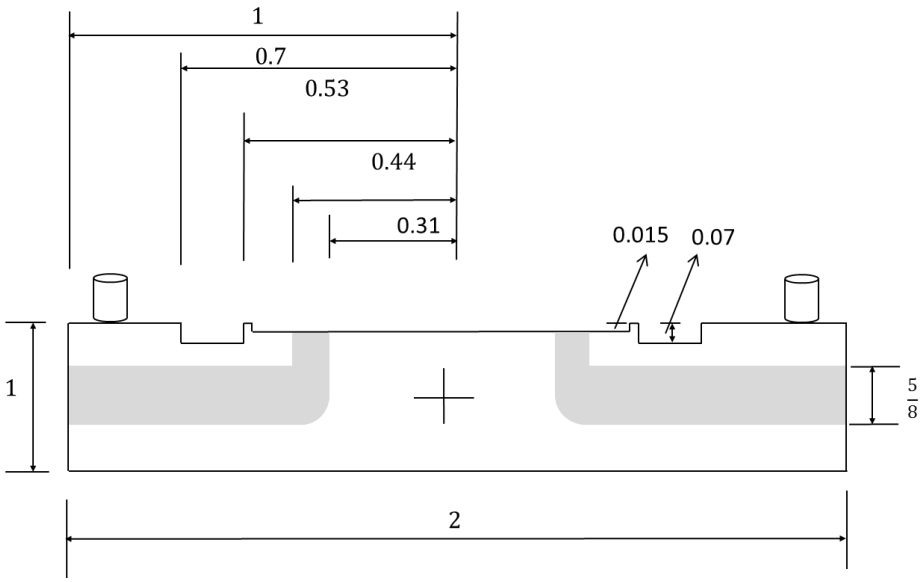

Figure 2.7 Cell side view: 2 in × 1.5 in; Cell dimension: 2 in × 1.5 in × 1 in; Membrane support area: 1.06 in × 0.78 in × 0.015 in; O-ring actual width: 0.07 in.

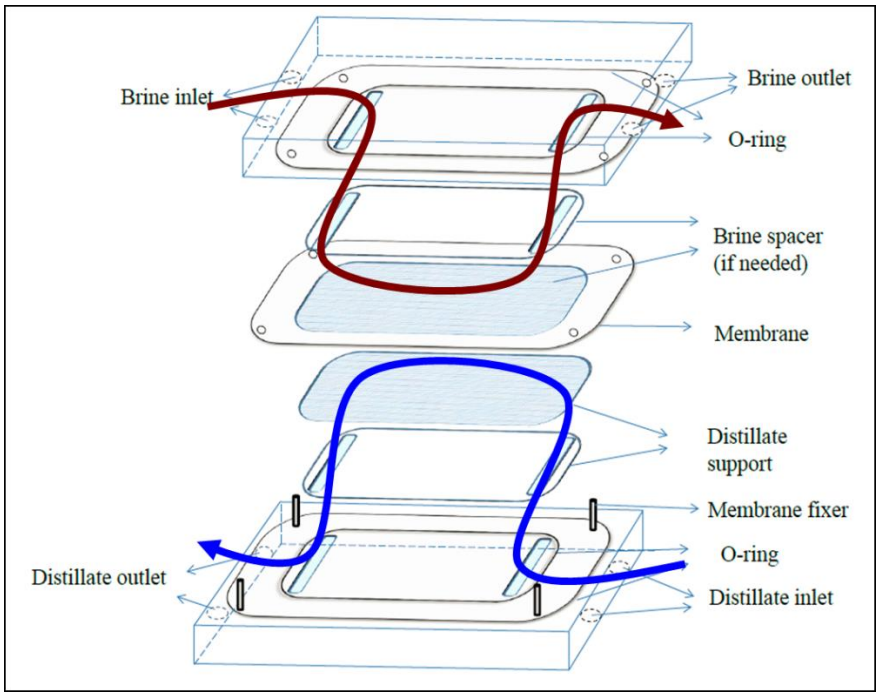

Figure 2.8 Plastic cell configuration made of CPVC (Chlorinated polyvinyl chloride).

In the work leading to this dissertation, extensive experiments were conducted using the CPVC cell since heat loss was drastically reduced.

2.2.1.3 Membrane Supports. The membrane supports are used to provide mechanical strength for membranes.

For the circular stainless steel cell, two stainless steel supports, diameter 47 mm and 34 mm, thickness 600 μm (Pall Corp., Port Washington, NY) were tried at first. However, due to its very low thickness, it did not fit properly in the cell and reproducible results were obtained only when a few of the stainless steel supports are put together. PTFE mesh (Part No. ET8800, Industrial Netting, Minneapolis, MN) was used to support the membrane from the distillate side of the stainless steel cell and to even the gap

between membrane and the edge of the cell. This mesh was chosen because the gap was considerable. The mesh has a thickness from 0.066 to 0.086 inch with a nominal opening size 0.144 x 0.370 $inch^2$. The diameter of the mesh was cut out around 34 mm and 47mm. The 34mm diameter mesh had less sealing problem. This opening size of this PTFE mesh is on the large side of commercial membrane supports. Due to manufacturing limitation, a thick PTFE mesh will come with large opening size. Too large an opening size will not provide proper mechanical strength to membrane, unless stacking another fine mesh on top of it which will create unwanted resistance. Therefore, another cell is needed to alter the gap between membrane and cell, and it will be easier to find membrane supports that can work properly. Different support arrangements were studied per Figures 2.9A, 2.9B, 2.9C and 2.9D. Configuration of Figure 2.9A was selected where the membrane is supported on the distillate side by a PTFE mesh which fills out the cell depression effectively.

For the CPVC cell, a PTFE mesh (Part No. 1100T41, McMaster-Carr, Robbinsville, NJ) was used to support the membrane from the distillate side. Brine side support was also tested but was not used because of the extra resistance in the brine side and therefore lower water vapor flux. The gap between the membrane and the edge of the cell was deliberately designed to fit the PTFE mesh thickness. This mesh has a thickness of 0.015 inch with an opening size 0.025 x 0.005 $inch^2$. The diameter of the mesh was cut out to support the membrane. It was attempted to make it with the same effective membrane area as the stainless steel cell which is 9 cm^2. But due to manufacturing

limitation for channels and o-ring grooves, the effective membrane area in the CPVC cell had to be fabricated a little larger which is 11 cm^2.

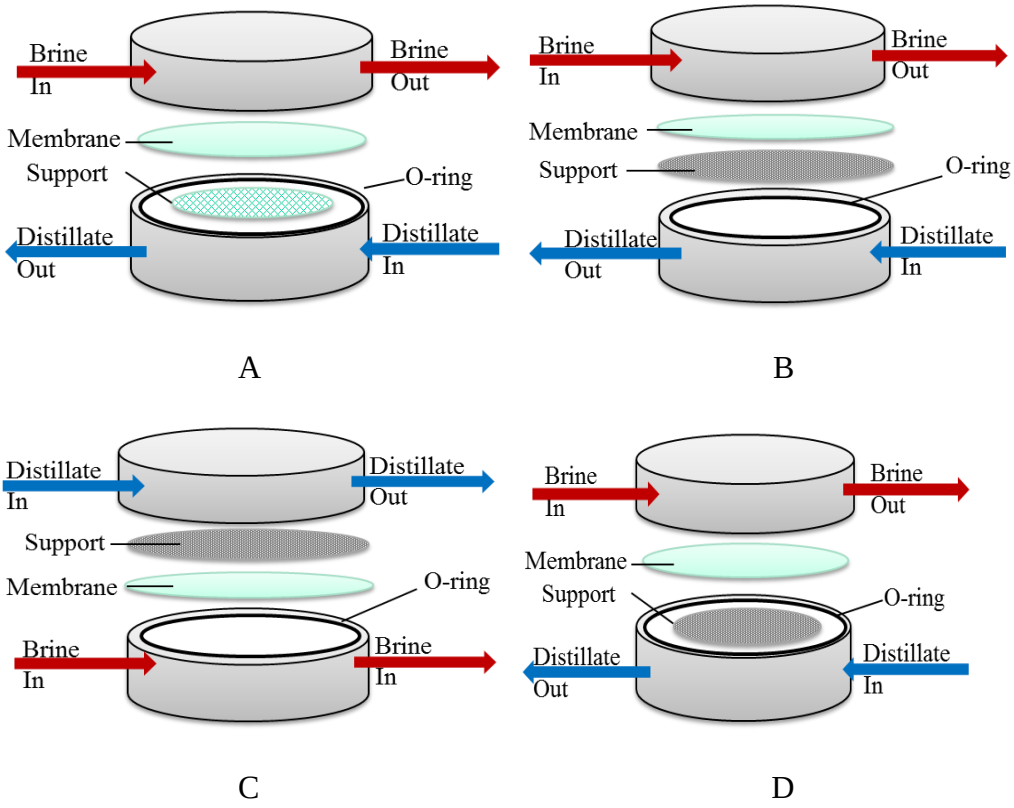

Figure 2.9 Stainless steel cell configurations A. PTFE support; B&C. Stainless steel support, diameter 47 mm; D. Stainless steel support, diameter 34 mm.

2.2.2 Apparatus for DCMD Experiments and Experimental Procedure

The DCMD experiments were performed with various hydrophobic PVDF and ePTFE flat sheet membranes over a hot brine temperature range of 65 ℃ to 85 ℃ and various flow rates ranging between 100 and 800 mL/min. A schematic of the DCMD setup is shown in Figure 2.10A. The NaCl solution (1% wt.) was introduced as the brine feed in a titanium vessel (Vargo, Lewisburg, PA) immersed in an oil bath (Haake A81, Thermo Fisher Scientific, Waltham, MA). It was pumped to one side of the membrane in the

DCMD cell through a plastic dome to eliminate the pulsation effect from a peristaltic pump. The other side of the membrane was exposed to deionized (DI) water cooled by a chiller (Polystat, Cole Parmer, Vernon Hills, IL) as the distillate stream condensing the water vapor. After the DCMD cell, hot brine was recycled to the brine tank; distilled water was recirculated to the distillate tank. The brine tank was fitted with a liquid level controller (Warrick Series 16, Gems Sensors & Controls, Plainville, CT) to maintain constant brine concentration due to continuous vaporization of water from the hot brine feed solution into membrane pores. This liquid level controller activated a pump to take in fresh DI water from a makeup water storage tank. A degassing module (Figure 2.10B) was connected to distillate side of the CPVC cell for particular experiments. A vacuum pump was attached to the degassing module on the other side to determine the effect of air flux in DCMD.

Inlet and outlet temperatures of the brine and the distilled water streams through the test cell were monitored by platinum RTD sensors (Model RTD-NPT-72-E-1/4-HH804-CONN, Omega, Stamford, CT; Accuracy:0.15+0.002T(°C)) connected to digital thermometers (Dual Input Pt100 Platinum RTD meter, Model HH 804, Omega, Stamford, CT; Accuracy: ±0.05%+0.2°C). The flow rates of brine out and distillate out streams were measured manually before membrane distillation flux measurements were initiated. The water vapor flux was measured by measuring the overflowing distillate mass per hour using a weighing machine. The conductivity on the distillate side was measured using a conductivity meter (Orion 115A+, Thermo Fisher Scientific, Waltham, MA). Any

experiment under given conditions was run for around 3 hour after steady state was reached. Each experiment was repeated three times to check reproducibility. After experiments were finished, the system was washed with DI water at room temperature to eliminate any salt residue, its rusting effect potentially on the system and fittings and the wetting effect potentially on the membrane.

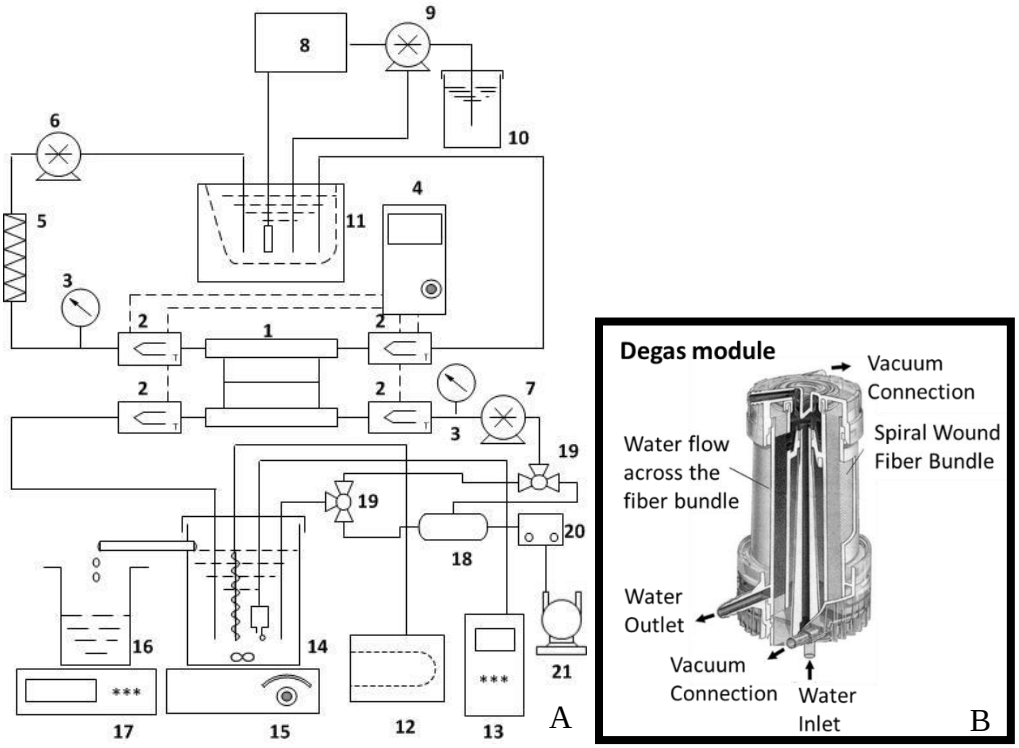

Figure 2.10A Schematic of DCMD setup. 1. Membrane test cell; 2. Thermocouple; 3. Pressure indicator; 4. Digital thermometer; 5. Pre-filter; 6. Brine pump; 7. Distillate pump; 8. Liquid level controller; 9. Make-up pump; 10. Make-up water reservoir; 11. Brine water-bath; 12. Chiller; 13. Conductivity meter; 14. Distillate beaker; 15. Magnetic stirrer; 16. Distillate overflow beaker; 17.Weighing balance; 18. Degas module; 19. Three-way valve; 20. Vacuum regulator; 21.Vacuum pump.
B Degas module configuration.

2.2.2.3 Determination of Maximum Pore Size. The maximum membrane pore size was determined from bubble point test (Figure 2.11). The test membrane was wetted completely by floating it on a pool of isopropyl alcohol (IPA). Then the wetted membrane was placed in the bubble point test cell; IPA was used to fill the perforated metal plate in the upper chamber of cell. Air was slowly applied on the lower part of the filter. Initially (no pressure), all the membrane pores were filled with IPA. At very low pressure, the pores remained filled with IPA. By increasing the applied pressure, the largest pores were emptied of this liquid, and the gas flux started to increase (Figure 2.12).

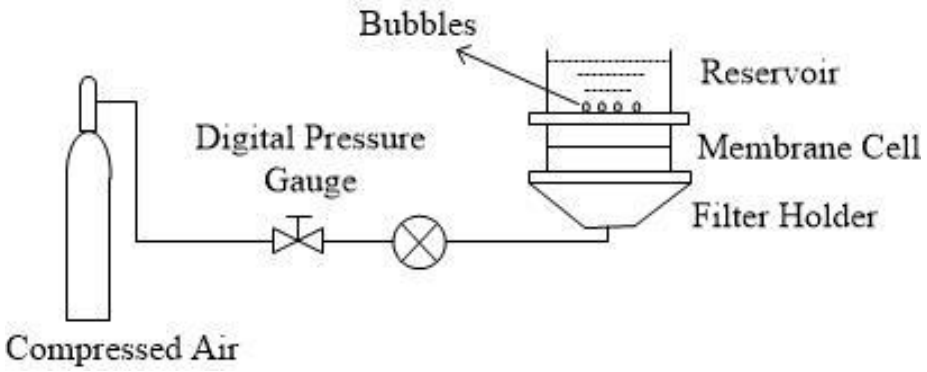

Figure 2.11 Bubble point measurement setup.

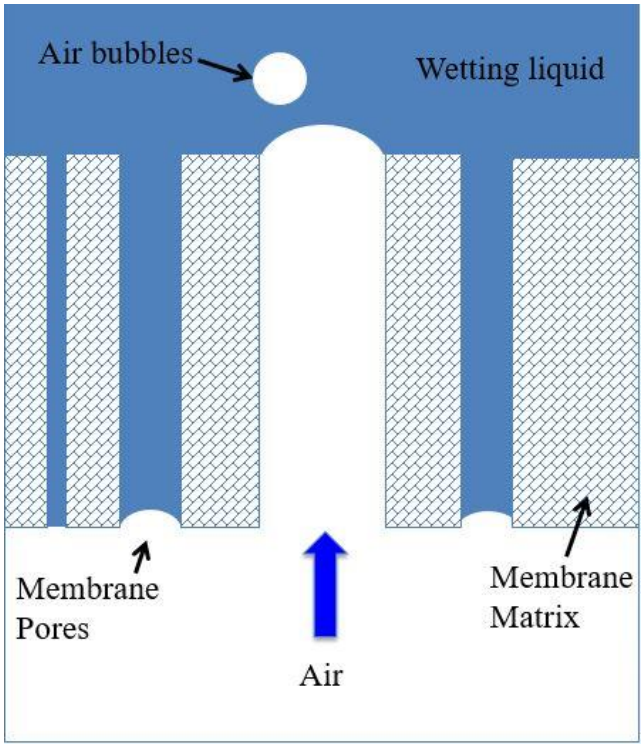

Figure 2.12 Bubble point pressure concept.

The minimum pressure was recorded when a steady stream of bubbles rised from the central area of the upper chamber. Wetting liquid was held in the membrane pores by capillary attraction and surface tension during the bubble point test. The minimum pressure required to force liquid from these pores was a function among others of the pore diameter. The maximum pore size was determined by:

$$P_{BP} = \frac{4\,\gamma\,cos\theta}{d_{max}} \tag{2.30}$$

$$d_{max} = \frac{4\,\gamma\,cos\theta}{P_{BP}} \tag{2.31}$$

where P_{BP} is the bubble point pressure; γ is the surface tension of IPA (0.0217 N/m at 20 ℃); θ is the contact angle between IPA and the membrane surface. Here, θ was assumed 0° since the membrane was fully wetted; d_{max} is the maximum membrane pore diameter.

2.2.2.4 Gas Permeation Study for Tortuosity Measurement Gas permeation study was performed to determine the membrane tortuosity (Figure 2.13). The membrane was completely wetted by water by an exchange method [8,9].

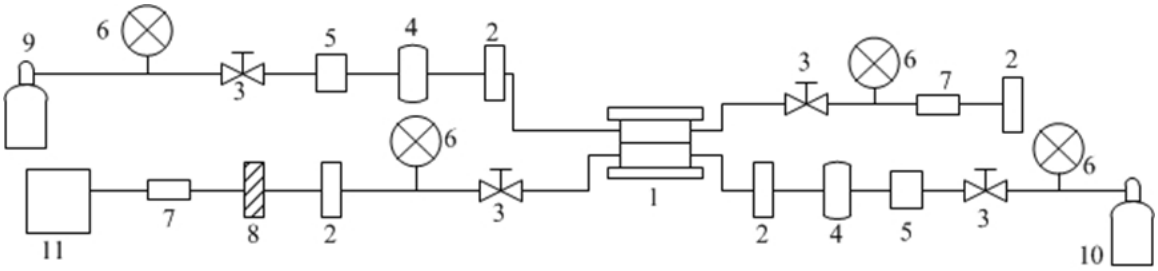

Figure 2.13 Tortuosity measurement setup.

The exchange method developed here consists of the following steps: Membrane was kept immersed consecutively in (a) 100% ethanol, (b) 80% ethanol/ 20%water, (c) 50% ethanol/ 50% water, (d) 30% ethanol/ 70% water, (e) 10% ethanol/ 90% water (a~e each step for 6 hours); (f) After steps a~e, the membrane was kept immersed in pure water for three days. The feed gas stream (CO_2) and the sweep gas stream (He) were both saturated with water vapor by passing each gas stream separately through a stainless steel cylinder containing distilled water. Gas flow rates were controlled by a digital control box (Model No. 8274, Matheson, Montgomeryville, PA). The temperature and humidity

of each gas stream were monitored at locations before the test cell entry by temperature and humidity probe (Model HMP 76, Vaisala, Woburn, MA). The sweep gas stream line was connected to a gas chromatograph (GC) (Hewlett-Packard 5890 series II, Agilent Technology, Santa Clara, CA) for analyzing the composition of the permeating species in the sweep gas sample. The membrane tortuosity χ_M can be estimated from:

$$\chi_M = \frac{Q_{CO_2} \varepsilon_M \, \Delta P_{CO_2} \, A}{R_{CO_2} \delta_M} \tag{2.32}$$

Here Q_{CO_2} is the permeability of the CO_2 through water immobilized in the pores acting as the membrane, which is equal to the product of the diffusivity of CO_2 through water, D_{CO_2}, and the solubility of CO_2 in pure water, S_{CO_2}

$$Q_{CO_2} = D_{CO_2} S_{CO_2} \tag{2.33}$$

2.3 Simulation Models

2.3.1 Prediction of Water Vapor Flux and Membrane Mass Transfer Coefficient

In Knudsen diffusion (K_n > 1, d_p < λ), water vapor flux can be predicted from Equation (2.25), and the mass transfer coefficient can be determined from Equation (2.23). In the transition region between Knudsen and molecular diffusion (0.01< K_n <1, λ < d_p < 100λ), water vapor flux can be predicted from Equation (2.28), and the mass transfer coefficient can be determined from Equation (2.23).

Water vapor flux prediction equations for degassed DCMD experiments can be obtained from [27] as

$$J_{Predicted} = \frac{(\varepsilon_M/\chi_M)P_T D_{w-a}}{(1-\alpha)\delta_M R T_m} \times \ln\left(\frac{D_{Kn}(P_T - P_{w,2}) + \left(\frac{\varepsilon_M}{\chi_M}\right)P_T D_{w-a}}{D_{Kn}(P_T - P_{w,1}) + \left(\frac{\varepsilon_M}{\chi_M}\right)P_T D_{w-a}}\right) \quad (2.34)$$

where by Graham's law: $$-\alpha = \frac{J_{air}}{J_{water}} = -\sqrt{\frac{M_{water}}{M_{air}}} \quad (2.35)$$

Here α indicates the effect of air flux. When water vapor diffuses through a stagnant gas film (negligible air flux), $\alpha = 0$.

The membrane mass transfer coefficient obtained experimentally is given by

$$k_{m-experimental} = \frac{J_{m-experimental}}{(P_{w,1} - P_{w,2})} \quad (2.36)$$

where $P_{w,1}$ and $P_{w,2}$ are calculated from T_1 and T_2 by Antoine equation (Equation 2.4). Further

$$T_1 = T_f - \frac{q_f}{h_f} = T_f - \frac{\mathrm{q}^t}{h_f} = T_f - \frac{\rho C_p F_{do} T_{do} - \rho C_p F_{di} T_{di}}{A_m h_f} \quad (2.37)$$

$$T_2 = T_d - \frac{\mathrm{q}^t}{h_d} = T_d - \frac{\rho C_p F_{do} T_{do} - \rho C_p F_{di} T_{di}}{A_m h_d} \quad (2.38)$$

In this study, all prediction models used the nominal pore size reported by the manufacturer. The membrane tortuosity was calculated from $\chi_M = 1/\varepsilon_M$ (Equation 2.7).

2.3.2 Prediction of Water Vapor Flux Performance vs. Membrane Thickness

From Equation (2.24), one can get

$$q_m dx = \big(JH_v(T)\big)dx - k_{mt}dT \quad (2.39)$$

$$k_{mt}dT = \big(JH_v(T)\big)dx - q_m dx \quad (2.40)$$

$$\int_{T_1}^{T_2} k_{mt}\, dT = \int_0^{\delta_M} \big(JH_v(T)\big)\, dx - \int_0^{\delta_M} q_m\, dx \quad (2.41)$$

$$k_{mt}(T_2 - T_1) = J\int_0^{\delta_M} H_v(T)\,dx - q_m\delta_M \tag{2.42}$$

Define

$$H_v(T) = \lambda_H + C_v(T - T_0) \tag{2.43}$$

Equation (2.42) becomes

$$k_{mt}(T_2 - T_1) = J\int_0^{\delta_M} \left(\lambda_H + C_v(T - T_0)\right) dx - q_m\delta_M \tag{2.44}$$

$$k_{mt}(T_2 - T_1) = J\lambda_H\delta_M + JC_v\int_0^{\delta_M} T\,dx - JC_vT_0\delta_M - q_m\delta_M \tag{2.45}$$

Here, temperature is assumed to be a liner function of membrane thickness

$$T = T_1 - (T_1 - T_2)\frac{x}{\delta_M} \tag{2.46}$$

Therefore

$$\int_0^{\delta_M} T\,dx = \int_0^{\delta_M} \left(T_1 - (T_1 - T_2)\frac{x}{\delta_M}\right) dx = \frac{(T_1 + T_2)}{2}\delta_M \tag{2.47}$$

Equation (2.45) becomes

$$k_{mt}(T_2 - T_1) = J\lambda_H\delta_M + JC_v\frac{(T_1 + T_2)}{2}\delta_M - JC_vT_0\delta_M - q_m\delta_M \tag{2.48}$$

$$\frac{k_{mt}(T_1 - T_2)}{\delta_M} = q_m - J\lambda_H - JC_v(T_m - T_0) \tag{2.49}$$

where $T_m = (T_1 + T_2)/2$.

Assume: there is no heat loss to ambient; combine Equations (2.17) to (2.20) with (2.49).

Equation (2.49) becomes

$$\frac{k_{mt}(T_1 - T_2)}{\delta_M} = h_f\left(T_f - T_1\right) - J(\lambda_H + C_v(T_m - T_0)) \tag{2.50}$$

Assume $T_d = T_{di}, T_f = T_{bi}$

$$J = \frac{h_f(T_{bi} - T_1) \; - \; \frac{k_{mt}(T_1 - T_2)}{\delta_M}}{\lambda_H \; + \; C_v(T_m - T_0)} \tag{2.51}$$

Combine Equation (2.8) with Equation (2.51)

$$\frac{(\varepsilon_M/\chi_M)P_T D_{w-a}}{\delta_M R T_m} \times \ln\left(\frac{D_{Kn}(P_T - P_{w,2}) + \left(\frac{\varepsilon_M}{\chi_M}\right)P_T D_{w-a}}{D_{Kn}(P_T - P_{w,1}) + \left(\frac{\varepsilon_M}{\chi_M}\right)P_T D_{w-a}}\right) = \frac{h_f(T_{bi} - T_1) - \frac{k_{mt}(T_1 - T_2)}{\delta_M}}{\lambda_H + C_v(T_m - T_0)} \tag{2.52}$$

For a certain δ_M, there is a certain T_1, other items such as heat transfer coefficients remaining constant,

$$\delta_M = \frac{\left(\frac{(\varepsilon_M/\chi_M)P_T D_{w-a}}{RT_m} \times \ln\left(\frac{D_{Kn}(P_T - P_{w,2}) + \left(\frac{\varepsilon_M}{\chi_M}\right)P_T D_{w-a}}{D_{Kn}(P_T - P_{w,1}) + \left(\frac{\varepsilon_M}{\chi_M}\right)P_T D_{w-a}}\right)\right) \times \left(\lambda_H + C_v(T_m - T_0)\right) + k_{mt}(T_1 - T_2)}{h_f(T_{bi} - T_1)} \tag{2.53}$$

Using T_1 obtained from Equation (2.53), T_2 could be obtained from Equations (2.17) to (2.20). Knowing T_1 and T_2, a plot of J vs. δ_M can be obtained from Equations (2.51) and (2.53).

2.3.3 Thermal Efficiency

Thermal efficiency is defined as the ratio of heat transfer rate for water evaporation over total heat transfer rate:

$$\eta(\%) = \frac{Mass\ rate\ of\ water\ collection\left(\frac{g}{h}\right) \times\ latent\ heat\ of\ water\ \lambda\left(\frac{kJ}{kg}\right) \times \frac{1}{60}\left(\frac{h}{min}\right)}{Q_t\left(\frac{J}{min}\right)} \times 100 \tag{2.54}$$

2.4 Results and Discussion

2.4.1 Effect of Cell Modification on Flux in the Stainless Steel Cell

The small s. steel cell was modified because of deformation problems of thin ePTFE membranes (23 ~ 85 μm) developing small bumps near the feed brine inlet at higher flow rates. Two feed brine inlets were modified to four larger inlets to reduce pressure drop which caused membrane deformation. Experiments which were conducted before cell modification were repeated. Experimental water vapor flux results for various brine flow rates at brine inlet temperature 65℃ / distillate inlet temperature 20℃ for PVDF HVHP04700 (d_M 0.45 μm, δ_M 125 μm, ε_M 75%) membrane in the original cell and modified cell are shown in Figure 2.14. Water vapor flux values were enhanced due to cell modification.

2.4.2 Effect of Cell Configuration and Support in Stainless Steel Cell

Due to very low thickness of the stainless steel support, the 30 mm diameter stainless steel support did not fit properly in the cell; it was not possible to obtain reproducible result unless a few of them were put together. The 34 mm diameter PTFE support having 2.18 mm thickness was able to fit into the cell; the membrane used in this experiment was PVDF HVHP04700 (d_M 0.45 μm, δ_M 125 μm, ε_M 0.75). Experimental results show that water vapor flux increased from 7.8 kg/m^2-h to 21.4 kg/m^2-h as the inlet flow rate was increased from 132 mL/min to 600 mL/min (Figure 2.15). Experiments with 47 mm stainless steel support showed comparable results; flux was able to reach 10.8 kg/m^2-h

with a flow rate of 288 mL/min; while using 30 mm PTFE support, flux could reach 10.4 kg/m^2-h. In the reversed mode (Figure 2.9C), experimental result shows a lower flux of 7.2 kg/m^2-h at a flow rate of 288 mL/min.

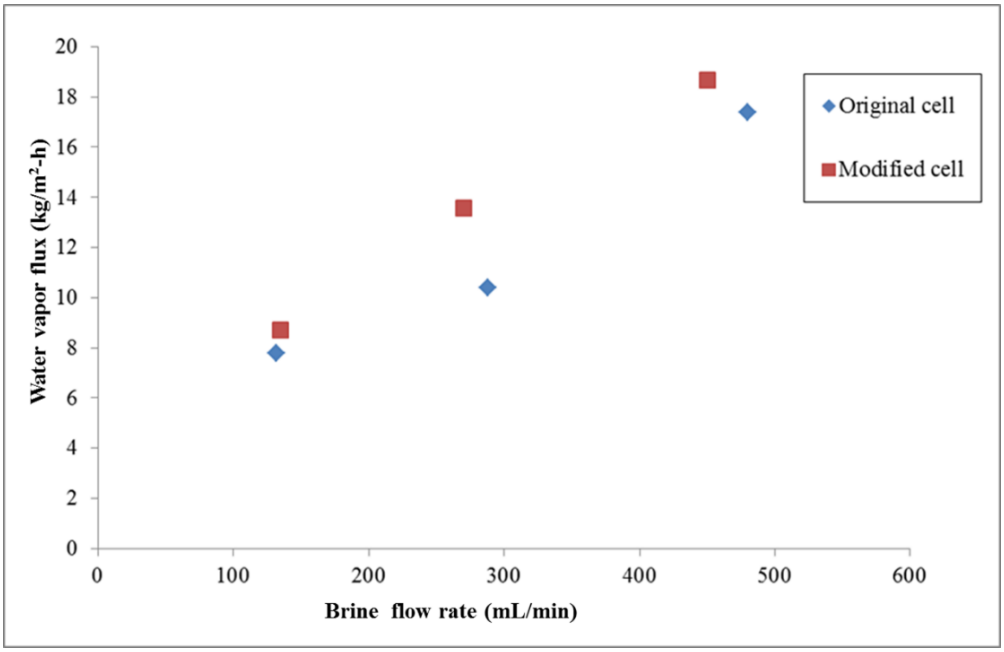

Figure 2.14 Experimental results of flux for various brine flow rates at constant brine-in and distillate-in temperatures for PVDF HVHP04700 membrane in the original s.steel cell and the modified cell. Brine inlet temperature 65℃, distillate inlet temperature 20℃.

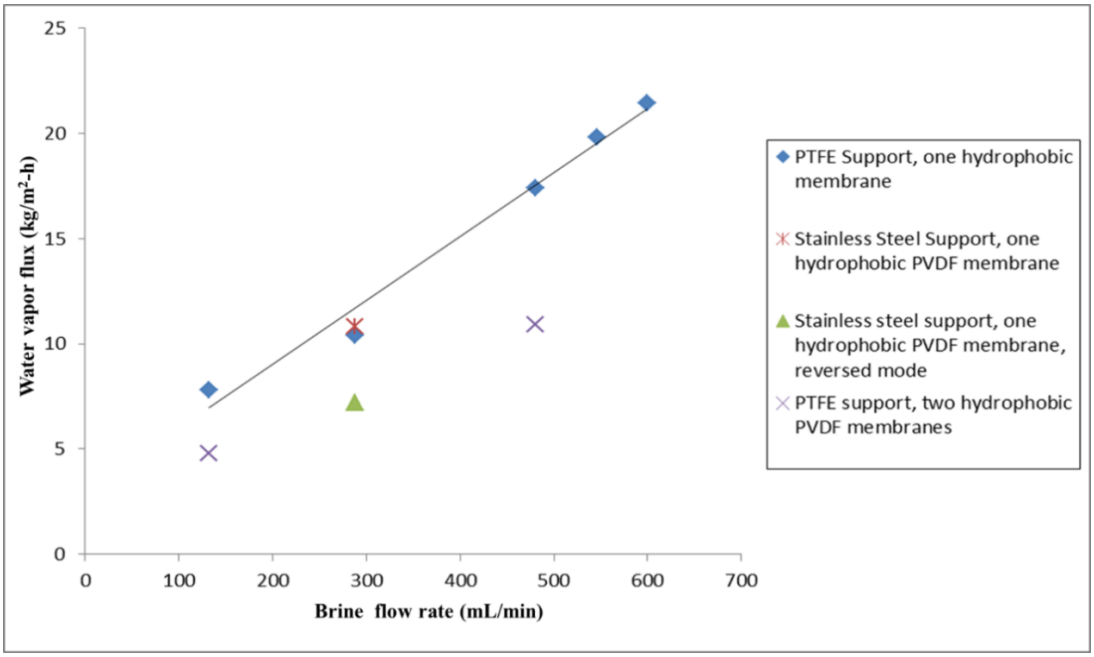

Figure 2.15 Experimental results for various brine flow rates at constant temperature. Feed brine temperature inlet 65℃, distillate inlet temperature 20℃.

2.4.3 Effect of Brine-inlet Temperature for Two Hydrophobic PVDF Membranes in Series

On the basis of experiments shown in Section 2.4.2, since the cell having a 30 mm diameter PTFE support had less sealing problem than 47 mm diameter stainless steel support, 30 mm diameter PTFE support was used to conduct experiments with two hydrophobic membranes in series (Figure 2.16). The brine-inlet temperature was varied from 65 ℃ to 80 ℃ for a brine inlet flow rate 480 mL/min, a distillate inlet flow rate 488 mL/min and distillate inlet temperature 20 ℃. At 75 ℃, the flux of one PVDF HVHP04700 (d_M 0.45 μm, δ_M 125 μm, ε_M 0.75) membrane was 29.1 kg/m^2-h, whereas the flux of two PVDF HVHP04700 (d_M 0.45 μm, δ_M 125 μm, ε_M 0.75) membranes was 17.9 kg/m^2-h, which is 61.5% of that for a single membrane. At 80 ℃, the flux of one

PVDF membrane was 37.4 kg/m^2-h, whereas the flux of two PVDF membranes was 23.2 kg/m^2-h, which is 62.0% of that for a single membrane. These results indicate that the existence of a thin air gap between two hydrophobic membranes increases the conductive heat flux resistance, this results in less than 50% reduction in flux.

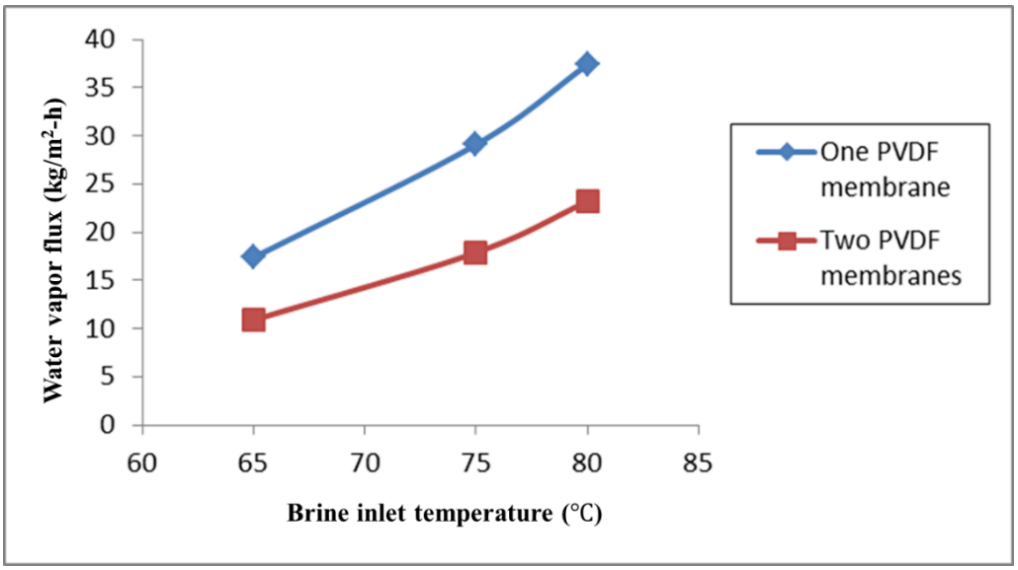

Figure 2.16 Experimental results of water vapor flux for one PVDF HVHP04700 membrane and two PVDF HVHP04700 membranes on various brine-inlet temperatures. Brine inlet flow rate 480 mL/min; distillate inlet flow rate 488 mL/min; distillate inlet temperature 20 ℃.

2.4.4 Two Hydrophobic PVDF / Hydrophilic PVDF Membranes in Series

Based on results shown in Section 2.4.3, a composite of two hydrophobic PVDF HVHP04700 (d_M 0.45 μm, δ_M 125 μm, ε_M 0.75) / hydrophilic PVDF (d_M 0.1 μm, δ_M 80 μm) membranes was used for comparison in Figure 2.17. The brine-inlet temperature range was 65 ℃ to 90 ℃; the experimental conditions were: brine inlet flow rate 480 mL/min, distillate inlet flow rate 488 mL/min, distillate inlet temperature 20 ℃. At 80 ℃,

the flux of one PVDF HVHP04700 (d_M 0.45 μm, δ_M 125 μm, ε_M 0.75) membrane was 37.4 kg/m^2-h, whereas the flux of two hydrophobic PVDF HVHP04700 (d_M 0.45 μm, δ_M 125 μm, ε_M 0.75) / hydrophilic PVDF (d_M 0.1 μm, δ_M 80 μm) membranes was 31.0 kg/m^2-h, which is 82.9% of that for a single membrane. At 90 ℃, the flux of one PVDF HVHP04700 (d_M 0.45 μm, δ_M 125 μm, ε_M 0.75) membrane was 52.4 kg/m^2-h, whereas the flux of two hydrophobic PVDF HVHP04700 (d_M 0.45 μm, δ_M 125 μm, ε_M 0.75) / hydrophilic PVDF (d_M 0.1 μm, δ_M 80 μm) membranes was 43.6 kg/m^2-h, which is 83.2% of that for a single membrane. It appeared that by adding a hydrophilic layer, whose pore size is 0.1 μm, to a hydrophobic membrane, whose pore size is 0.45 μm, reduced the water vapor flux.

M. Khayet [38] concluded that a hydrophobic/hydrophilic composite membrane consisting of thinner top-hydrophobic layer (< 10 μm) and thicker sub-hydrophilic layer (> 90 μm), whose pores are larger than that of the top-hydrophobic layer is ideal for DCMD. Further investigations might be needed by using same pore size hydrophilic and hydrophobic membranes.

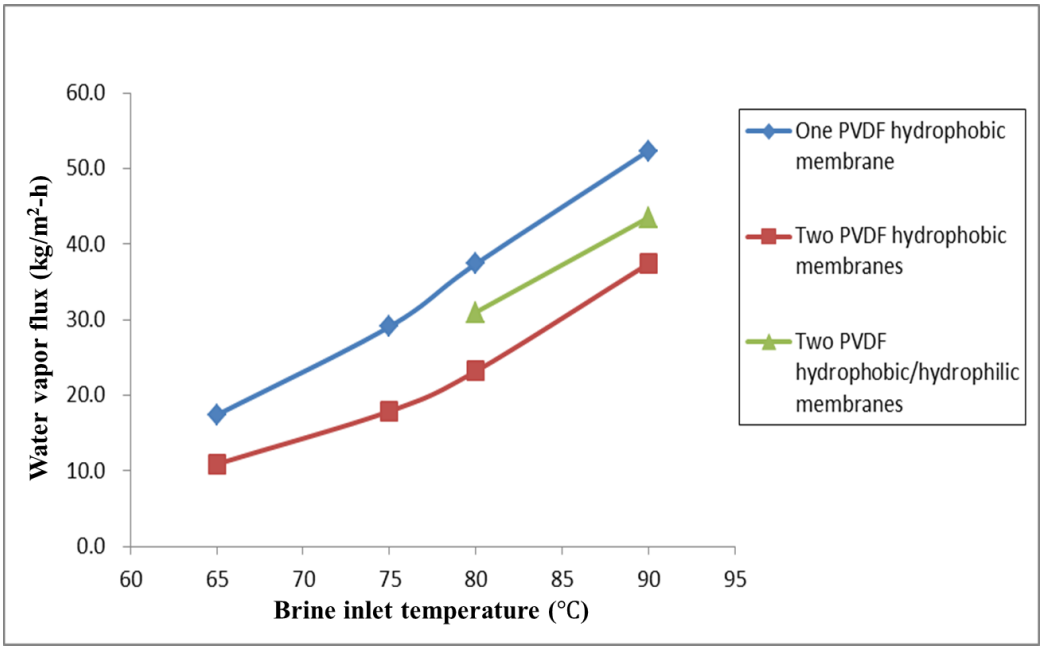

Figure 2.17 Experimental results of water vapor flux on various brine inlet temperatures for two hydrophobic PVDF HVHP04700 (d_M 0.45 μm) / hydrophilic PVDF (d_M 0.1 μm) membranes.

2.4.5 Wilson Plot in Stainless Steel Cell and CPVC Cell

The Wilson plot method yielded heat transfer correlations in the s. steel cell as well as the CPVC cell. Heat transfer correlations on the brine side for the stainless steel cell and CPVC cell are provided in Table 2.3. The heat transfer correlations on the distillate side for the stainless steel cell and CPVC cell are shown in Table 2.4. Both brine side and distillate side Wilson plots for either stainless steel cells or CPVC cells are different since the flow systems are different. However, the membrane mass transfer coefficients obtained from these plots were very close. Most experimental and simulation results were obtained using Wilson plots in CPVC cell since heat loss to the ambient was drastically reduced.

Table 2.3 Brine Side Heat Transfer Correlations*

Table 2.3A Brine Side Heat Transfer Correlations in Stainless Steel Cell

Brine inlet temperature (℃)	**Brine side Wilson plot**	
65	$\frac{1}{h_0} = 0.00004\ V_b^{-0.6} + 0.0004;\ R^2 = 0.9899$	(2.55)

Table 2.3B Brine Side Heat Transfer Correlations in CPVC Cell

Brine inlet temperature (℃)	**Brine side Wilson plot**	
65	$\frac{1}{h_0} = 0.0003 v_f^{-0.6} + 0.0019;\ R^2 = 0.9975$	(2.56)
70	$\frac{1}{h_0} = 0.0003 v_f^{-0.6} + 0.0025;\ R^2 = 0.9947$	(2.57)
75	$\frac{1}{h_0} = 0.0003 v_f^{-0.6} + 0.0021;\ R^2 = 0.9863$	(2.58)
80	$\frac{1}{h_0} = 0.0003 v_f^{-0.6} + 0.0021;\ R^2 = 0.9968$	(2.59)
85	$\frac{1}{h_0} = 0.0003 v_f^{-0.6} + 0.0019;\ R^2 = 0.9965$	(2.60)

* Distillate inlet temperature ~20 ℃.

Table 2.4 Distillate Side Heat Transfer Correlations*

Table 2.4A Distillate Side Heat Transfer Correlations in Stainless Steel Cell

Brine inlet temperature (℃)	**Distillate side Wilson plot**	
65	$\frac{1}{h_0} = 0.00004\ V_b^{-0.6} + 0.0005;\ R^2 = 0.9819$	(2.61)

Table 2.4B Distillate Side Heat Transfer Correlations in CPVC Cell

Brine inlet temperature (℃)	**Distillate side Wilson plot**	
65	$\frac{1}{h_0} = 0.0003 v_d^{-0.6} + 0.0022;\ R^2 = 0.9946$	(2.62)
70	$\frac{1}{h_0} = 0.0003 v_d^{-0.6} + 0.0021;\ R^2 = 0.9844$	(2.63)
75	$\frac{1}{h_0} = 0.0003 v_d^{-0.6} + 0.0022;\ R^2 = 0.9883$	(2.64)
80	$\frac{1}{h_0} = 0.0003 v_d^{-0.6} + 0.0021;\ R^2 = 0.9943$	(2.65)
85	$\frac{1}{h_0} = 0.0003 v_d^{-0.6} + 0.0020;\ R^2 = 0.9962$	(2.66)

* Distillate inlet temperature ~20 ℃.

2.4.6 Bubble Point Test

The experimentally obtained values of maximum pore size for PVDF membranes are provided in Table 2.5. The results show that the maximum pore size may be as much as 3-4 times the nominal pore size of the membrane. The manufacturer data for maximum pore size for ePTFE membranes are also provided in Table 2.5.The ePTFE membranes were handled with same size paper (Figure 2.18A), fully wetted by IPA and placed in the cell with the paper side up. The membranes developed less wrinkles and were ready for use after removing the paper (Figure 2.18B). If wetted Gore membranes are only handled by hand or tweezers, they will get folded and wrinkled because of lack of stiffness (Figure 2.18C). False bubbles appeared resulting in test failure (Figure 2.19).

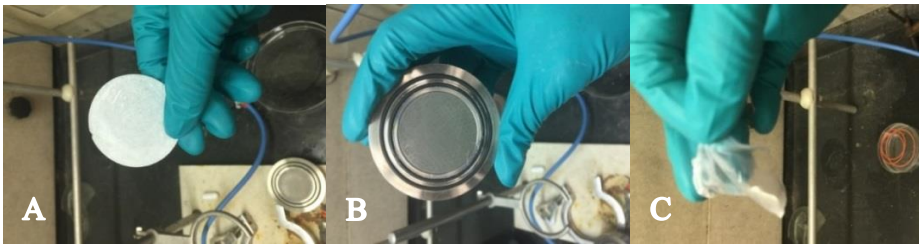

Figure 2.18 Bubble point test for ePTFE membranes.

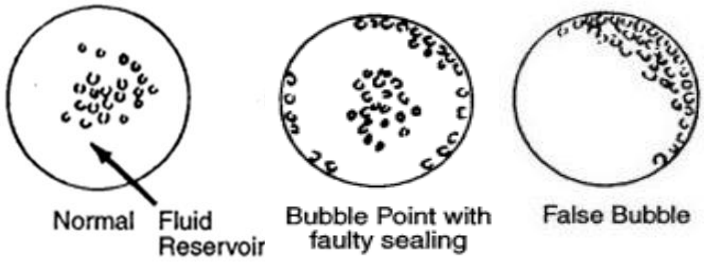

Figure 2.19 Examples of Erroneous Bubble Points.

Source: ASTM F316-03 (2011), "Standard Test Methods for Pore Size Characteristics of Membrane Filters by Bubble Point and Mean Flow Pore Test," ASTM International, West Conshohocken, PA, 2011.

Table 2.5 Bubble Point Pressure Data

	d_p (μm)	P_{BP} (data from manufacturer, psi)	P_{BP}' (experimental values, psi)	Calculated d_{max} from P_{BP} (μm)	Calculated d_{max} from P_{BP}' (μm)
ePTFE* M005	0.05	45***	N/A	0.28	N/A
ePTFE* M010	0.1	25.5***	N/A	0.49	N/A
ePTFE* M020A	0.2	17.6***	N/A	0.72	N/A
ePTFE* M020B	0.2	16***	N/A	0.79	N/A
ePTFE* M045	0.45	8.5***	N/A	1.48	N/A
PVDF** VVHP	0.1	N/A	26.7***	N/A	0.47
PVDF** GVHP	0.22	N/A	19.1***	N/A	0.66
PVDF** HVHP	0.45	N/A	10.4***	N/A	1.21

* W.L.Gore & Associates. Inc, Elkton, DE

** EMD Millipore Corp., Billerica, MA

*** Wetting liquid: Isopropyl alcohol ~20 ℃

2.4.7 Membrane Tortuosity Measurement

Experimentally determined values for membrane tortuosity are listed in Table 2.5. A treated PVDF GVHP membrane using exchange method is shown in Figure 2.20. The experimentally obtained values were close to the assumed value $(1/\varepsilon_M)$. The deviation is ~5%. Therefore, the assumption $(\chi_M = 1/\varepsilon_M)$ made for membrane tortuosity in all prediction models used above for DCMD appears to be reasonable as long as the

membrane porosity is quite high ≥0.7. Tortuosity measurement for Celgard 2400 (d_M 0.02, δ_M 25.4 μm, ε_M 0.38) was conducted to verify the experimental method; the tortuosity value obtained was 2.74 which is close to the previously reported values 2.68~3.70 [8]. Note the higher values in [8] were obtained at high pressures where the compression of the porous Celgard film is reflected in the higher end values of the tortuosity factor.

Table 2.6 Tortuosity Calculation

Membrane	**% CO_2 in permeate**	**$D_{CO_2} \times 10^9$** [39] (m^2/s)	**$S_{CO_2} \times 10^6$** [40] ($mol/m^3/Pa$)	**$Q_{CO_2} \times 10^{14}$** (m^3 (STP)-m /m^2-s-Pa)	**ΔP_{CO_2}** (kPa)	**$R_{total} \times 10^7$** (m^3 (STP)/s)	**$R_{CO_2} \times 10^9$** (m^3 (STP)/s)	**χ_M**
PVDF VVHP 04700 (d_M 0.1, δ_M 125 μm, ε_M 0.70)	0.41	1.92	365.76	1.57	100.9	1.26	5.21	1.46
PVDF GVHP 04700 (d_M 0.22, δ_M 125 μm, ε_M 0.75)	0.47	1.92	365.76	1.57	100.9	1.26	5.88	1.38
PVDF HVHP 04700 (d_M 0.45, δ_M 125 μm, ε_M 0.75)	0.50	1.92	365.76	1.57	100.8	1.26	6.31	1.29

Table 2.6 (Continued) Tortuosity Calculation

Membrane	% CO_2 in permeate	$D_{CO_2} \times 10^9$ [39] (m^2/s)	$S_{CO_2} \times 10^6$ [40] ($mol/m^3/Pa$)	$Q_{CO_2} \times 10^{14}$ (m^3 (STP)-m /m^2-s-Pa)	ΔP_{CO_2} (kPa)	$R_{total} \times 10^7$ (m^3 (STP)/s)	$R_{CO_2} \times 10^9$ (m^3 (STP)/s)	χ_M
ePTFE M-005 (d_M 0.05, δ_M 23 μm, ε_M 0.80)	3.05	1.92	365.76	1.57	98.3	1.28	30.9	1.18
ePTFE M-010 (d_M 0.1, δ_M 85 μm, ε_M 0.80)	0.80	1.92	365.76	1.57	100.5	1.37	10.9	1.16
ePTFE M-020A (d_M 0.2, δ_M 70 μm, ε_M 0.80)	1.03	1.92	365.76	1.57	100.3	1.29	13.3	1.16
ePTFE M-020B (d_M 0.2, δ_M 30 μm, ε_M 0.80)	2.33	1.92	365.76	1.57	99.0	1.29	30.1	1.18
ePTFE M-045 (d_M 0.45, δ_M 98 μm, ε_M 0.80)	0.73	1.92	365.76	1.57	100.6	1.27	9.23	1.20

Figure 2.20 A treated PVDF GVHP membrane using exchange method.

2.4.8 Comparison of Experimental and Predicted Water Vapor Flux Values at Various Brine Out Flow Rates and Distillate Out Flow Rates

The experimental and predicted water vapor flux values for different brine flow rates at various brine-in temperatures for a particular ePTFE membrane in the CPVC cell are shown in Figure 2.21. Distillate flow rate was kept at 460 mL/min; distillate inlet temperature was constant at 20 ℃. At a constant brine outlet flow rate, water vapor flux increased with increasing brine inlet temperature; at constant brine inlet temperature, water vapor flux increased with increasing brine outlet flow rate. This is because of the driving force (water vapor partial pressure difference) was increased in each case. Equation (2.8) was employed to predict the water vapor flux values. The predicted values describe the observed values quite well.

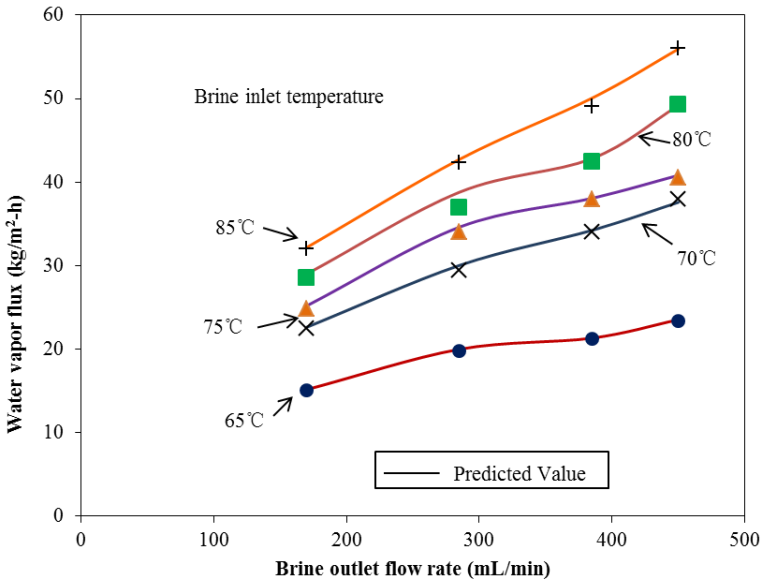

Figure 2.21 Experimental and predicted water vapor flux values for various brine flow rates at various brine-in temperatures for ePTFE M-045 membrane in the CPVC cell.

The experimental and predicted water vapor flux values for various distillate flow rates at various brine-in temperatures for the same ePTFE membrane in the CPVC cell are shown in Figure 2.22. The brine flow rate was kept at 425 mL/min; the distillate inlet temperature was constant at 20 ℃. At a constant distillate outlet flow rate, water vapor flux increased with increasing brine inlet temperature since the driving force (water vapor partial pressure difference) was increased. At a constant brine inlet temperature, water vapor flux increased slightly with increasing distillate outlet flow rate. The water vapor flux values predicted from Equation (2.8) are close to the experimental values. From Figures 2.22 and 2.23, it is clear that brine side heat transfer coefficient has a much stronger effect on water vapor flux than distillate side heat transfer coefficient. The brine side heat transfer coefficient is an important factor in achieving higher flux since the effect of temperature on water vapor pressure is much stronger at higher temperatures.

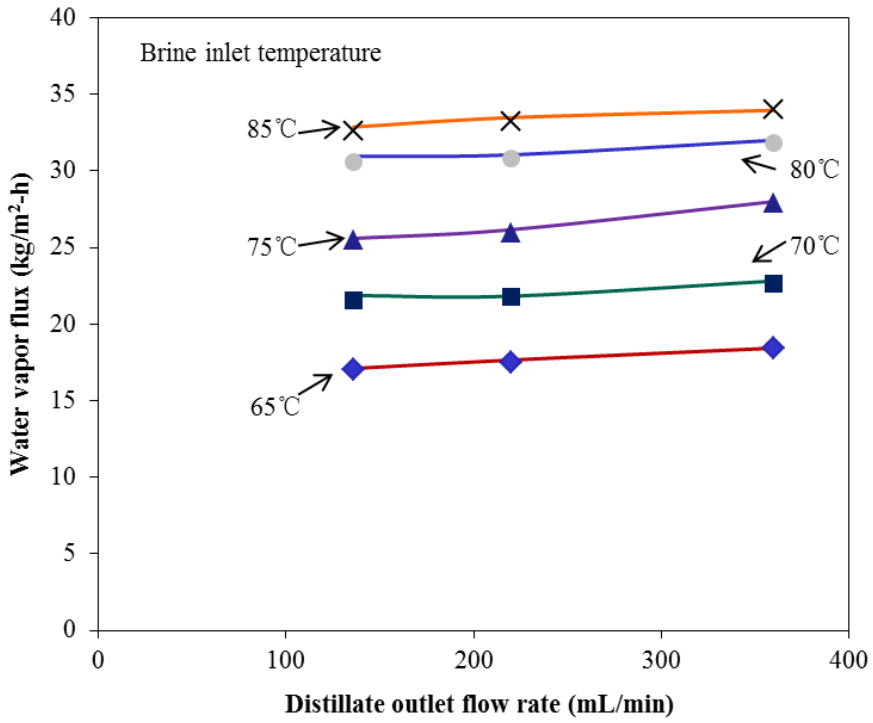

Figure 2.22 Experimental and predicted water vapor flux values for various distillate flow rates at various brine-in temperatures for ePTFE M-045 membrane in the CPVC cell.

2.4.9 Experimental and Predicted Water Vapor Flux and k_m for Different ePTFE and PVDF Membranes

The experimental and predicted water vapor fluxes for various brine flow rates at a constant brine-in temperature of 65℃ for different ePTFE and PVDF membranes in the CPVC cell are shown in Figure 2.23. The distillate flow rate was kept same as the brine flow rate; distillate inlet temperature was constant at 20 ℃. The predicted flux values for ePTFE membranes M-005 and M-010 were determined by the Knudsen diffusion model (Equation (2.5); Table 2.7).Predicted flux values for the PVDF VVHP047000 membrane were determined by the Knudsen diffusion model (Equation (2.5); Table 2.7) and the transition model (Equation (2.8); Table 2.7). For this membrane, the experimental values

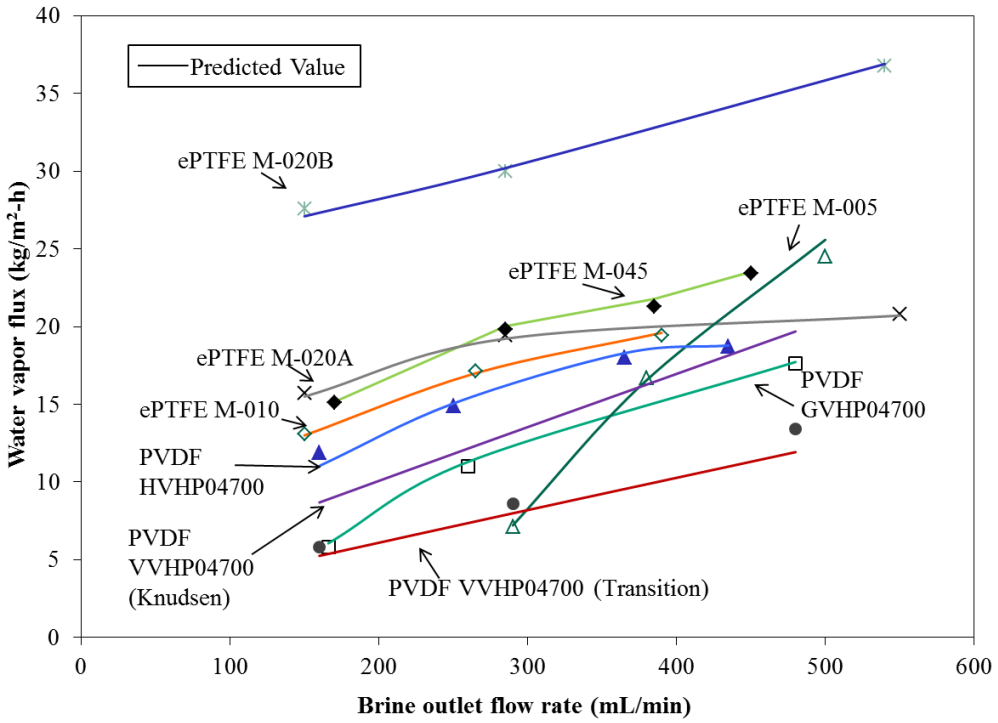

Figure 2.23 Experimental and predicted water vapor fluxes for various brine flow rates at brine-in temperature 65 ℃ for different ePTFE and PVDF membranes in the CPVC cell.

are not predicted well by either model. The flux values for other membranes were determined by the transition model (Equation (2.8); Table 2.7). Comparing ePTFE membranes M-020B and M-020A having the same pore size and different thicknesses, membrane M-020B (d_M 0.2, δ_M 30 μm, ε_M 0.80) shows much higher flux because it is much thinner than M-020A (d_M 0.2, δ_M 70 μm, ε_M 0.80). Comparing PVDF membranes HVHP04700 (d_M 0.45, δ_M 125 μm, ε_M 0.75), GVHP04700 (d_M 0.22, δ_M 125 μm, ε_M 0.75) and VVHP04700 (d_M 0.1, δ_M 125 μm, ε_M 0.70) having the same thickness and different pore sizes, the water vapor flux increased with increasing membrane pore size. It appears that the predicted flux values are in reasonable agreement with the measured

values with deviation less than 5% for all membranes except the PVDF VVHP04700 membrane.

Figure 2.24 shows the experimental and predicted values of the membrane mass transfer coefficient, k_m, for various membrane mean temperatures for different ePTFE and PVDF membranes in the stainless steel cell and CPVC cell. Predicted k_m values of M-005 and M-010 were calculated using the Knudsen diffusion model (Equation (2.5); Table 2.7). Any other predicted k_m values for other membranes shown in Figure 2.25 were determined using the transitional region model for Knudsen diffusion and molecular diffusion (Equation (2.8); Table 2.7). Different k_m values were achieved at different brine inlet temperatures in either stainless steel cell or CPVC cell. The k_m values increased slightly with increasing membrane mean temperature. The values of tortuosity for all the membranes were assumed to be $1/\varepsilon_M$. The predicted values of k_m are comparable to the experimentally obtained values. The deviation is within 5%.

Table 2.7 DCMD Prediction Model Used for Each Hydrophobic Membrane

Membrane	d_p (μm)	K_n	**Prediction model for *J***
PVDF (VVHP04700)**	0.1	1.058	Knudsen diffusion, Equation (2.5); Transition region between Knudsen and molecular diffusion, Equation (2.8)
PVDF (GVHP04700) **	0.22	0.482	Transition region between Knudsen and molecular diffusion, Equation (2.8)
PVDF (HVHP04700) **	0.45	0.235	Transition region between Knudsen and molecular diffusion, Equation (2.8)
ePTFE (M-005)*	0.05	2.116	Knudsen diffusion, Equation (2.5)
ePTFE (M-010) *	0.1	1.058	Knudsen diffusion, Equation (2.5)
ePTFE (M-020A) *	0.2	0.529	Transition region between Knudsen and molecular diffusion, Equation (2.8)
ePTFE (M-020B) *	0.2	0.529	Transition region between Knudsen and molecular diffusion, Equation (2.8)
ePTFE (M-045) *	0.45	0.235	Transition region between Knudsen and molecular diffusion, Equation (2.8)

*: EMD Millipore, Billerica, MA; **: W. L. Gore & Associates, Inc., Newark, DE

K_n is calculated based on T_m = 40 ℃, $\lambda_{w\text{-}a}$ = 0.106 um.

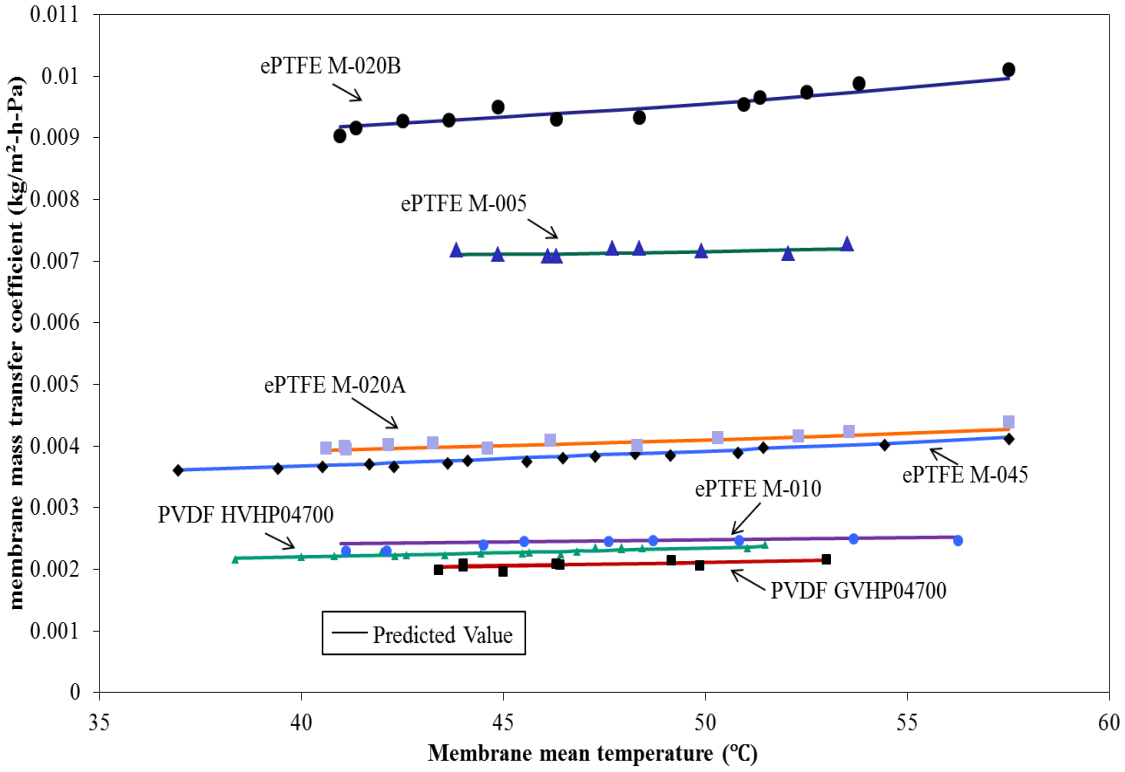

Figure 2.24 Experimental and predicted k_m for various membrane mean temperatures for different ePTFE and PVDF membranes in the stainless steel cell and the CPVC cell.

Figure 2.25 illustrates the experimental and predicted k_m values for various membrane mean temperatures for the PVDF VVHP04700 membrane in the CPVC cell. Predicted k_m values were calculated using Knudsen diffusion model (Equation (2.5); Table 2.7) and transition model for the regime in between of Knudsen diffusion and molecular diffusion (Equation (2.8); Table 2.7). Different k_m values were achieved at different brine inlet temperatures. The k_m values increased with increasing the membrane mean temperature. The tortuosity was assumed to be $1/\varepsilon_M$. The experimental k_m values are higher than predicted values using the transition model and much lower than those predicted by Knudsen diffusion values. Large pore size (0.47 µm (Table 2.5); K_n = 0.226

at 40 ℃) was observed during bubble point tests with the membrane. The pore size distribution was not measured. The few numbers of the larger pores might explain why the prediction from neither Knudsen diffusion model nor the transition model describes well the mass transfer coefficient of the PVDF VVHP04700 membrane.

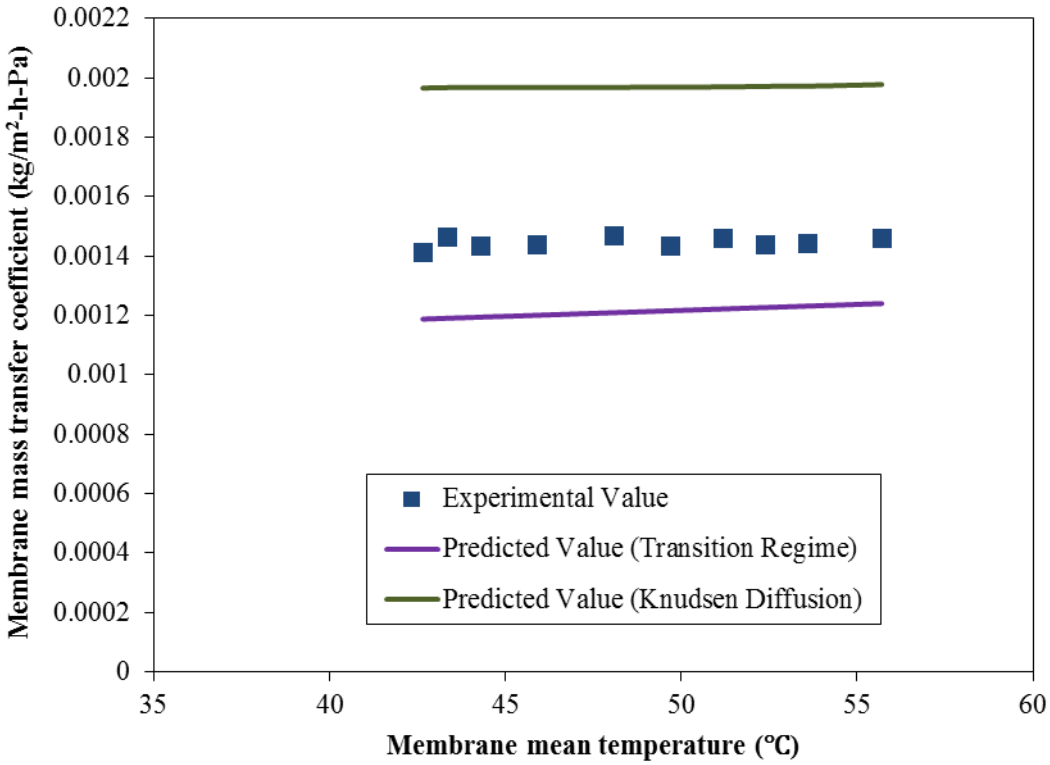

Figure 2.25 Experimental and predicted k_m for various membrane mean temperatures for the PVDF membrane VVHP04700 in the CPVC cell.

2.4.10 Water Vapor Flux Prediction Using Transition Model and Knudsen Model for K_n = 1

Phattaranawik et al. [27] had indicated limited effect of pore size distribution for the membranes they studied (d_p 0.2 μm, 0.22 μm and 0.45μm). In the present study, it

appears that pore size distribution does not matter if the range of membrane pore size entirely falls in Knudsen diffusion regime (K_n>1, d_p<λ) or the transition regime for Knudsen diffusion/ordinary molecular diffusion (0.01<K_n <1, λ <d_p<100λ). However, for membranes having nominal size ≅ 0.1 μm, K_n ≅ 1, the pore size distribution appears to play an important role in DCMD. Further investigation is needed for membranes having pore size close to the mean free path of water vapor and air (~K_n ≅ 1).

When K_n =1, the flux values predicted by Knudsen diffusion and transition region should be identical since at 70℃ the value of λ_{w-a} is equal to the nominal pore size of ePTFE M-020B membrane. However, in DCMD under practical operating conditions, the temperatures on two sides of the membrane are different leading up to the values of water vapor flux shown in Figure 2.26 for different values of ΔT = 10, 20, 30 and 40℃ and correspondingly different membrane mean temperatures. The mean free path of water vapor and air increases with increasing membrane mean temperature. Under this condition, to maintain K_n = 1, the membrane pore size has to be increased which results in deviation between the transition model and the Knudsen model.

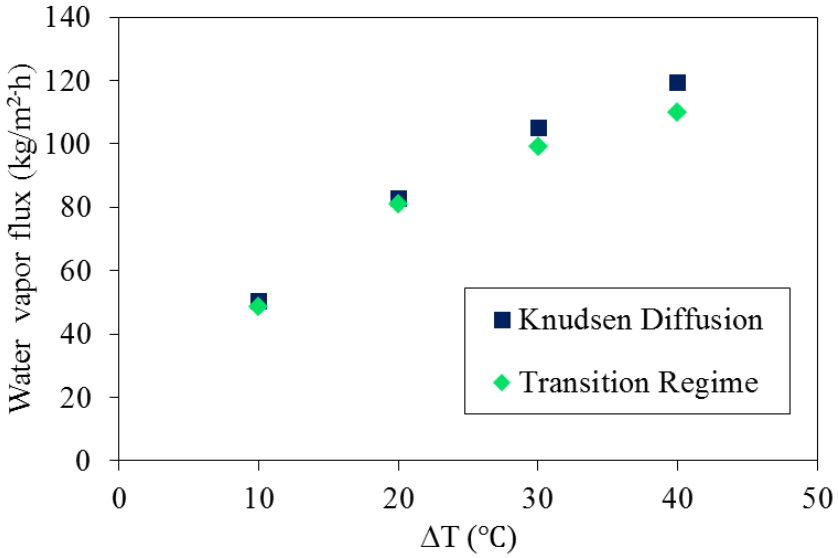

Figure 2.26 Water vapor flux predicted by the transition model and Knudsen model for K_n = 1 and T_1 = 70 ℃ and ΔT = 10, 20, 30 and 40 ℃ for ePTFE M-020B membrane.

2.4.11 Experimental and Simulation Results of Water Vapor Flux and Thermal Efficiency

It is useful to speculate on the effect of membrane thickness on water vapor flux in DCMD as conductive heat flux increases with a decrease in membrane thickness. Simulation for membrane thickness less than 5 μm was not carried out since orifice flow mechanism needs to be taken into account as the thickness is drastically reduced. Simulation results of water vapor flux (solid line) and thermal efficiency (dashed line) for brine side heat transfer coefficient h_f ranging between 200 W/m^2-K to 1200 W/m^2-K for various membrane thicknesses are shown in Figure 2.27. Parameters used in simulation are shown in the figure legend. The water vapor flux increased with a decrease in membrane thickness from 200 μm to 8 μm, and appears to become flat from 8 μm to 5 μm as a result of the balancing effect of a thin membrane on conductive heat loss. The

thermal efficiency increased as the thickness increased from 5 μm to 200 μm. A membrane thickness of 20 μm appears to provide high water vapor flux and not too low a thermal efficiency.

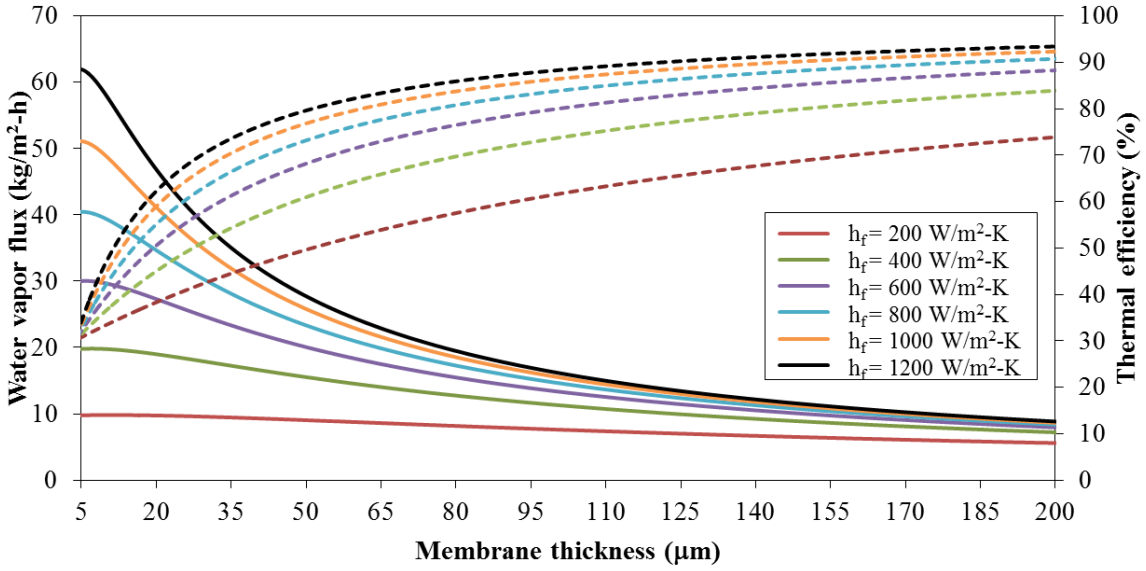

Figure 2.27 Simulation results of water vapor flux (solid line) and thermal efficiency (dashed line) for a h_f range of 200-1200 W/m^2-K for various membrane thicknesses. Simulation parameters: d_M , 0.45 μm; ε_M , 0.8; χ_M 1.25; brine mean temperature 65℃; distillate mean temperature 25℃.

Figure 2.28 illustrates the experimental and predicted thermal efficiency values for PVDF and ePTFE membranes at a h_f value of 600 W/m^2-K. Parameters used in the simulation are shown in the figure. The values of the thermal conductivity k_{mt} for all membranes are listed in Table 2.2. It is clear that thermal efficiency decreases with decreasing membrane thickness. The experimental value of thermal efficiency was: 79.7% for PVDF HVHP04700 membrane (d_M 0.45, δ_M 125 μm, ε_M 0.75) and 50.6% for ePTFE M-005(d_M 0.05, δ_M 23 μm, ε_M 0.80). The experimental values of thermal efficiency

calculated from Equations (2.54) are slightly lower (within 5%) than the predicted value. The reason is that brine mean temperature was assumed to be equal to brine inlet temperature in the simulation program. However, the brine mean temperatures were 1 ~ 2 ℃ lower than the brine inlet temperature in the experiments. A membrane thickness of 150~200 μm appears to provides very close to the highest thermal efficiency.

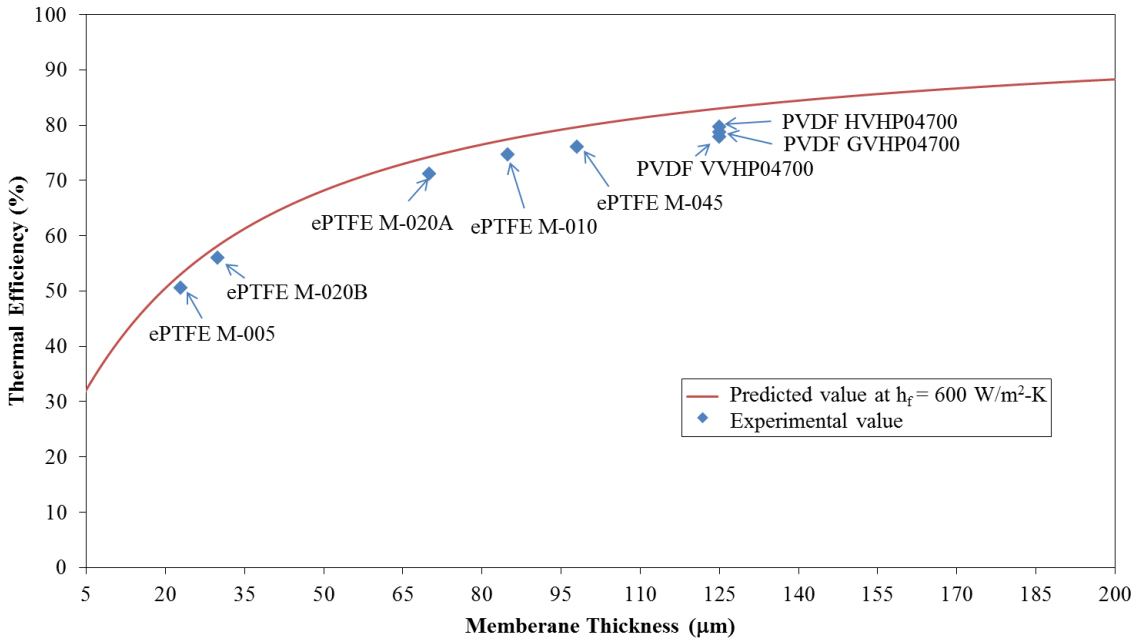

Figure 2.28 Experimental and simulated thermal efficiency results for different membranes. Brine outlet flow rate 260 mL/min; distillate outlet flow rate 280 mL/min; brine inlet temperature 65 ℃.

From Figures 2.27 and 2.28, it should be noted that one should not only pay attention to water vapor flux performance, but also need to focus on thermal efficiency. It was observed that thermal efficiency values as high as 88% in the countercurrent configuration of cross flow hollow fiber devices [41] was achieved primarily due to the

small temperature difference between the hot brine and the colder distillate in individual DCMD membrane modules; it is worth noting that the hollow fiber membrane wall thickness was 150 μm.

2.4.12 Simulation Results of Water Vapor Flux and Thermal Efficiency for Various Values of ΔT, Temperature Difference between Two Membrane Surfaces

For a thin membrane (d_M 0.45, δ_M 15 μm, ε_M 0.8), the result of simulating the effects of ΔT (temperature difference between two sides of the membrane) on water vapor and thermal efficiency are shown in Figure 2.29 for a h_f value of 600 W/m^2-K. Thermal efficiency decreases with increasing ΔT because conductive heat loss is enhanced. Water vapor flux increases with increasing ΔT because the driving force for mass transport is increased. At ΔT ~5 ℃, the value of thermal efficiency was 70.3%, while the value of water vapor flux was 22.9 kg/m^2-h.

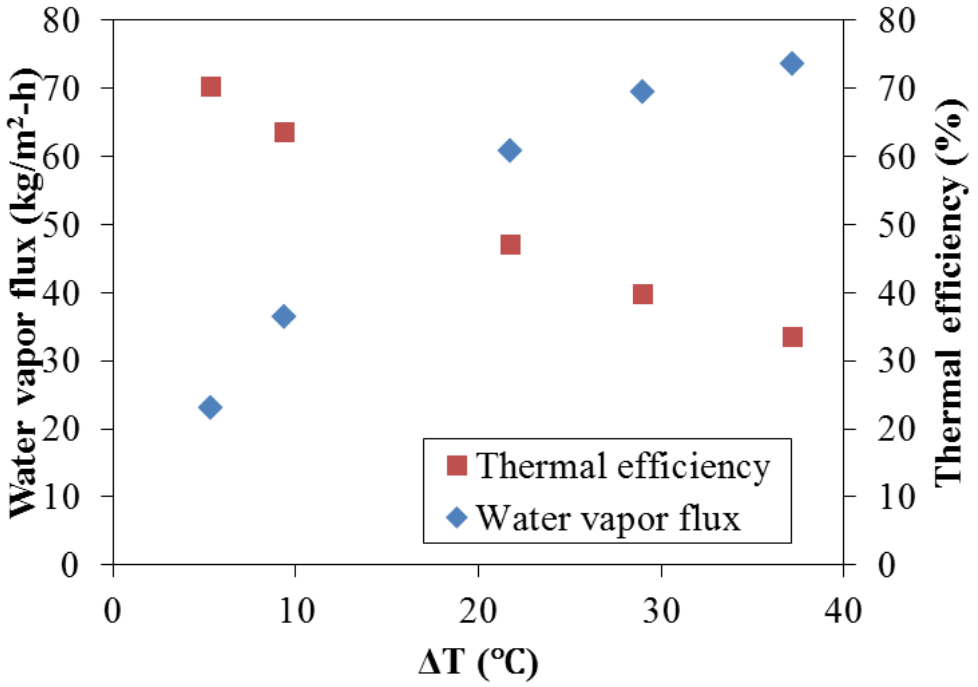

Figure 2.29 Simulation results of water vapor flux and thermal efficiency for various values of ΔT, temperature difference between two membrane surfaces. δ_M, 15 μm; d_M, 0.45 μm; ε_M, 0.8, χ_M, 1.25; brine mean temperature, 65℃; distillate mean temperature, 25℃; brine side heat transfer coefficient h_f, 600 W/m^2-K.

2.4.13 DCMD Experiments for Degassed Incoming Distillate Stream

Using degassed incoming distillate water, DCMD experiments were also performed with an ePTFE membrane, M-045(d_M 0.45, δ_M 98 μm, ε_M 0.80); (d_M 0.2, δ_M 70 μm, ε_M 0.80), in the CPVC cell. No remarkable differences were observed with respect to the flux in conventional operation without degassing. The experimental conditions were: brine outlet flow rate, 250 mL/min, distillate outlet flow rate, 245 mL/min, brine inlet temperatures, 65℃ and 85 ℃, distillate inlet temperature, 20 ℃. Vacuum pressure was at 13.3 kPa which is 87% of full vacuum. In the present study air flux does not appear to affect the prediction of water vapor flux in DCMD experiments using only degassed incoming

distillate water. Further investigation is needed to fully degas both feed side and distillate side. Relatively low solubility of air in feed brine and higher solubility of air in the cold distillate establish the air pressure gradients accompanied with water vapor partial pressure on two sides of the membrane to maintain a total pressure 1 atm.

2.5 Concluding Remarks

Membrane distillation has been known since 1963 [10] and is not yet extensively implemented in industry. A clearer understanding of the mass transfer mechanisms, the role of various membrane properties, air flux and pore size distribution is expected to facilitate the development of DCMD.

In the present study, Wilson plot technique was used to determine the heat transfer coefficients on the two sides of the flat membrane in the DCMD cells for unknown heat transfer conditions in the hot brine and the cold distillate sides. This allowed experimental determination of the membrane-liquid interface temperatures and thereby the membrane mass transfer coefficients k_m for water vapor. Available model equations for Knudsen diffusion region and transition region for Knudsen diffusion/molecular diffusion were utilized to predict the membrane mass transfer coefficient for a variety of ePTFE and PVDF membranes. The predicted values were quite close to the values of k_m determined via Wilson plot technique from the experimental data in either stainless steel or CPVC cell. The assumption of membrane

pore tortuosity of $\chi_M = 1/\varepsilon_M$ appears to be valid for the membranes having high porosity (ε_M > 0.7) used here.

It appears that pore size distribution does not matter if the ranges of membrane pore size entirely falls entirely in the Knudsen diffusion (K_n>1, d_p<λ) or transition regime for Knudsen diffusion/ordinary molecular diffusion (0.01< K_n <1, λ < d_p< 100λ). However, for membranes having nominal size ≅ 0.1 μm, K_n ≅ 1, the pore size distribution plays an important role in DCMD. Further investigations are needed for membranes having pore size close to the mean free path of water vapor and air (~K_n ≅ 1). In the present study, the small air flux did not appear to affect the value of the water vapor flux in DCMD experiments using only degassed incoming distillate water. The ideal membrane properties for DCMD are large pore size, high porosity, and low membrane thickness (~20 μm) to achieve high water vapor flux while balancing thermal efficiency in DCMD. For higher thermal efficiency, a larger thickness ~150 - 200 μm is necessary when temperature difference on two sides of the membrane is larger than 10 ℃. To achieve high thermal efficiency for thin membranes around 10 ~ 20 μm, the temperature difference on two sides of the membrane should be quite low.

CHAPTER 3

VACUUM MEMBRANE DISTILLATION

3.1 Theory

In VMD - based desalination (Figure 3.1), a porous hydrophobic membrane serves as the boundary between the hot brine and vacuum. Water vapor diffuses when the partial pressure of water vapor on the brine side is higher than the vacuum pressure. Membrane porosity is generally high to provide membrane high permeability. Membrane pore size especially membrane maximum pore size, is a critical factor: it should be large enough to deliver high membrane permeability, but also should be relatively small to prevent pore wetting. Liquid entry pressure (LEP) and bubble point experiments are two common methods to determine the relation of membrane wetting and membrane maximum pore size. The vacuum level should be sufficiently high to provide enough difference in water vapor partial pressure between the two sides of membrane and be comparable with those in other MD methods. But the energy consumption required by vacuum should also be taken into account. Therefore, membrane properties and operating conditions play important roles in mass transfer and heat transfer in VMD.

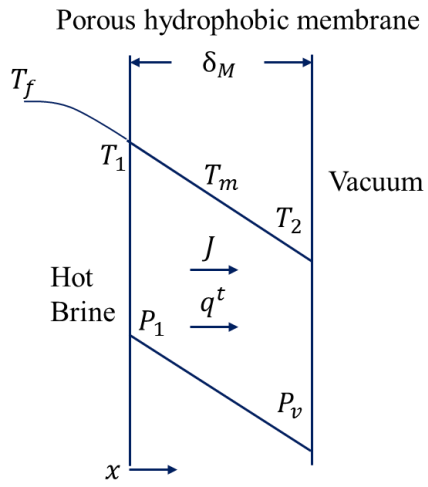

Figure 3.1 Vacuum membrane distillation (VMD).

3.1.1 Mass Transfer

The mass transfer mechanism strongly depends on the Knudsen number (K_n) :

$$K_n = \frac{\lambda_w}{d_p} \tag{3.1}$$

where λ_w is the mean free path of water vapor and air and d_p is the nominal membrane pore diameter. For pure water vapor, the mean free path is expressed by

$$\lambda_w = \frac{k_B T_m}{\sqrt{2}\pi P_m {\sigma_w}^2} \tag{3.2}$$

where k_B is the Boltzmann constant; P_m is mean of the pressure on the brine side of membrane and vacuum pressure on the other side; σ_w is the collision diameter for water vapor (2.641×10^{-10} m); T_m is the membrane mean surface temperature which is assumed to be equal to that of the brine side of the membrane.

If the mean free path of the molecules is larger than membrane pore size (K_n>1, d_p<λ), molecule – pore wall collisions are dominant and Knudsen diffusion model should

be considered. If K_n<0.01, d_p>100 λ, molecular diffusion is used to describe the mass transport in the continuum region; consider stagnant air trapped within membrane pores due to the low solubility of air in water. If 0.01<K_n <1, λ <d_p<100λ, the mass transport mechanism is in transitional region which could be described by combined Knudsen diffusion model and ordinary molecular diffusion flow model. It is notable that all values of mean free path for pure water vapor at T_m values from 40℃ - 80 ℃ are larger than 1 with a vacuum pressure of 7600 Pa; therefore, Knudsen diffusion model is considered for membranes having pore sizes in the range of 0.05 μm - 0.45 μm (Table 3.1).

Table 3.1 Mean Free Path for Pure Water Vapor for Different Values of T_m

$\mathbf{d_p}$ (μm)	$\boldsymbol{T_m}$ (℃)	$\mathbf{P_1}$ (Pa)	$\mathbf{P_2}$ (Pa)	$\mathbf{P_m}$ (Pa)	$\boldsymbol{\lambda_w}$ (μm)	$\mathbf{K_n}$
	40	6495.1	7600	7047.6	1.98	39.6
0.05	60	10861.8	7600	9230.9	1.61	32.2
	80	17538.5	7600	12569.3	1.25	25.1
	40	6495.1	7600	7047.6	1.98	19.8
0.1	60	10861.8	7600	9230.9	1.61	16.1
	80	17538.5	7600	12569.3	1.25	12.5
	40	6495.1	7600	7047.6	1.98	9.9
0.2	60	10861.8	7600	9230.9	1.61	8.0
	80	17538.5	7600	12569.3	1.25	6.3

Table 3.1 (Continued) Mean Free Path for Pure Water Vapor for Different Values of T_m

$\mathbf{d}_p$ (μm)	T_m (℃)	$\mathbf{P}_1$ (Pa)	$\mathbf{P}_2$ (Pa)	$\mathbf{P}_m$ (Pa)	$\boldsymbol{\lambda}_w$ (μm)	$\mathbf{K}_n$
	40	6495.1	7600	7047.6	1.98	4.4
0.45	60	10861.8	7600	9230.9	1.61	3.6
	80	17538.5	7600	12569.3	1.25	2.8

In the VMD process, the pressure on the membrane surface of the permeate side is equal to the vacuum level on the permeate side; therefore

$$P_{w,2} = P_v \tag{3.3}$$

The water vapor partial pressure on the feed side ($P_{w,1}$) can be expressed as

$$P_{w,1} = x_w \gamma_w P_{w,1}^0 \tag{3.4}$$

Here x_w is the mole fraction of water on the membrane surface; γ_w is the activity coefficient of water on the membrane surface; $P_{w,1}^0$ is the actual water vapor pressure. For NaCl solution, γ_w can be expressed as [45]:

$$\gamma_w = 1 - 0.5x_{NaCl} - 10x_{NaCl}^2 \tag{3.5}$$

For dilute NaCl solution (1 wt% NaCl), the actual water vapor partial pressure is considered equal to pure water vapor partial pressure neglecting the very limited effect of salt on water vapor pressure:

$$P_{w,1} = P_{w,1}^0 \tag{3.6}$$

The values of $P_{w,1}$ are calculated from T_1 by Antoine equation

$$\log_{10} P(mm\ Hg) = 8.017 - \frac{1730.6}{233.426 + T(℃)} \tag{3.7}$$

The general mass transfer expression for water vapor flux J in VMD can be expressed as

$$J = k_m \left(P_{w,1} - P_v\right) \tag{3.8}$$

3.1.1.1 Knudsen Diffusion. The mass transfer model for Knudsen diffusion (K_n > 1, d_p < λ_w) can be expressed for a membrane of thickness δ_M by

$$J = \frac{D_{Kn}}{RT_m} \times \frac{\left(P_{w,1} - P_{w,2}\right)}{\delta_M} \tag{3.9}$$

$$J = \frac{D_{Kn}}{RT_m} \times \frac{\left(P_{w,1} - P_v\right)}{\delta_M} \tag{3.10}$$

where D_{Kn} is the Knudsen diffusivity

$$D_{Kn} = \frac{4}{3} \frac{\varepsilon_M d_p}{\chi_M} \sqrt{\frac{RT_m}{2\pi M_w}} \tag{3.11}$$

M_w is molecular weight of water, R is the universal gas constant.

For membranes having a porosity $\varepsilon_M \geq 0.70$, membrane tortuosity χ_M can be expressed as [33]

$$\chi_M = \frac{1}{\varepsilon_M} \tag{3.12}$$

Experimental values of χ_M were determined in earlier studies by a solvent exchange method [8,9, Sub-section 2.2.2.4].

3.1.1.2 The Dusty-gas Model (DGM). The Dusty-gas Model (DGM) considers the effect of the porous media as a "dusty gas" component of the gas mixture. It is assumed

to consist of large molecules fixed in space that is treated as a component of the gas mixture. The kinetic theory of gases is applied to this dusty-gas mixture. For single gas transport, the water vapor flux can be calculated from

$$J = \frac{1}{RT\delta_M}\left[K_0\left(\frac{8RT}{\pi M_W}\right)^{0.5} + B_0\left(\frac{P_m}{\mu}\right)\right](P_1 - P_v) \tag{3.13}$$

The value for water vapor viscosity, μ, e.g., at 40°C is 0.653×10^{-3} Pa · s; K_0 and B_0 are functions of membrane properties

$$K_0 = \frac{\varepsilon_M d_p}{3\chi_M};\ B_0 = \frac{\varepsilon_M {d_p}^2}{32\chi_M} \tag{3.14}$$

where membrane porosity is ε_M and membrane tortuosity is χ_M.

3.1.2 Heat Transfer

In VMD - based desalination, water evaporated from the hot brine reduces the membrane surface temperature from the bulk brine temperature. This temperature reduction is the source of temperature polarization; it results in decreased water vapor partial pressure difference across the membrane thus decreasing the water vapor flux.

Assuming that there is no heat loss to the ambient, the total heat transfer rate Q_t is equal to the brine side heat transfer rate

$$Q_t = \mathrm{q}^t \times A_m \tag{3.15}$$

$$Q_b = \rho_b C_{pb} F_{bi} T_{bi} - \rho_b C_{pb} F_{bo} T_{bo} \tag{3.16}$$

$$Q_t = Q_b \tag{3.17}$$

Further

$$F_p = F_{bi} - F_{bo} \tag{3.18}$$

where F_p is the volumetric condensate flow rate.

Here, total heat flux q^t based on the brine side heat flux q_f can be expressed as:

$$q^t = \frac{\rho_b C_{pb} F_{bi} T_{bi} - \rho_b C_{pb} F_{bo} T_{bo}}{A_m} \tag{3.19}$$

$$q_f = h_f (T_f - T_1) \tag{3.20}$$

where h_f is the brine side heat transfer coefficient; further

$$q^t = q_f = q_m \tag{3.21}$$

The hot brine side average temperature (K) is assumed as

$$T_f = (T_{bi} + T_{bo})/2 \tag{3.22}$$

Assuming no heat loss to the ambient from the permeate side, we can assume that temperatures on two sides of membrane surface are essentially equal:

$$T_1 = T_2 = T_m \tag{3.23}$$

Generally in MD, the total heat transfer resistance has three contributions: brine side heat transfer resistance, membrane heat transfer resistance, and condenser side heat transfer resistance; in VMD, vacuum side heat transfer resistance is minimal.

Heat transfer across the membrane in MD is generally contributed by: latent heat and sensible heat transfer associated with water vapor flux; the conductive heat transfer across the membrane. The latter is considered heat loss in MD.

$$q_m = JH_v(T) - k_{mt} \frac{dT}{dx} \tag{3.24}$$

where $H_v(T)$ is the enthalpy of water vapor which includes the latent heat of vaporization for water and sensible heat above 0℃, and k_{mt} is the thermal conductivity of the membrane.

In VMD, the following assumption is made:

$$k_{mt}\frac{dT}{dx} = 0 \tag{3.25}$$

Therefore

$$q_m = JH_v(T) \tag{3.26}$$

Wilson plot was applied to determine the brine side heat transfer coefficient and the brine side membrane surface temperature. Wilson plot method [37] was developed to evaluate convective heat transfer coefficients in shell and tube condensers. It avoids direct measurement of surface temperatures and consequently the disturbances to fluid flow. In this study, the brine side Wilson plot equations from the previous DCMD study described in Section 2.2.2.4 are employed to determine the boundary layer heat transfer coefficient (h_f) and the membrane surface temperatures (T_1) in VMD. Detailed methods are not shown here. For fully developed flow, the heat transfer coefficient may be assumed to be proportional to a power of the brine velocity which could be expressed by

$$h_f = a{v_f}^n \tag{3.27}$$

where a is a constant, v_f is the brine side velocity and n is the corresponding velocity exponent.

3.2 Experimental

3.2.1 Materials and Chemicals

Porous hydrophobic PVDF and expanded-PTFE (ePTFE) flat sheet membranes employed in VMD are the same as those used DCMD, which are listed in Sub-section 2.2.1.1.

3.2.2 Apparatus for VMD Experiments and Experimental Procedure

The VMD experiments were performed with hydrophobic flat sheet membranes over a hot brine temperature range of 65 ℃ to 85 ℃ and brine flow rates varying between 100 and 500 mL/min. A schematic of the VMD setup is shown in Figure 3.2A. The NaCl solution (1% wt.) was introduced as the brine feed in a titanium vessel (Vargo, Lewisburg, PA) immersed in an oil bath (Haake A81, Thermo Fisher Scientific, Waltham, MA). It was pumped over one side of the membrane in the CPVC cell. The other side of the membrane was exposed to various vacuum levels by a vacuum pump (Model USEM 820.0, KNF Neuberger, Trenton, NJ) with a digital vacuum regulator (Model 200, J-KEM Scientific). The condensate was collected in glass vacuum traps immersed in liquid N_2. After the CPVC cell, hot brine was recycled to the brine tank. The brine tank was fitted with a liquid level controller (Warrick Series 16, Gems Sensors & Controls, Plainville, CT) to maintain constant brine concentration due to continuous vaporization of water from the hot brine feed solution into membrane pores. This liquid level controller activated a pump to take in fresh DI water from a makeup water storage tank. Figure 3.2B shows an opposite arrangement of a traditional cold trap to solve the blockage by icing

condensate: the water vapor (condensate) flows down the wall of the trap while vacuum was pulled from the inner tube.

Platinum RTD sensors (Model RTD-NPT-72-E-1/4-HH804-CONN, Omega, Stamford, CT; Accuracy:0.15 + 0.002T(°C)) connected to digital thermometers (Dual Input Pt100 Platinum RTD meter, Model HH 804, Omega, Stamford, CT; Accuracy: ± 0.05% + 0.2°C) were used to monitor the inlet and outlet temperatures of the brine stream through the CPVC cell. Inlet pressure of the brine stream was monitored by a manometer (Model 490-1, Dwyer Instruments, Michigan City, IN). The flow rate of the brine out stream was measured manually before membrane distillation flux measurements were initiated. A weighing machine was used to determine the water vapor flux by measuring the condensate mass per hour. The conductivity of the condensate was measured using a conductivity meter (Orion 115A+, Thermo Fisher Scientific, Waltham, MA). After a steady state was reached in any experiment under given conditions, it was run for around 3 hour. After each run, DI water at room temperature was passed as feed for 10 min to dissolve any salt remaining in the system. Each experiment was repeated three times to check reproducibility.

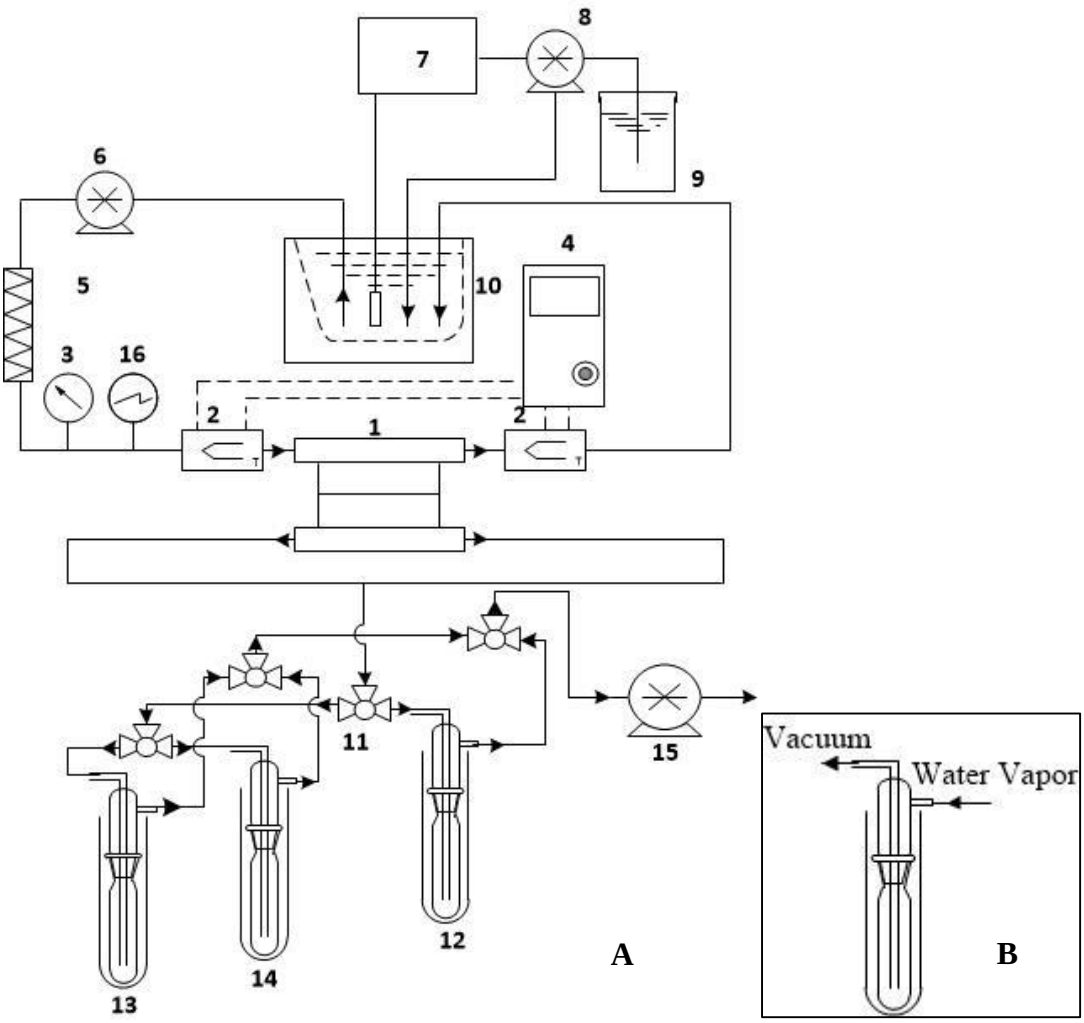

Figure 3.2A Schematic of VMD setup. 1. Membrane test cell; 2. Thermocouple; 3. Pressure indicator; 4. Digital thermometer; 5. Pre-filter; 6. Brine pump; 7. Liquid level controller; 8. Make-up pump; 9. Make-up water reservoir; 10. Brine water-bath; 11. Three-way valve; 12.Vacuum trap I; 13.Vacuum trap II; 14.Vacuum trap III; 15. Vacuum pump. 16. Digital Manometer.

Figure 3.2B Cold trap configuration. An opposite arrangement of traditional cold trap is used to solve the blockage of the icing condensate: the water vapor (condensate) flows down the wall of the trap while sucked by vacuum from the inner tube.

3.2.3 Determination of Liquid Entry Pressure (LEP)

The liquid entry pressure (LEP) of a membrane for a given liquid is defined as the minimum pressure at which a continuous flux of the liquid is observed. A schematic

drawing of LEP set up is shown on Figure 3.3. The liquid chamber (sample cylinder, part # DOT-3E 1800, Swagelok, Mountainside, NJ) was filled with 1% NaCl solution. Dry membrane was placed in the flat stainless steel cell (diameter 47mm; membrane area 13.8 cm^2; part # XX4404700, EMD Millipore, Billerica, MA). Low pressure (~20.7 kPag (3 psig)) was applied in order to remove gas at the feed side of the membrane. Pressure was raised stepwise (with 6.9 kPag (1 psig)) monitored by a 6'' test gauge (0- 1379 kPag (0-200 psig), part # 63-5622, Matheson, Montgomeryville, PA). Five samples were taken to check reproducibility.

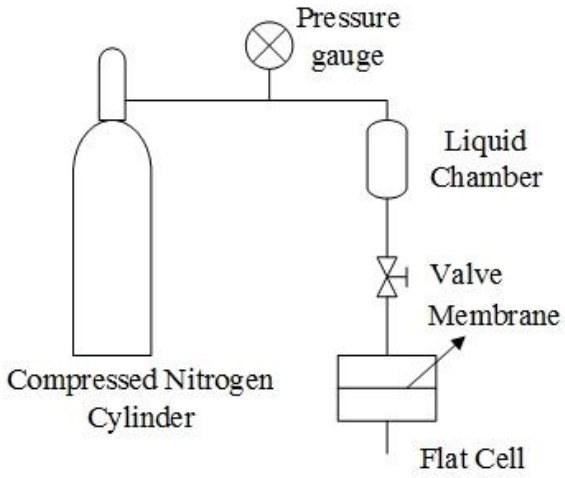

Figure 3.3 Schematic drawing of LEP set up.

Generally, LEP increases with decreasing membrane maximum pore size; LEP increases with surface porosity, r/R ratio, membrane thickness [46]. A number of studies

have focused on the models for predicting the correlation of LEP and maximum pore size, such as Young-Laplace equation

$$\Delta P = \frac{-2\gamma \cos\theta}{r_{max}} \tag{3.28}$$

Franken [47] introduced the curvature radius (B) of membrane surface pore

$$\Delta P = \frac{-2B\gamma \cos\theta}{r_{max}} \tag{3.29}$$

For PTFE, the value of B is around 0.4 to 0.6 [48].

3.3 Models Used for Prediction

3.3.1 Prediction of Water Vapor Flux and Membrane Mass Transfer Coefficient

In this study, the water vapor mass transfer coefficient (k_m) can be determined from Equation (3.8); the water vapor flux can be predicted from Knudsen diffusion using Equation (3.10) or DGM using Equation (3.13).

The membrane mass transfer coefficient obtained experimentally is given by

$$k_{m-experimental} = \frac{J_{m-experimental}}{(P_{w,1} - P_v)} \tag{3.30}$$

Here $P_{w,1}$ is obtained from Antoine equation (Equation (3.7)). Further

$$T_1 = T_f - \frac{q_f}{h_f} = T_f - \frac{\mathrm{q}^t}{h_f} = T_f - \frac{\rho C_p F_{bi} T_{bi} - \rho C_p F_{bo} T_{bo}}{A_m h_f} \tag{3.31}$$

All prediction models used here employ the nominal pore size reported by the manufacturer. The membrane tortuosity was calculated from $\chi_M = 1/\varepsilon_M$ (Equation (3.12)).

3.3.2 Prediction of Water Vapor Flux Performance vs. Membrane Thickness

From Equation (3.24), one can get

$$\int_0^{\delta_M} q_m \, dx = \int_0^{\delta_M} \left(J H_v(T)\right) dx \tag{3.32}$$

Define

$$H_v(T) = \lambda_H + C_v(T - T_0) \tag{3.33}$$

Equation (3.32) becomes

$$q_m \delta_M = J \int_0^{\delta_M} \left(\lambda_H + C_v(T - T_0)\right) dx \tag{3.34}$$

Here, temperature is assumed to be a constant at T_1

$$J C_v \int_0^{\delta_M} T \, dx = J C_v \int_0^{\delta_M} T_1 \, dx \tag{3.35}$$

Therefore

Equation (3.34) becomes

$$q_m = J\lambda_H + J C_v(T_1 - T_0) \tag{3.36}$$

Combining with Equations (3.21) and (3.23), Equation (3.36) becomes

$$h_f\left(T_f - T_1\right) = J(\lambda_H + C_v(T_m - T_0)) \tag{3.37}$$

Assume $T_f = T_{bi}$

$$J = \frac{h_f(T_{bi} - T_1)}{\lambda_H + C_v(T_m - T_0)} \tag{3.38}$$

Combine Equation (3.13) with Equation (3.38)

$$\frac{1}{RT\delta_M}\left[K_0\left(\frac{8RT}{\pi M_W}\right)^{0.5} + B_0\left(\frac{P_m}{\mu}\right)\right](P_1 - P_2) = \frac{h_f(T_{bi} - T_1)}{\lambda_H + C_v(T_1 - T_0)} \tag{3.39}$$

For a certain δ_M, there is a certain T_1, other items such as heat transfer coefficient remaining constant,

$$\delta_M = \frac{[\lambda_H + C_v(T_1 - T_0)]\left[K_0\left(\frac{8RT}{\pi M_W}\right)^{0.5} + B_0\left(\frac{P_m}{\mu}\right)\right](P_1 - P_2)}{\left[h_f(T_{bi} - T_1)\right]RT} \tag{3.40}$$

3.3.3 Thermal Efficiency

Thermal efficiency is defined as the ratio of heat transfer rate for water evaporation over total heat transfer rate:

$$\eta(\%) = \frac{Mass\ rate\ of\ water\ collection\left(\frac{g}{h}\right) \times\ latent\ heat\ of\ water\ \lambda\left(\frac{kJ}{kg}\right) \times \frac{1}{60}\left(\frac{h}{min}\right)}{Q_t\left(\frac{J}{min}\right)} \times 100 \tag{3.41}$$

In VMD, since there is essentially no heat loss, the thermal efficiency is very high (close to 100%).

3.4 Results and Discussion

3.4.1 Comparison of Experimental Values of Water Vapor Flux for VMD and DCMD

Figure 3.4 provides a comparison of experimental values of water vapor flux for VMD with these of DCMD (Figure 2.21) for ePTFE M-045 membrane at various hot brine flow rates and brine inlet temperatures. The vacuum level was 92.5% of full vacuum (7600 Pa). A very high value of water vapor flux, 150 kg/m^2-h, was achieved at a brine flow rate 280 mL/min and brine inlet temperature 85℃. The permeate conductivity was 990 μS/cm at 25℃, about 94.3% salt rejection. In the low range of brine flow rates ~180

mL/min, no salt leakage was observed (100% salt rejection) in the permeate at brine temperatures from 65℃ to 85℃. At a high temperature of 85℃, salt rejection decreased with increasing brine inlet flow rate and water vapor partial pressure difference. This is due to the following: the pressure of the entering brine is higher if the brine flow rate into the cell is higher. When this extra above-atmosphere pressure of brine is added to the vacuum level, it may exceed the liquid entry pressure for the membrane. Hence at a lower brine flow rate, there was no entry of liquid into the pores and no salt leakage. This issue is considered in detail later.

3.4.2 Experimental Values of Water Vapor Flux and Salt Leakage

Experimental values of water vapor flux and salt rejection for ePTFE M-045 for various vacuum levels are shown in Figure 3.5. Brine inlet temperature was 75℃. Brine flow rate was 280 mL/min. Four vacuum levels, 88.2%, 90%, 92.5%, 95.2% of full vacuum, were applied. At 88% of full vacuum, the water vapor flux value was 31.8 kg/m^2-h, which is lower than the DCMD experimental value of 34.0 kg/m^2-h (Figure 2.21) under the same experimental conditions on the feed brine side. This is because the vacuum pressure applied was not enough to support a high enough water vapor partial pressure difference. The values of water vapor flux increased with increasing vacuum levels as a result of the increased water vapor partial pressure difference. However, salt rejection increased rapidly with increasing vacuum level. There was no observed salt leakage (100% rejection) for the vacuum level of 88%.

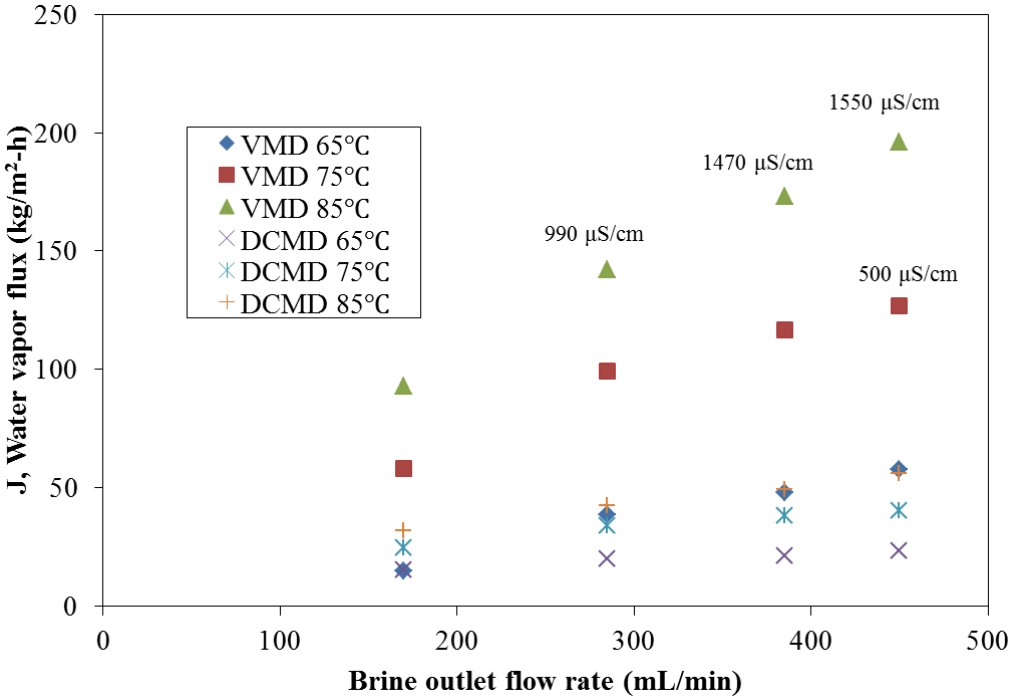

Figure 3.4 Comparison of experimental values of water vapor flux for VMD and DCMD for ePTFE M-045 at various brine flow rates and brine inlet temperatures. DCMD data are from Figure 2.21.

Figure 3.6 provides the experimental values of $J\delta_M$ and salt rejection for various membrane nominal pore sizes at 92.5% of full vacuum (7600 Pa) for all membranes at a brine flow rate of 280 mL/min and brine inlet temperature of 65°C. The value of $J\delta_M$ increases with increasing membrane nominal pore size. The salt rejection decreases with increasing membrane pore size. For membranes having nominal pore sizes 0.1 and 0.2 µm, the values of salt rejection were almost ~99%. As membrane pore size increases to 0.45 µm, the values of salt rejection decrease drastically: the salt rejection for ePTFE M-045 (d_M, 0.45) was 95.8%, while the salt rejection for PVDF HVHP (d_M, 0.45) was 97.2%.

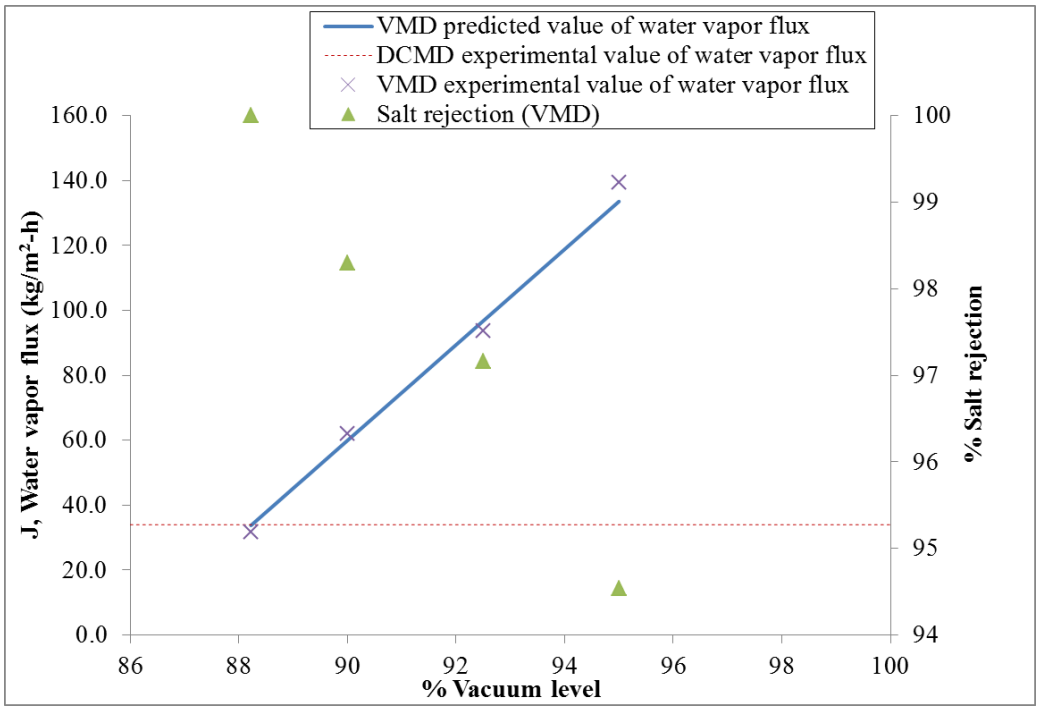

Figure 3.5 Experimental values of water vapor flux and salt rejection for ePTFE M-045 at various vacuum levels. DCMD data are from Figure 2.21.

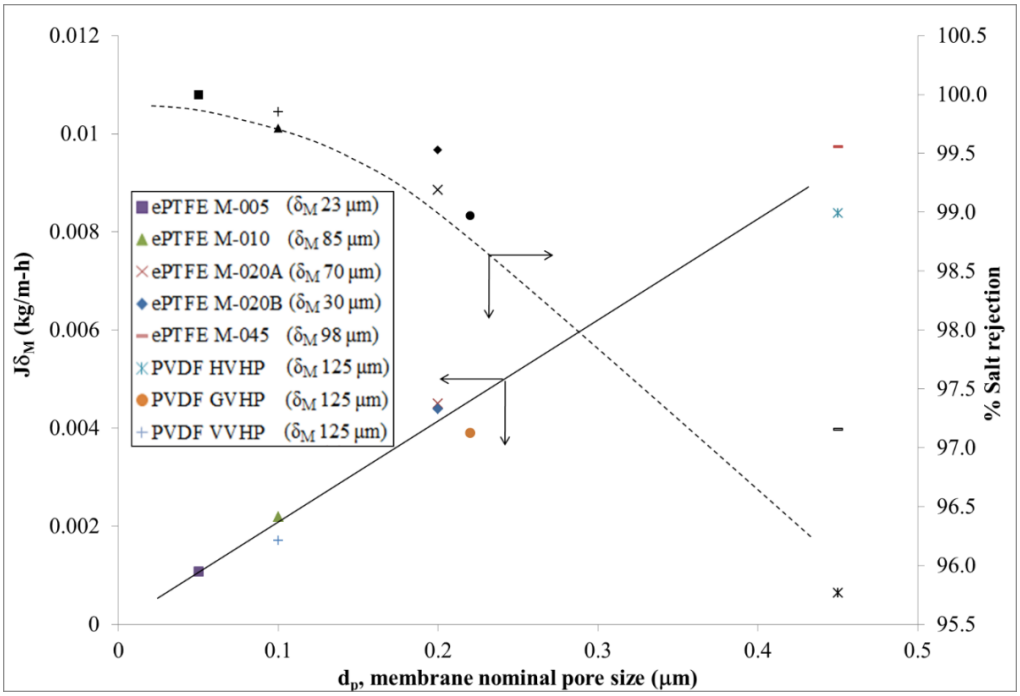

Figure 3.6 Experimental VMD values of $J\delta_M$ and salt rejection vs. membrane nominal pore sizes for all membranes.

3.4.3 Further Investigation of Salt Leakage

Pressure fluctuations near brine entrance of the CPVC cell recorded during a 30 second period for ePTFE M-045 membrane are shown in Figure 3.7. The applied vacuum pressure was 7.6 kPa (1.1 psi). The average pressure on the feed brine side was maintained at 29 kPag (4.21 psig) during the 3-hour experimental period.

The total pressure difference imposed on the membrane was 4.21 + 14.7 - 1.1psi = 17.81 psi = 122.8 kPa. The experimental LEP values were 125.48 ± 17.85 kPa (18.20±2.59 psi) (Table 3.2) which is close to the applied pressure difference during VMD. The maximum pore size, 1.48 μm, calculated for this membrane is based on the bubble point pressure, $P_{BP,}$ from manufacturer's data. The salt leakage is due to membrane wetting because of the large value of the maximum pore size.

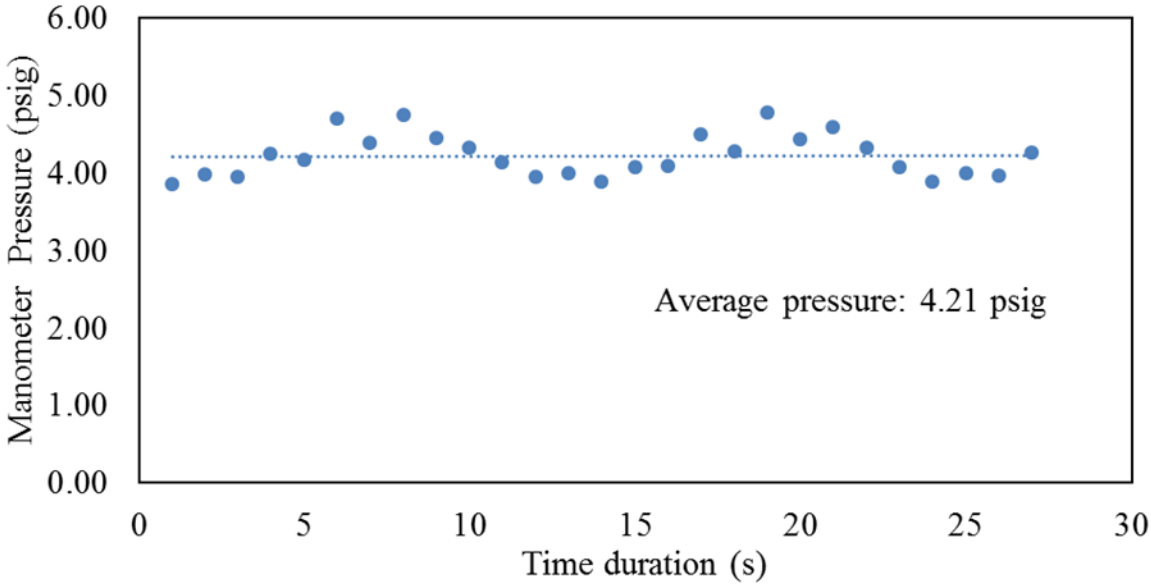

Figure 3.7 Experimental values of manometer pressure near the brine inlet for ePTFE M-045.

Table 3.2 Liquid Entry Pressure (LEP) Experimental Results

Membrane	d_p (μm)	LEP (psi)	LEP (kPa)
* ePTFE M005	0.05	>200.00	>1378.95
*ePTFE M010	0.1	111.60±1.52	769.46±10.46
*ePTFE M020A	0.2	29.00±4.00	199.95±27.58
*ePTFE M020B	0.2	24.80±1.92	170.99±13.26
* ePTFEM045	0.45	18.20±2.59	125.48±17.85
**PVDF VVHP	0.1	48.40±0.55	333.71±3.78***
** PVDF GVHP	0.22	34.80±1.10	239.94±7.55***
** PVDF HVHP	0.45	21.60±0.55	148.93±3.78

* W.L.Gore & Associates. Inc, Elkton, MD

** EMD Millipore Corp., Billerica, MA

*** Experimental results are close to literature data [24]

3.4.4 Model Simulation Results of Water Vapor Flux

Comparisons of the model predicted values for water vapor flux using the dusty-gas model (DGM) (Equations (3.13-3.14)) and Knudsen diffusion model (Equations (3.9-3.12)) for ePTFE M-045 (d_M 0.45, δ_M 98 μm, ε_M 0.8) at brine inlet temperatures of 65-85℃ and various brine flow rates are shown in Figure 3.8. Vacuum level used was 92.5% of full vacuum (7600 Pa). The dynamic viscosity of water vapor used for all temperatures, μ, was 0.653×10^{-3} Pa·s. Knudsen diffusion is the dominant regime in VMD transport since the K_n values for all membranes were larger than 1 at all temperatures (Table 3.1). The deviation between the two models is within 1.3 %.

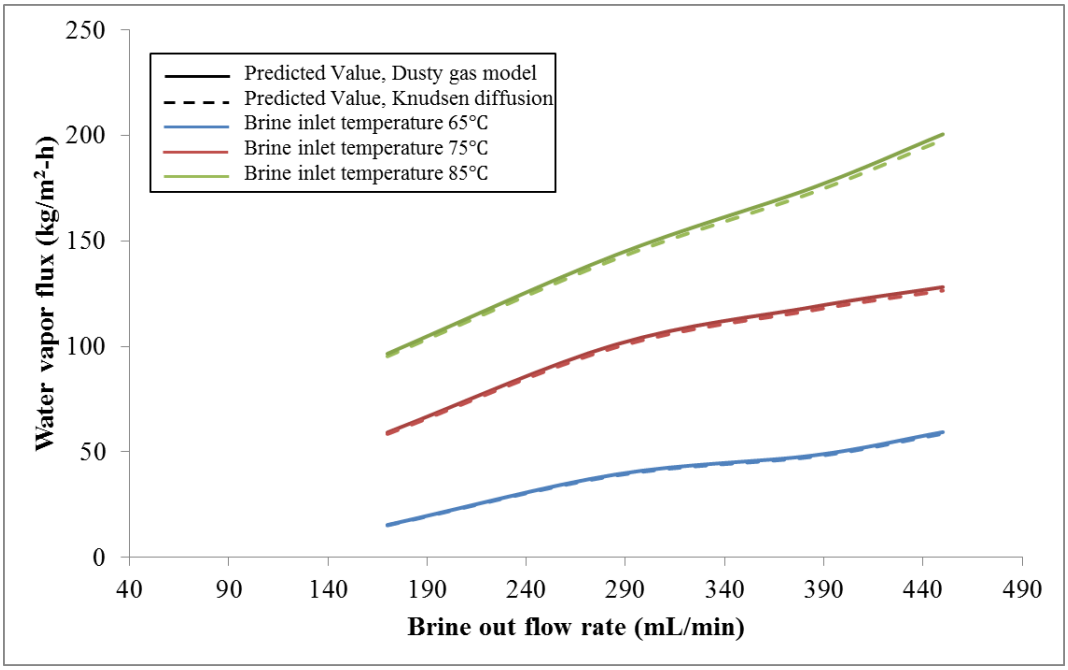

Figure 3.8 Comparison of predicted values for water vapor flux using dusty-gas model and Knudsen diffusion for ePTFE M-045 membrane.

Figure 3.9 compares the experimental and predicted values of water vapor flux using DGM for all membranes studied at a brine inlet temperature 65℃ and various brine flow rates. Vacuum level applied here was 92.5% of full vacuum (7600 Pa). Comparing ePTFE membranes M-020B and M-020A having the same nominal pore size and different thicknesses, M-020B (d_M 0.2, δ_M 30 μm, ε_M 0.8) shows much higher flux (86.2 kg/m^2-h) because it is much thinner than M-020A (d_M 0.2, δ_M 70 μm, ε_M 0.8). Comparing PVDF membranes HVHP (d_M 0.45, δ_M 125 μm, ε_M 0.75), GVHP (d_M 0.22, δ_M 125 μm, ε_M 0.75) and VVHP (d_M 0.1, δ_M 125 μm, ε_M 0.7) having the same thickness and different pore sizes, the water vapor flux increased with increasing membrane pore

size. It appears that the predicted flux values are in reasonable agreement with the measured values with deviation less than 5% for all membranes.

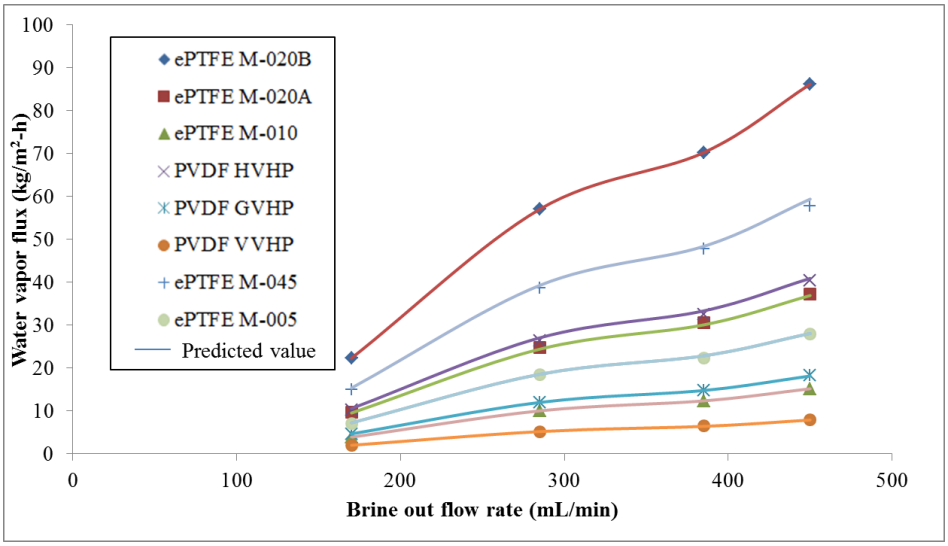

Figure 3.9 Experimental and predicted values of water vapor flux using DGM for all membranes at 65 ℃.

Figure 3.10 illustrates the experimental and predicted values of membrane mass transfer coefficient (k_m) using DGM for all membranes at brine inlet temperatures of 65-85℃ and various brine flow rates. Vacuum level used was 92.5% of full vacuum (7600 Pa). Different k_m values were achieved at different brine inlet temperatures. The values of tortuosity for all the membranes were assumed to be $1/\varepsilon_M$. The predicted values of k_m are comparable to the experimentally obtained values from measured water vapor fluxes. The deviation was within 5%.

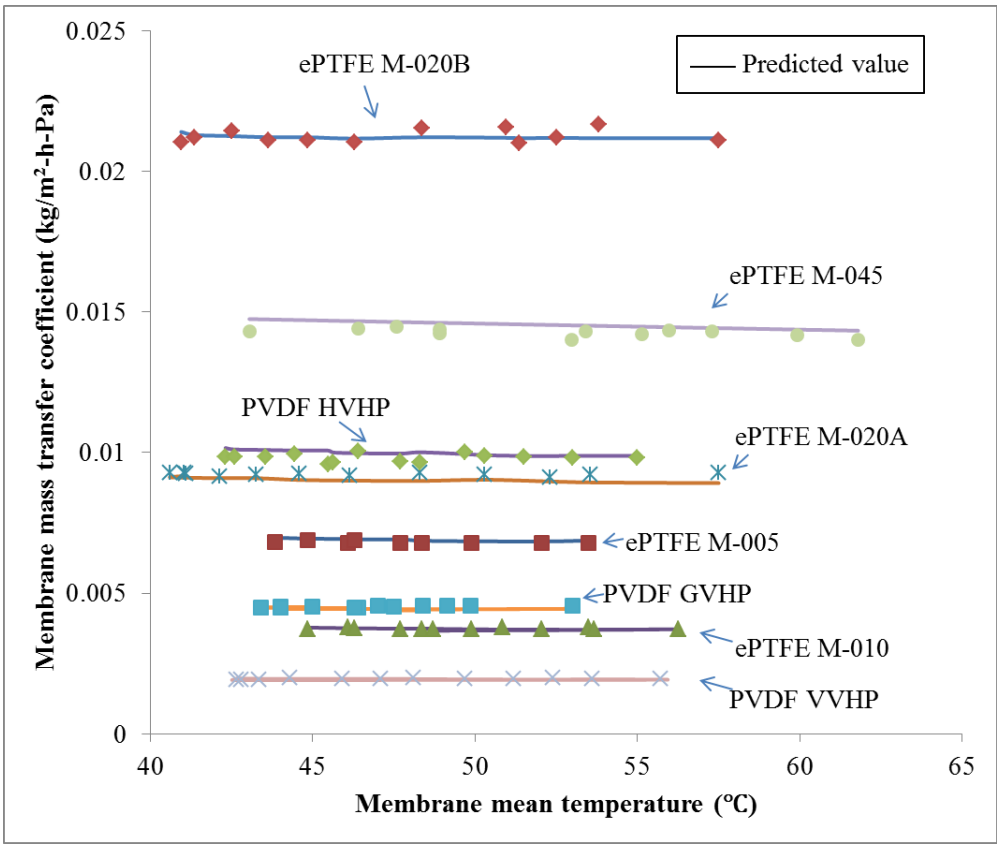

Figure 3.10 Membrane mass transfer coefficient prediction using DGM for all membranes.

The influence of various vacuum levels on water vapor fluxes was also predicted using DGM for membrane ePTFE M-045. The results are shown in Figure 3.5. Brine inlet temperature was 75℃. Brine flow rate was 280 mL/min. Four vacuum levels, 88.2%, 90.0%, 92.5%, 95.2% of full vacuum were applied. The deviation between predicted values and experimental values of water vapor flux is within 5%.

To investigate the effect of membrane thickness on water vapor flux in VMD, simulations were done for water vapor flux for brine side heat transfer coefficient h_f ranging between 200 to 1200 W/m^2-K for various membrane thicknesses (Figure 3.11).

Membrane thickness less than 5 μm was not employed since orifice flow mechanism needs to be considered as the thickness is drastically reduced. Parameters used in simulation are shown in the figure legend. Water vapor flux increased with a decrease in membrane thickness from 200 μm to 5 μm for h_f values above 200 W/m^2-K. For a thin membrane at higher h_f s, although very high values of water vapor flux can be reached (> 200 kg/m^2-h), the risk of membrane pore wetting also increases drastically due to a possible increase in feed side pressure often present at a higher h_f.

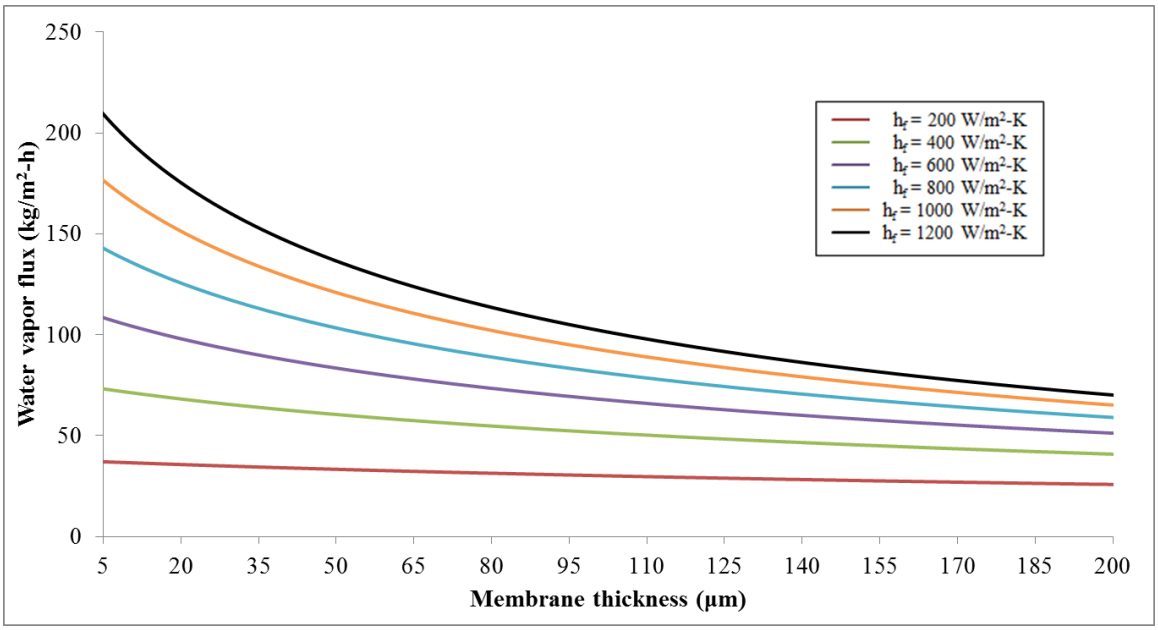

Figure 3.11 Simulation results of water vapor flux for a h_f range of from 200 - 1200 W/m^2-K for various membrane thicknesses. Simulation parameters: d_M, 0.45 μm; ε_M, 0.8; χ_M, 1.25; brine mean temperature, 65℃.

3.4.5 LEP Data vs. Membrane Nominal Pore Size (d_p) and the Maximum Pore Size (d_{max})

Figures 3.12A and 3.12B show the relation between the liquid entry pressure and the membrane nominal pore size and the maximum pore size. The maximum pore size information for PVDF membranes was experimentally obtained in Chapter 2. For ePTFE membranes, the maximum pore size information was obtained from manufacturer. It is notable that LEP is defined as the pressure applied to the system while continuous flux is produced instead of the first drops of liquid breaking through the membrane [47]. Further investigations are needed.

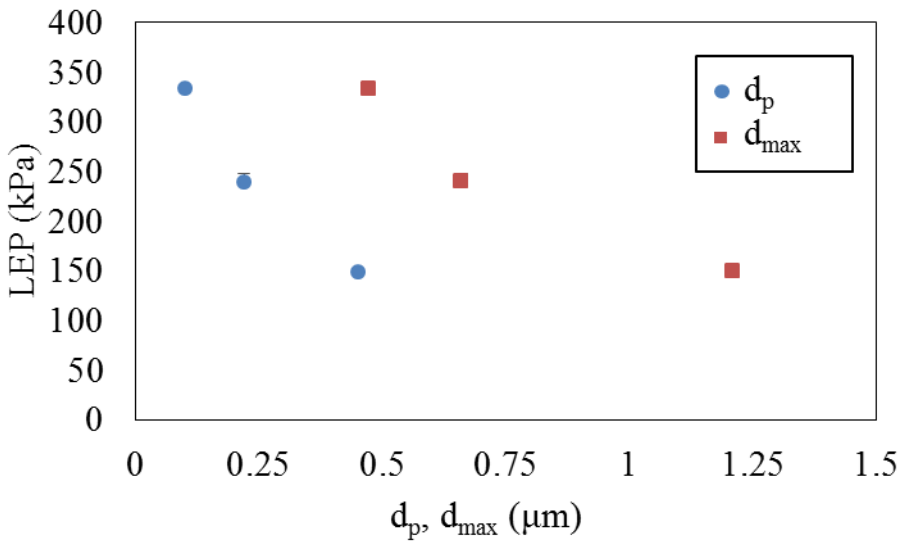

Figure 3.12A Experimental values of LEP for PVDF membranes having nominal pore size (d_p) ranging between from 0.1 and 0.45 µm and associated maximum pore size.

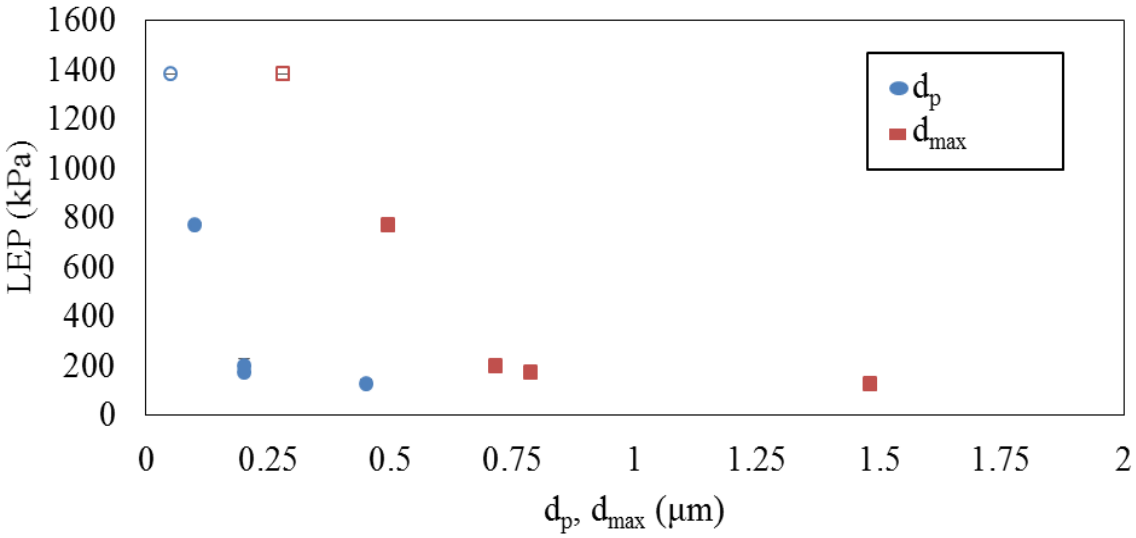

Figure 3.12B Experimental LEP results for ePTFE membranes having nominal pore size range from 0.05 to 0.45 μm and associated maximum pore size. The hollow dot symbol represents LEP larger than 1379 kPa (200 psi) for ePTFE M-005.

3.5 Concluding Remarks

Vacuum membrane distillation is a promising technology for desalination. Various studies have proved the feasibility of VMD in removal of trace gases and VOCs from water, and removal of water in desalination. A clearer understanding of the mass transfer mechanisms, the role of various membrane properties is expected to facilitate the development of VMD. Practical development and performance estimation in industrial scale are also needed in future.

In VMD, the values of the mean of the vapor pressure of water vapor on two sides of the membrane are much lower than those in DCMD resulting in larger mean free path, which leads to values of K_n much larger than 1. As a result, Knudsen diffusion is dominant in VMD mass transfer for all membranes at feed brine temperatures ~65 - 85℃

used in this study. At the same vacuum level, water vapor flux increases almost linearly with membrane pore size. Water vapor flux decreases linearly with increasing membrane thickness. Water vapor flux increases linearly with vacuum levels. To achieve sufficient water vapor flux, low pressure (high vacuum level) should be applied to generate high water vapor partial pressure difference on two sides of the membrane. At the same vacuum level, salt leakage is observed mostly at higher temperatures and higher brine flow rates due to wetting of membrane pores; 100% salt rejection is achieved for low brine flow rates at all temperatures. The measured LEP value for one of the largest pore size membrane, ePTFE M-045, was close to the applied pressure difference at higher flow rates explaining the basis for salt leakage.

In the present study, Wilson plot based technique used earlier in Chapter 2 to determine the heat transfer coefficient on the brine side of the flat membrane in the same cell used for DCMD was used to determine unknown heat transfer conditions in VMD. This allowed experimental determination of the membrane-liquid interface temperatures and thereby the membrane mass transfer coefficients k_m for water vapor. Knudsen diffusion model and dusty-gas model were utilized to predict the membrane mass transfer coefficient for a variety of ePTFE and PVDF membranes. The predicted values were quite close to the values of k_m determined via Wilson plot technique from the experimental data.

CHAPTER 4

PERFORMANCE ESTIMATES FOR LARGE HOLLOW FIBER-BASED DCMD DEVICES

4.1 Introduction

Membrane distillation (MD) is a thermally-driven separation process, in which only vapor molecules can pass through a porous hydrophobic membrane. The partial pressure difference of vapor between the two sides of the membrane is the driving force for mass transfer. Fouling refers to the deposition of some feed components on the membrane surface or within the membrane pores [49]. It increases cost due to increased energy consumption, downtime, cleaning, necessary membrane area and construction, labor, time, and material costs for backwashing and cleaning processes [50]. Unlike other pressure driven membrane separation processes such as reverse osmosis (RO), MD can be utilized in desalting highly saline waters that have considerable osmotic pressures and is more fouling resistant [42]. However, a fouling layer formed on the membrane surface can cause progressive wetting of the membrane in MD. This phenomenon is accelerated if salt crystals are formed on pore mouths [51-53]. Scale can build up on the membrane surface if the concentration of minerals or salt becomes too high [1].

Various investigators have studied different types of fouling in MD such as inorganic salt scaling or precipitation fouling, particulate fouling, biological fouling, and chemical membrane degradation [54-57]. Fouling can be controlled by selecting appropriate membrane material, flow manipulation, additional force field and cleaning

procedure [51]. Extensive studies on the effects of various flow manipulations, namely to increase mass transfer rates and prevent membrane fouling have been studied since 1980s. Figure 4.1 shows typical types of flow manipulations, namely, Taylor vortices created by rotating cylindrical membranes, oscillating / rotating disc, air bubbling and Dean vortices. Pulsatile blood flow was proposed in 1973 to enhance gas transfer in membrane blood oxygenators [60]. It was then applied to a few protein separations for MF and UF [61-64]. The mechanism of the Pulsatile flow induced oscillation on fouling is unknown.

A previous study by He et al. [66] showed that in a mixed $CaSO_4$-$CaCO_3$ system, at high saturation indices and fast precipitation rate, no significant loss in water vapor permeation was observed even at elevated temperatures or high concentrations. It was due to the application of cross flow, multiple flow separation points, eddies around hollow fiber membranes etc., and the nature of the hydrophobic coating on the surface.

Song et al. (2008) [25] have shown that a particular membrane configuration with a specific membrane and a novel method of operation ensures no precipitation based fouling from $CaCO_3$ and $CaSO_4$ in direct contact membrane distillation (DCMD). They employed crossflow of hot brine across unrestrained hydrophobic hollow fibers in DCMD. Further the hollow fiber ODs had a highly porous plasma polymerized fluorosilicone coating which effectively had larger pores than the pores of the substrate polypropylene hollow fibers. They had taken a video of the oscillations of hollow fibers

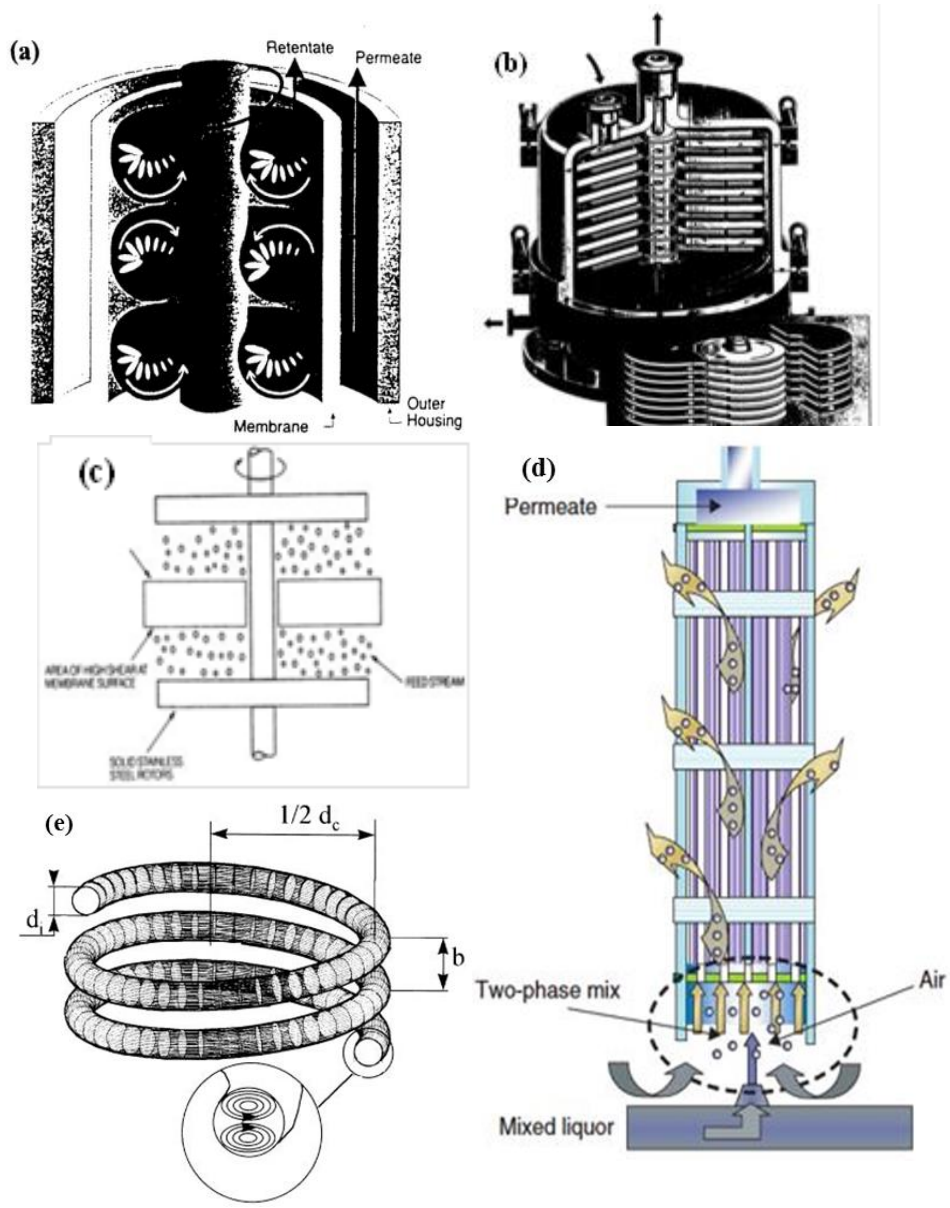

Figure 4.1 (a) Taylor vortex module (by courtesy of Membrex) [63]; (b)&(c) A rotary membrane unit (by courtesy of Pall corporation); (d) The MemJet module with integral jet aerator; (e) Dean vortices in a coiled pipe.

Source: [63,64,65].

in the pilot plant study [29]. This technique does not involve any of the special investments shown in Figure 4.1. In Figure 4.2, a few snapshots of the hollow fiber oscillation are shown.

Earlier DCMD simulation models [25,29] assumed membrane mass transfer coefficient, k_m, as an adjustable parameter for modeling water vapor transport in large hollow fiber modules with crossflow in a given range, guided by estimated values and Zukauskas equation for predicting the heat transfer coefficients in the shell-side boundary layer. A model was proposed to predict the membrane mass transfer coefficient in DCMD in Chapter 2. This model has now been introduced into the earlier model by Song et al. (2008) [29] of the crossflow hollow fiber modules.

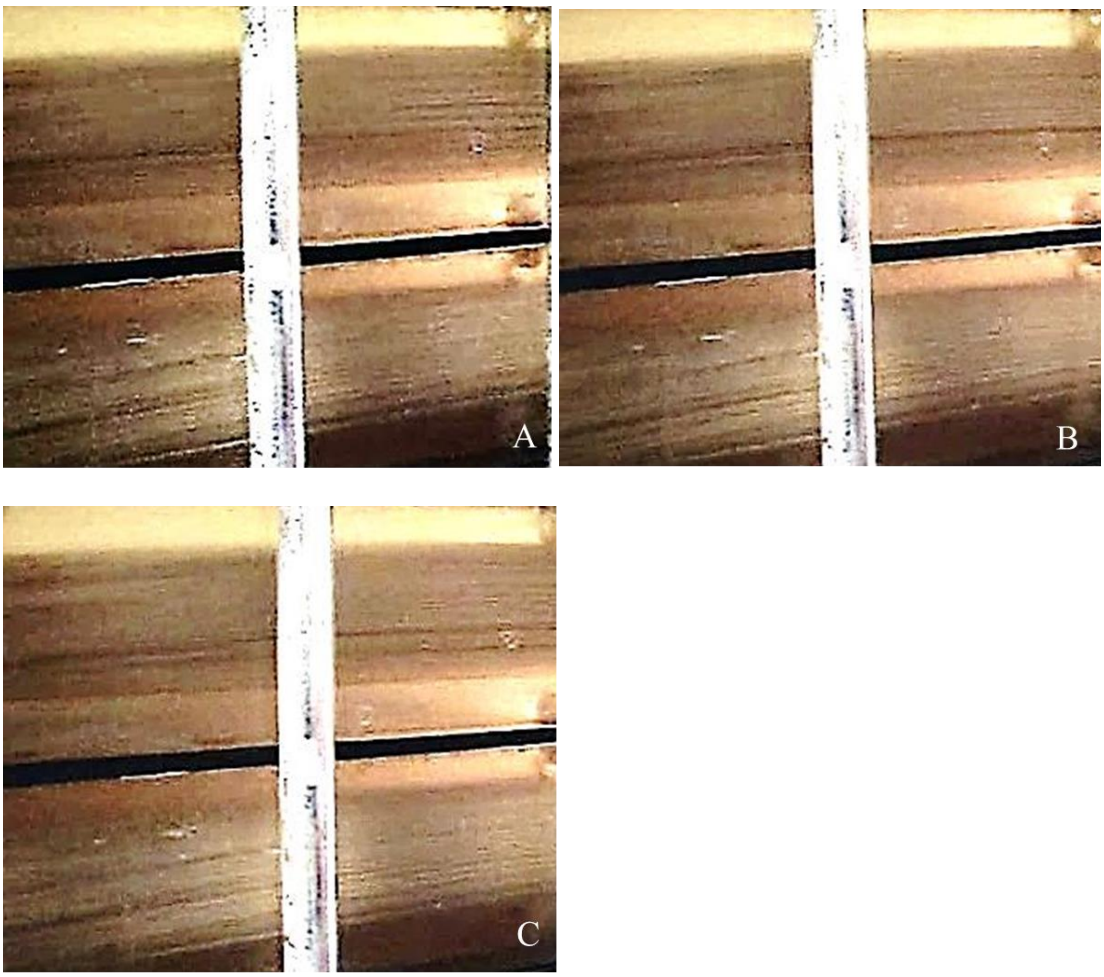

Figure 4.2 Snapshots of hollow fiber oscillation. Time interval 0.047s.

4.2 Membrane Material, Modules and System

Table 4.1 shows two sets of membranes and membrane module properties used for simulation. On the basis of previously used PP hollow fiber modules [25, 29], another PVDF hollow fiber-based module was considered for simulation because of the increased fiber ID and potentially reduced tube side pressure drop. The number of total fibers for this PVDF hollow fiber module was reduced in order to keep membrane area the same as in the PP hollow fiber module. The number of fibers per layer has been modified to keep similar shell side cross-sectional area and similar packing density (shell side cross-sectional area over total cross-sectional area based on module frame) for two modules.

The city water TDS used previously was 34 ppm = 0.34 mMol/L [29]. The conductivity of the city water was 55 μS/cm (in the range of drinking water 5-50 mS/m). The effect of concentration polarization is minimal.

The model developed here is based on the previous model [25]; details of the original model will not be discussed. Hot brine flows perpendicularly to the hollow fibers with a flow rate V_{b0} and temperature T_{b0} from the 1st fiber layer to the mth fiber layer; then the stream exits the module with a flow rate V_{b1} and temperature T_{b1}. For a typical jth fiber layer (j=1,2,3…m), cold distillate is introduced to the bores of the hollow fibers at x=0, with flow rate $V_{p0,j}$ and temperature $T_{p0,j}$ and exits at x=L, with a flow rate $V_{p1,j}$ and temperature $T_{p1,j}$. (Figures 4.3&4.4). A schematic drawing considering a small length Δx at jth fiber layer is shown in Figure 4.5.

Table 4.1 Membrane and Module Properties

Membrane material	Support membrane PP with silicone fluoropolymer coating [29]*	PVDF**
Fiber ID (μm)	330	691
Wall thickness (μm)	150	117
Membrane pore size (μm)	0.6 (maximum pore size)	0.2
Membrane porosity	0.8	0.54
Effective fiber length (cm)	24.1	
Effective membrane surface area (cm^2)	6622.7	6667.1
No. of fibers	2652	1275
No. of fibers per layer	102	75
No. of fiber layers	26	17
Effective cross-sectional area for shell-side liquid flow (cm^2)	59.7	
Arrangement of fibers	Staggered	
Packing density	0.209	0.216
Shell side flow mode	Cross flow	
Rectangular module frame (internal dimensions)	L_f: 25.4 cm, W_f: 8.9 cm, H_f: 4.45cm	

* Membrana, Charlotte, NC; Plasma polymerized coating on support hollow fibers were applied by Applied Membrane Applied Membrane Technology, Inc., Minnetonka, MN. Listed values are slightly different from [29].

** Arkema, King of Prussia, PA

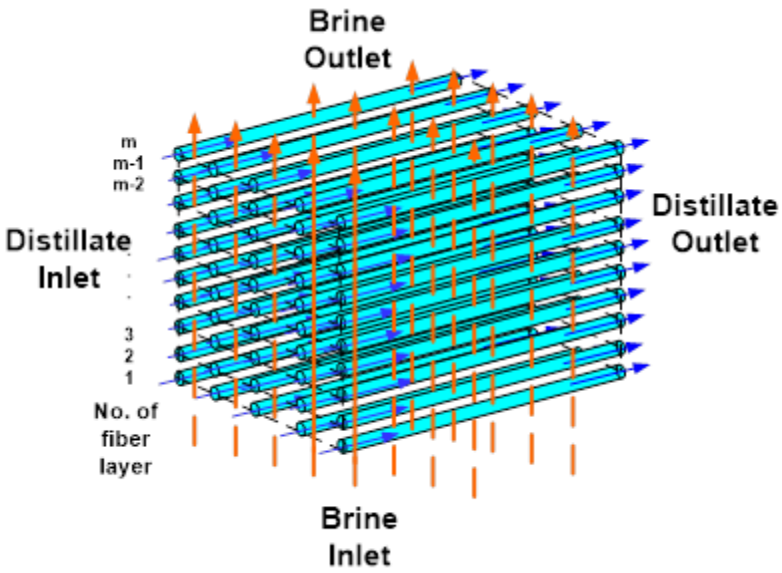

Figure 4.3 Arrangement of fibers. Figure adapted from Song et al., 2008 [29].

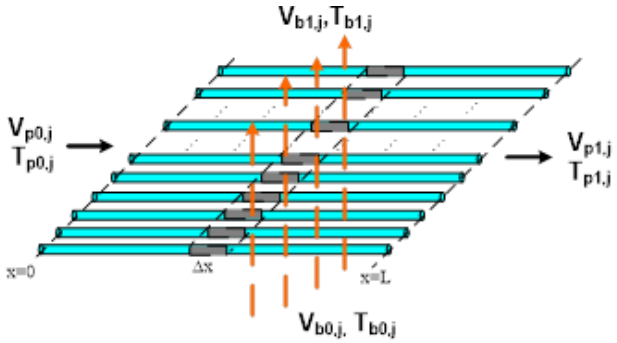

Figure 4.4 jth fiber layer. Figure adapted from Song et al., 2008 [29].

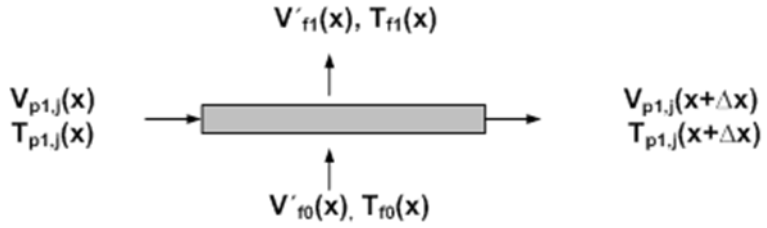

Figure 4.5 Mass and energy balance for the length of Δx in the distillate flow direction. Figure adapted from Song et al., 2008 [29].

4.3 Main Modeling Equations

4.3.1 Shell-Side Hot Brine: Heat Transfer

$$\left.\frac{dQ(x)}{dx}\right|_j = h_f A_{rf} \left(n\pi d_i\right)(T_{f\,0,j}(x) - T_{fm,j}(x)) \tag{4.1}$$

$$A_{rf} = (\frac{d_o}{d_i}) \tag{4.2}$$

4.3.2 Tube-Side Distillate: Heat Transfer

$$\left.\frac{dQ(x)}{dx}\right|_j = h_p A_{rp} \left(n\pi d_i\right)(T_{pm,j}(x) - T_{p1,j}(x)) \tag{4.3}$$

$$A_{rp} = \frac{d_i}{d_i} (=1) \tag{4.4}$$

4.3.3 Shell Side Heat Transfer, Zukauskas Equation:

$$Nu_f = \frac{h_f d_o}{k_o} = 1.04 Re_o^{0.4} Pr_o^{0.36} \left(\frac{Pr_o}{Pr_w}\right)^{0.25} F_c \ (Re < 40) \tag{4.5}$$

$$Nu_f = \frac{h_f d_o}{k_o} = 0.71 Re_o^{0.5} Pr_o^{0.36} \left(\frac{Pr_o}{Pr_w}\right)^{0.25} F_c \ (Re > 40) \tag{4.6}$$

where

$$Re_o = \frac{d_o \nu_o \rho_o}{\mu_o}; Pr_o = \frac{C_{po}\mu_o}{k_o}; Pr_w = \frac{C_{pw}\mu_w}{k_w}$$

$$F_c = 1 \tag{4.7}$$

4.3.4 Tube Side Heat Transfer, Sieder-Tate Equation:

$$Nu_p = \frac{h_p d_i}{k_i} = 1.86\left(\frac{d_i}{L}\right)^{0.25}\left(Re_i Pr_i\right)^{0.33}\left(\frac{\mu_i}{\mu_{wi}}\right)^{0.14} \tag{4.8}$$

where

$$Re_i = \frac{d_i v_i \rho_i}{\mu_i}; Pr_i = \frac{C_{pi}\mu_i}{k_i} \tag{4.9}$$

4.3.5 Heat Transfer across the Porous Membrane in the *j*th Fiber Layer

$$\left.\frac{dQ(x)}{dx}\right|_j = h_m A_{r\ln}\alpha(T_{fm,j}(x) - T_{pm,j}(x)) + N_{v,j}(x)\alpha(\Delta H_v(T_{pm,j}(x)) + C_{pm,j}T_{pm,j}(x)) \tag{4.10}$$

where

$$A_{r\ln} = \frac{d_{lm}}{d_i} \tag{4.11}$$

$$d_{lm} = \frac{d_o - d_i}{\ln\frac{d_o}{d_i}} \tag{4.12}$$

4.3.6 Heat Transferred by the Hot Brine in the *i*th Fiber Layer

$$\left.\frac{dQ(x)}{dx}\right|_j = \rho_{f0,j}(x)V'_{f0,j}(x)C_{pf0,j}(x)T_{f0,j}(x) - \rho_{f1,j}(x)V'_{f1,j}(x)C_{pf1,j}(x)T_{f1,j}(x)) \tag{4.13}$$

4.3.7 Local Water Vapor Flux in the *j*th Fiber Layer

$$N_{v,j}(x) = k_m A_{r\ln}(P_{fm,j}(x) - P_{pm,j}(x)) \tag{4.14}$$

$$N_{v,j}(x) = \frac{\left(\varepsilon_M / \chi_M\right)P_T D_{w-a}}{d_{lm}RT_m} \times \ln\left(\frac{D_{K_n}\left(P_T - P_{pm,j}(x)\right) + \left(\varepsilon_M / \chi_M\right)P_T D_{w-a}}{D_{K_n}\left(P_T - P_{fm,j}(x)\right) + \left(\varepsilon_M / \chi_M\right)P_T D_{w-a}}\right) \text{ [27]} \tag{4.15}$$

See Chapter 2, Equation (2.6) ~ Equation (2.9).

4.3.8 Tube Side Pressure Drop

$$\Delta P = \frac{32 \mu L v_i}{d_i^2} \tag{4.16}$$

4.4. Results and Discussion

4.4.1 Comparison of Current Model with Previous Model [29]

Figure 4.6 compares the simulation results of water vapor flux of one module from the current model with that of the model from Song et al., 2008 (Figure 6 in [29]). Dashed line represents the results from the original model, which was based on an assumed membrane mass transfer coefficient for the whole fiber bundle. The solid line represents the current model which is based on the analysis of fiber surface temperature along fiber length on each layer, under conditions same as those in Song et al.'s model. The maximum standard deviation between experimental values and Song's modeled values is 1.6. Current modeling results are much closer to the experimental values, especially at higher shell side flow rate. The maximum standard deviation between experimental and modeling values of this study is 0.8.

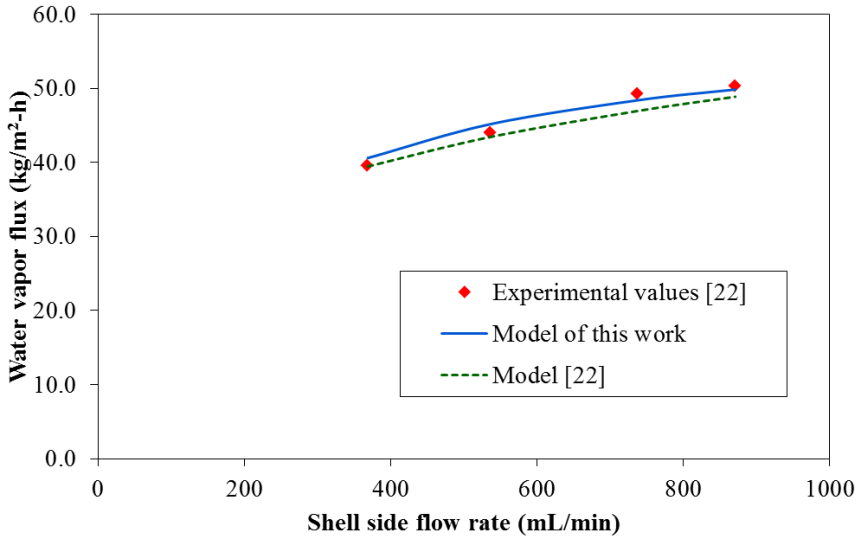

Figure 4.6 Comparison of two models for variation of water vapor flux with shell side flow rate of city water. Modeling parameters: d_i, 330 μm; d_o, 630 μm; N, 2652; V_{b0}, 22 L/min; V_{d0}, 10 L/min; $T_{b0,}$ 90 ℃; $T_{d0,}$ 20 ℃.

4.4.2 Simulation of Temperatures of the Fiber Inside and Outside Walls

Fiber inside wall temperatures (Figure 4.7) and outside wall temperatures (Figure 4.8) along the fiber length (0.241 cm to 24.1 cm) in various fiber layers were simulated. Figure 4.7A shows the fiber inside wall temperatures along fiber length in selected fiber layers. Fiber inside wall temperature increased with increasing fiber length as the amount of water vapor recovered is increased. The 1st fiber layer was heated up drastically since it was the closest layer to the incoming hot brine (90℃), while the 26th fiber layer was the farthest layer to the incoming hot brine. An overall distillate temperature (fiber inside wall temperature) profile is shown in Figure 4.7B. The temperatures at the distillate inlet (fiber length 0.241 cm) increased from 30℃ to 40℃ as the fiber layer was getting closer to the incoming hot brine from the 26th layer to the 1st layer of fibers, while it increased

from 62℃ to 75℃ for those at the distillate outlet (fiber length 24.1 cm). Figure 4.8A shows the fiber outside wall temperature along fiber length in selected fiber layers. The fiber outside wall temperature increased slightly with increasing fiber length, 3℃ for the 1st fiber layer and 6℃ for the 26th fiber layer. An overall shell side profile is shown in Figure 4.8B. What is notable is that the shell side brine temperature drops drastically at distillate inlet from 85 ℃ to 64℃ from the 1st fiber layer to the 26th fiber layer, while the brine temperature drops from 88℃ to 70℃ at distillate outlet from the 1st fiber layer to 26th fiber layer. This is due to the higher flux achieved at distillate inlet location due to the higher ΔT.

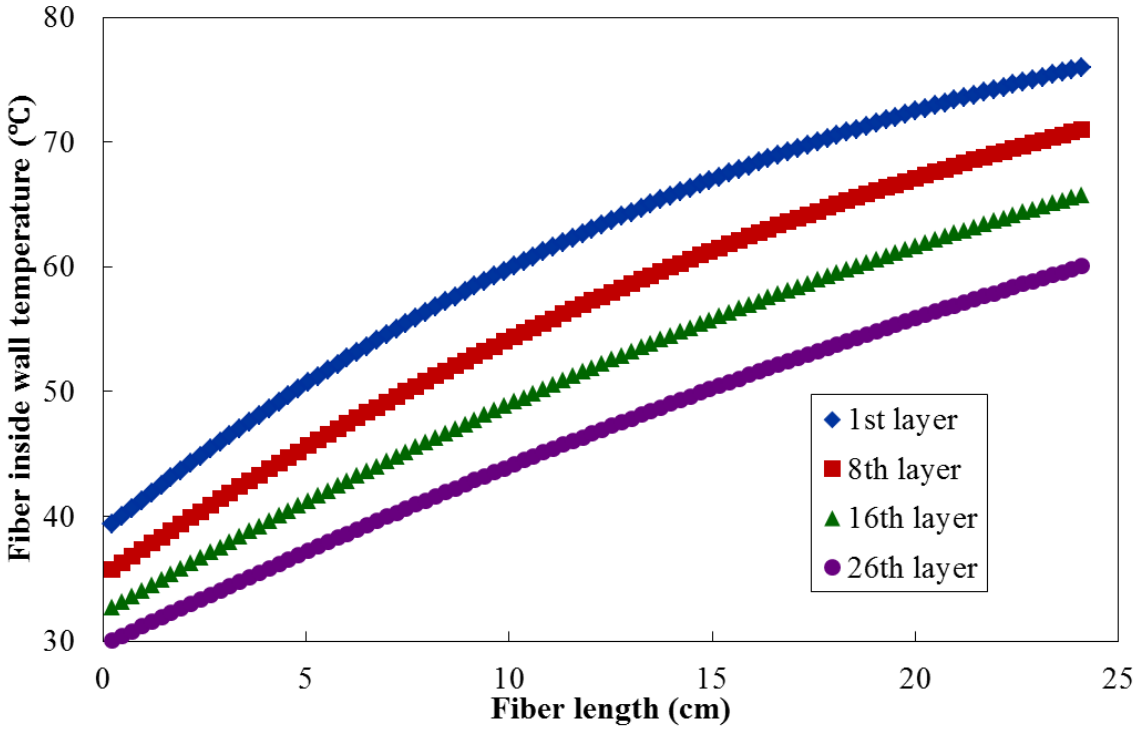

Figure 4.7A Predicted fiber inside wall temperatures along fiber length in selected fiber layers. Modeling parameters: d_i, 330 μm; d_o, 630 μm; N, 2652; L, 24.1cm; V_{b0}, 22 L/min; V_{d0}, 10 L/min; $T_{b0,}$ 90 ℃; $T_{d0,}$ 20 ℃.

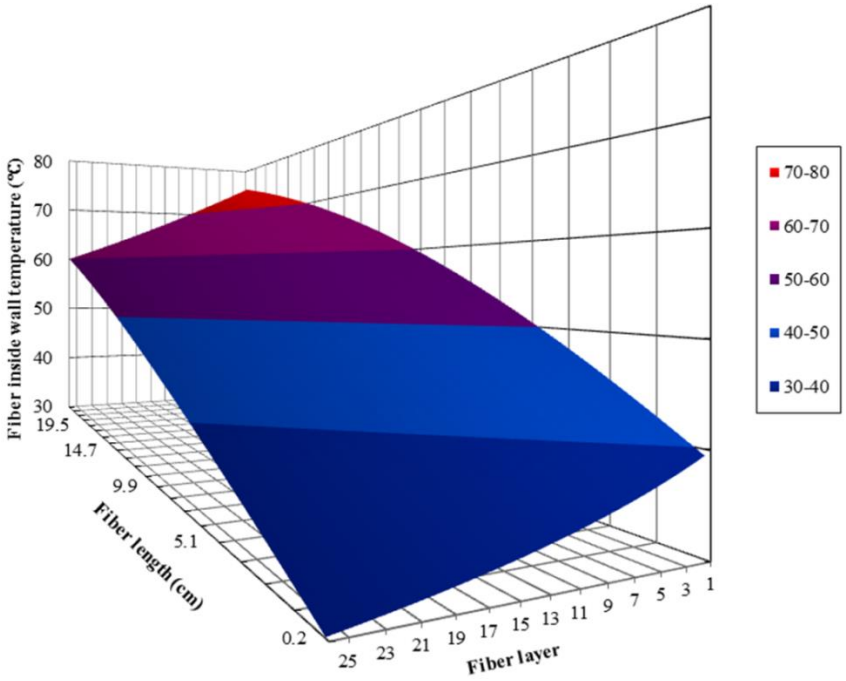

Figure 4.7B Predicted fiber inside wall temperatures along fiber length for all fiber layers. Modeling parameters: d_i, 330 μm; d_o, 630 μm; N, 2652; L, 24.1cm; V_{b0}, 22 L/min; V_{d0}, 10 L/min; $T_{b0,}$ 90 ℃; $T_{d0,}$ 20 ℃.

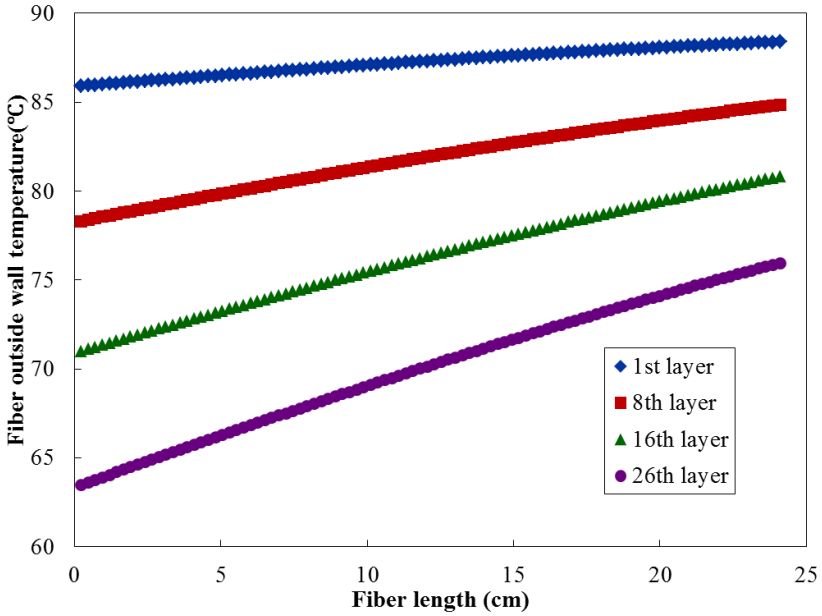

Figure 4.8A Predicted fiber outside wall temperatures along fiber length in selected fiber layers. Modeling parameters, d_i, 330 μm; d_o, 630 μm; N, 2652; L, 24.1cm; V_{b0}, 22 L/min; V_{d0}, 10 L/min; $T_{b0,}$ 90 ℃; $T_{d0,}$ 20 ℃.

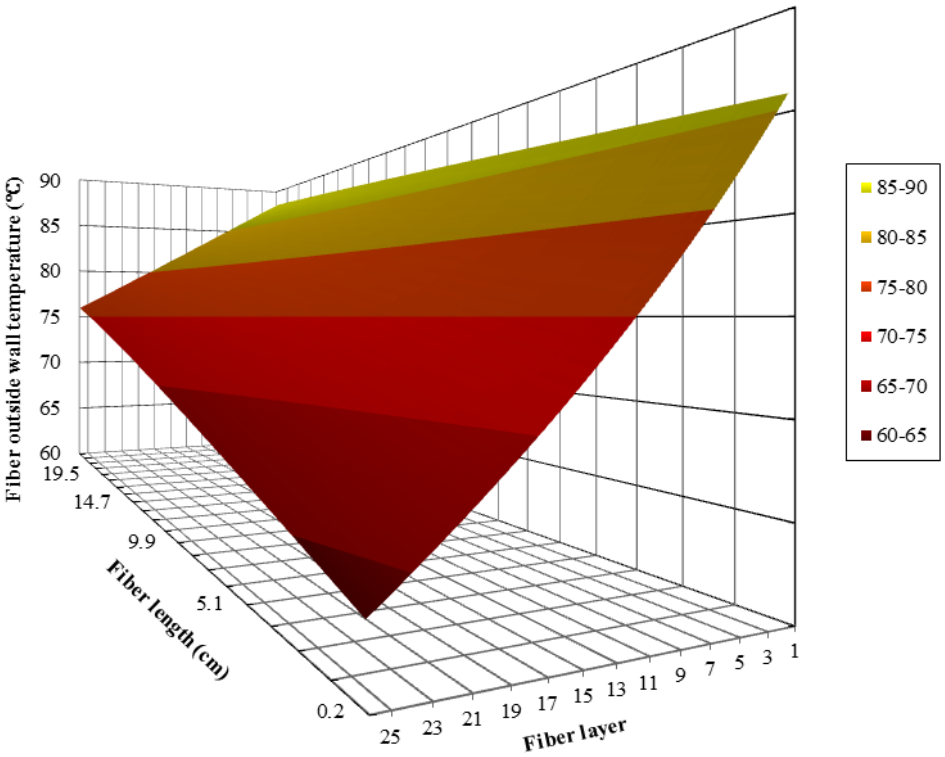

Figure 4.8B Predicted fiber outside wall temperatures along fiber length for all fiber layers. Modeling parameters, d_i, 330 μm; d_o, 630 μm; N, 2652; L, 24.1cm; V_{b0}, 22 L/min; V_{d0}, 10 L/min; $T_{b0,}$ 90 ℃; $T_{d0,}$ 20 ℃.

4.4.3 Simulation of Water Vapor Flux

Local water vapor flux profile for all fiber layers are shown in Figure 4.9. The 1st fiber layer generated the highest water vapor flux because of the largest temperature difference between fiber outside and inside wall temperatures, while the 26th layer has the lowest water vapor flux due to the lowest temperature differences (Figure 4.9A). The drop of water vapor fluxes along the fiber length was attributed to the effectively lower temperature difference between two sides of the fiber (Figure 4.9B). Figure 4.10 shows the water product rate for all fiber layers.

4.4.4 Simulation of Membrane Mass Transfer Coefficient

Figure 4.11 shows the predicted membrane mass transfer coefficient along the fiber length. It was based on local water vapor flux values over local temperature difference on two sides of the fiber along the fiber length. The overall predicted membrane mass transfer coefficient was around 0.0014 kg/m^2-h-Pa. Song et.al used a k_m value of 0.0015 kg/m^2-h-Pa [29].

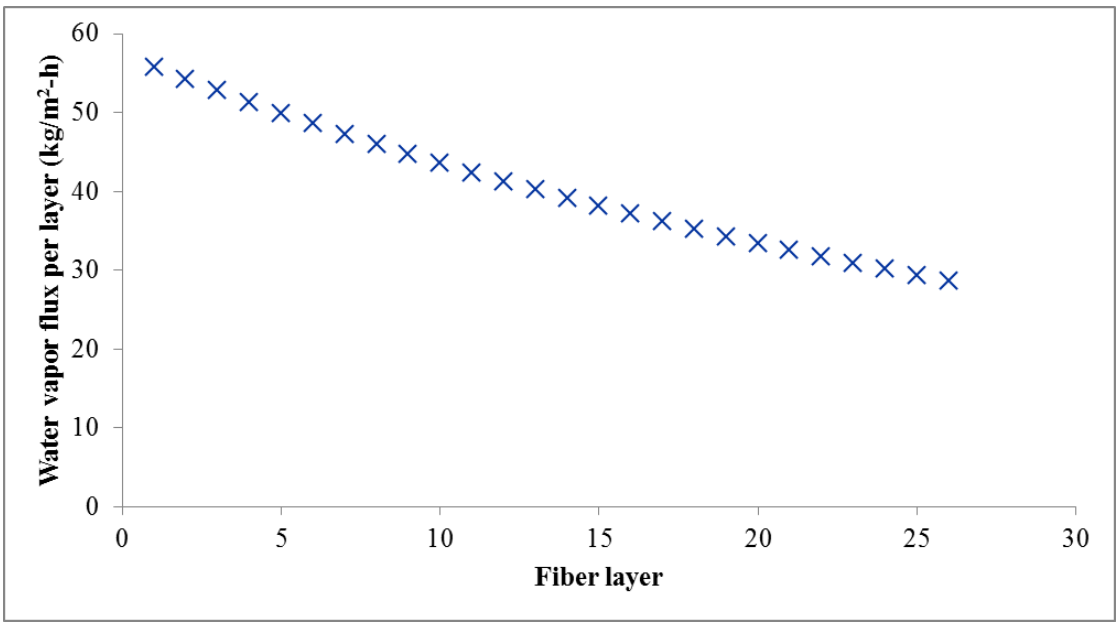

Figure 4.9A Predicted water vapor fluxes per fiber layer. Modeling parameters: d_i, 330 μm; d_o, 630 μm; N, 2652; L, 24.1cm; V_{b0}, 22 L/min; V_{d0}, 10 L/min; $T_{b0,}$ 90 ℃; $T_{d0,}$ 20 ℃.

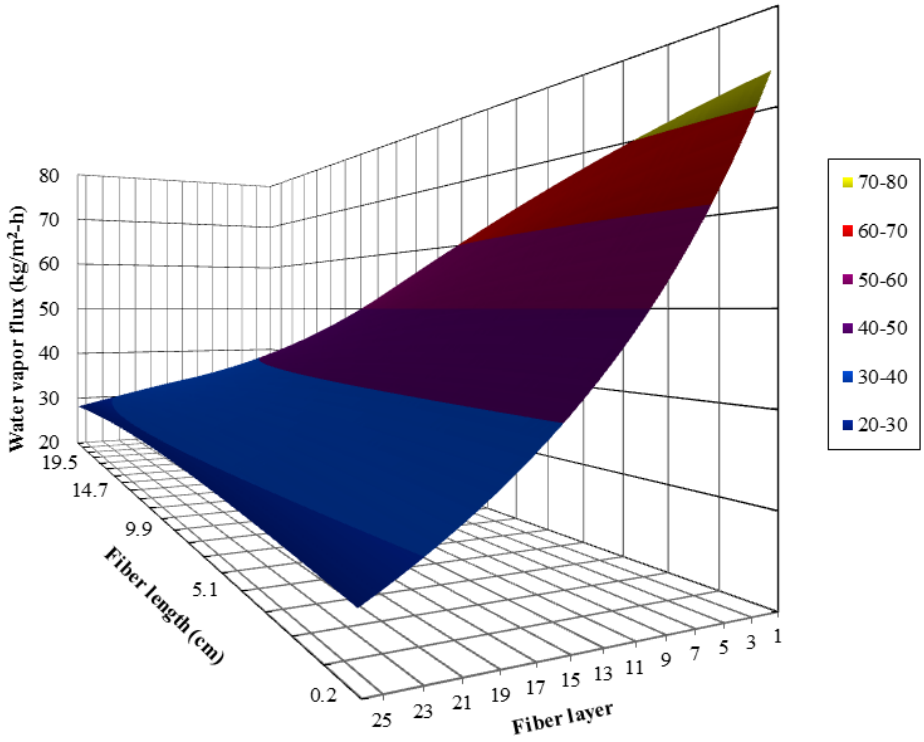

Figure 4.9B Predicted water vapor fluxes along fiber length for all fiber layers. Modeling parameters, d_i, 330 μm; d_o, 630 μm; N, 2652; L, 24.1cm; V_{b0}, 22 L/min; V_{d0}, 10 L/min; $T_{b0,}$ 90 ℃; $T_{d0,}$ 20 ℃.

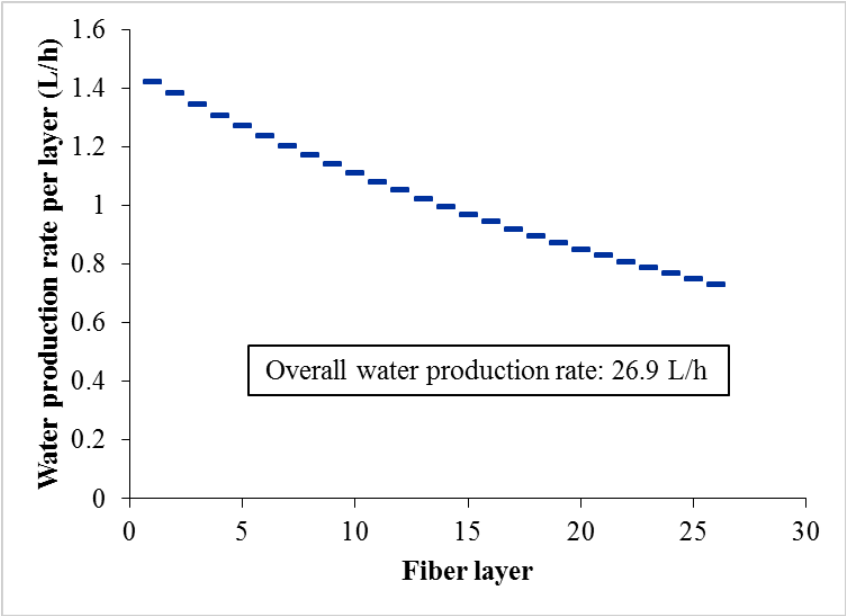

Figure 4.10 Predicted water production rate per fiber layer. Modeling parameters, d_i, 330 μm; d_o, 630 μm; N, 2652; L, 24.1cm; V_{b0}, 22 L/min; V_{d0}, 10 L/min; $T_{b0,}$ 90 ℃; $T_{d0,}$ 20 ℃.

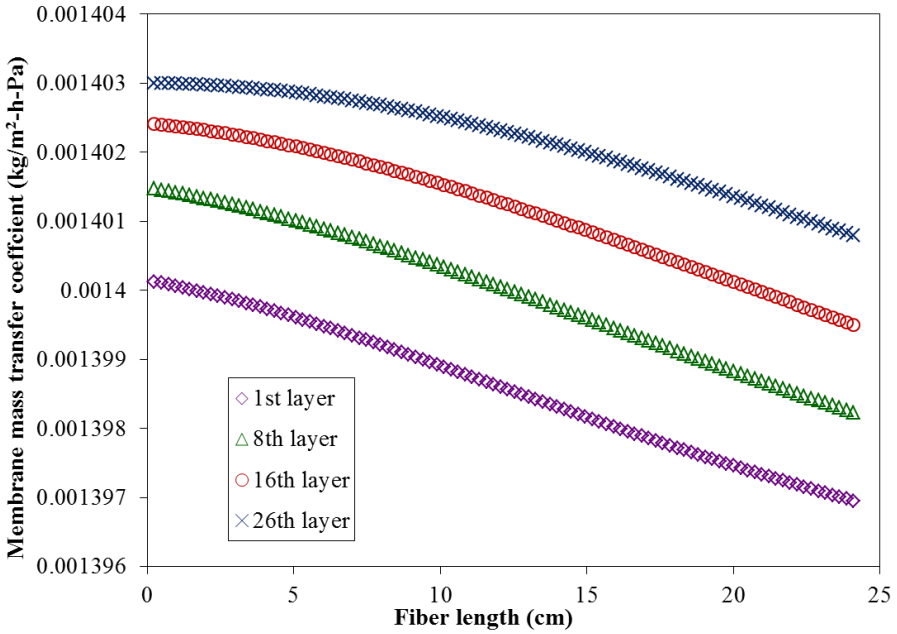

Figure 4.11 Predicted mass transfer coefficients along fiber length in selected fiber layers. Modeling parameters: d_i, 330 μm; d_o, 630 μm; N, 2652; L, 24.1cm; V_{b0}, 22 L/min; V_{d0}, 10 L/min; $T_{b0,}$ 90 ℃; $T_{d0,}$ 20 ℃.

4.4.5 Simulation of Water Vapor Flux and Tube Side Pressure vs. Fiber ID

Figure 4.12 illustrates the predicted water vapor flux and tube side pressure drop for fibers with d_i, 330 μm and d_o, 630 μm. Water vapor flux increased slightly with increasing tube side flow rate. The tube side pressure drop was 46.3kPa (6.72 psi) for a tube side flow rate of 10 L/min. It doubled to 92.7 kPa (13.4 psi) when the tube side flow rate was doubled to 20 L/min.

To reduce the pressure drop, modeling was conducted for fibers having a d_i, 691 μm and d_o, 925 μm. Figure 4.13 shows the predicted water vapor flux and tube side pressure drop. Comparing Figures 4.12 and 4.13, one finds that the values of tube side pressure drop were drastically decreased from 46.3 kPa to 5 kPa at V_{d0} = 10 L/min, while

it decreased further from 92.7 kPa to 10 kPa at V_{d0} = 20 L/min. On the other hand, water vapor flux is comparable to that from the fibers with d_i, 330 μm and d_o, 630 μm.

4.4.6 Simulation of Water Vapor Flux, Water Production Rate and Tube Side Pressure vs. Fiber Length

The effects of fiber length on the tube side pressure drop, water vapor flux and water production rate were simulated and are shown in Figures 4.14A, B and C. Comparing Figure 4.14A and Figure 4.13, the values of tube side pressure drop doubled as the fiber length increased from 24.1 cm to 48 cm; at T_{bo} = 90 ℃, the value of water vapor flux decreased from 38.9 kg/m^2-h to 24.0 kg/m^2-h at V_{d0} = 10 L/min and at V_{d0} = 20 mL/min, from 41.8 kg/m^2-h and to 27.9 kg/m^2-h (Figure 4.14B). This is attributed to the effectively lower temperature difference between two sides of hollow fiber, due to the longer retention time of distillate stream within the longer hollow fiber; therefore the temperature of the distillate increased more. However, the water production rate increased tremendously when increasing the fiber length (Figure 4.14C). At T_{b0} = 90 ℃, it is 32.0 L/h for V_{d0} = 10 L/min, and 37.2 L/h for V_{d0} = 20 L/min for a fiber length of 48.2 cm, while it is 26.0 L/h for V_{d0} = 10 L/min, and 27.9 L/h for V_{d0} = 20 L/min for a fiber length of 24.1 cm. An improved estimate of fiber properties and operating conditions are, d_i, 691 μm; d_o, 925 μm; N, 1275; L, 48.1cm; V_{b0}, 22 L/min; V_{d0} = 20 L/min; $T_{b0,}$ 90 ℃; $T_{d0,}$ 20 ℃, which will give water vapor flux of 27.9 kg/m^2-h, water production rate of 37.2 L/h and pressure drop of 20.1 kPa.

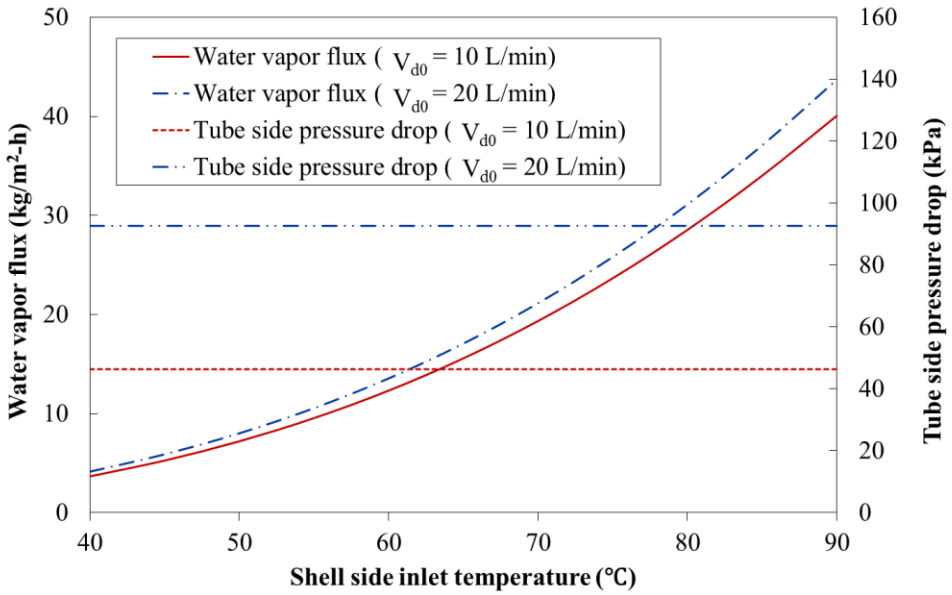

Figure 4.12 Predicted water vapor flux and tube side pressure drop at shell side inlet temperature from 40℃ to 90℃ at two sets of tube side flow rate V_{d0} = 10 L/min and V_{d0} = 20 L/min. Modeling parameters: d_i, 330 μm; d_o, 630 μm; N, 2652; L, 24.1cm; V_{b0}, 22 L/min; $T_{d0,}$ 20 ℃.

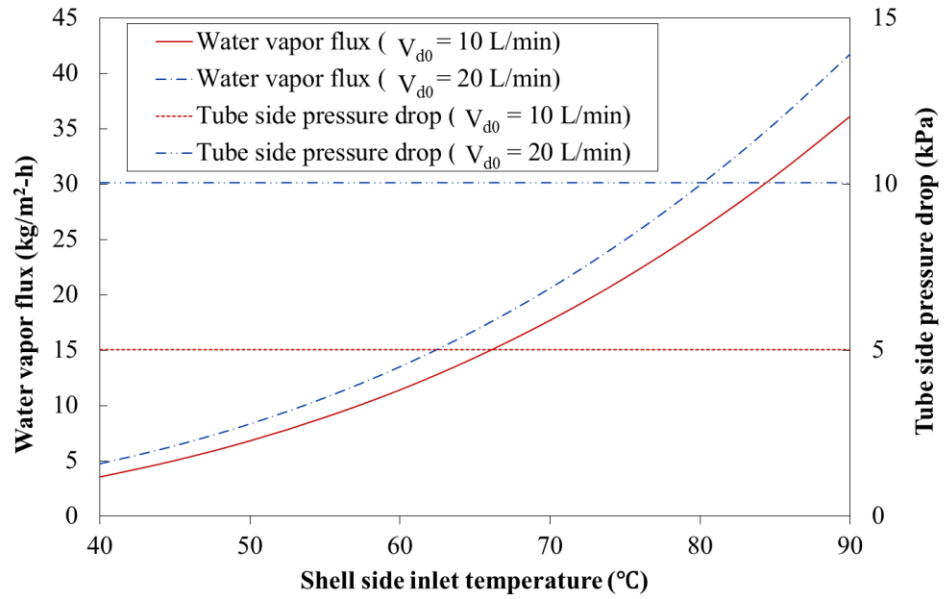

Figure 4.13 Predicted water vapor flux and tube side pressure drop at shell side inlet temperature from 40℃ to 90℃ at two sets of tube side flow rate V_{d0} = 10 L/min and V_{d0} = 20 L/min. Modeling parameters: d_i, 691 μm; d_o, 925 μm; N, 1275; L, 24.1cm; V_{b0}, 22 L/min; $T_{d0,}$ 20 ℃.

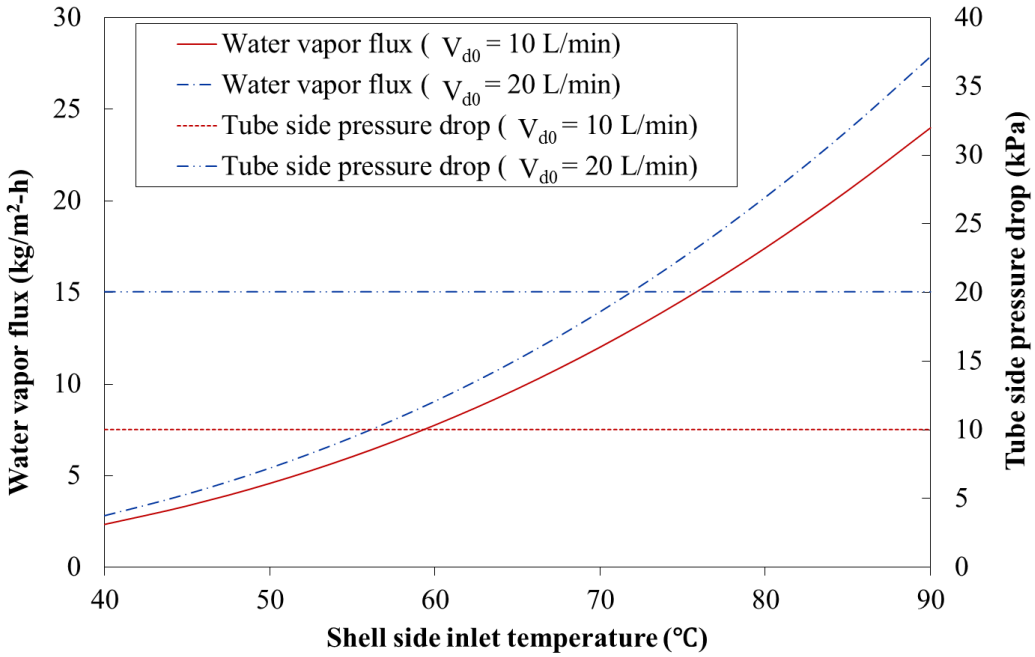

Figure 4.14A Predicted water vapor flux and tube side pressure drop at shell side inlet temperature from 40℃ to 90℃ at two sets of tube side flow rate V_{d0} = 10 L/min and V_{d0} = 20 L/min. Modeling parameters: d_i, 691 μm; d_o, 925 μm; N, 1275; L, 48.2 cm; V_{b0}, 22 L/min; $T_{d0,}$ 20 ℃.

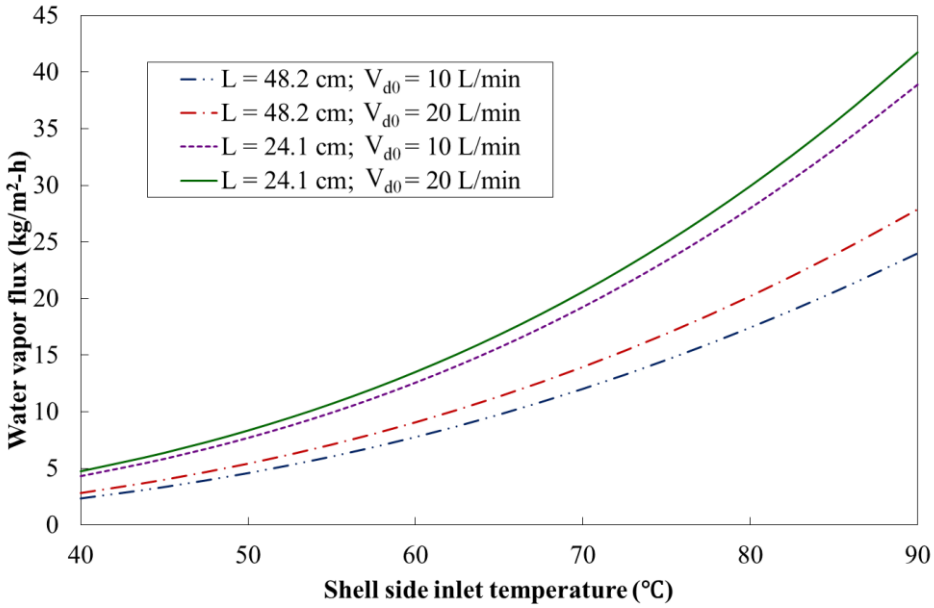

Figure 4.14B Predicted water vapor flux at shell side inlet temperature from 40℃ to 90℃ at two sets of tube side flow rate V_{d0} = 10 L/min and V_{d0} = 20 L/min. Modeling parameters: d_i, 691 μm; d_o, 925 μm; N, 1275; V_{b0}, 22 L/min; $T_{d0,}$ 20 ℃.

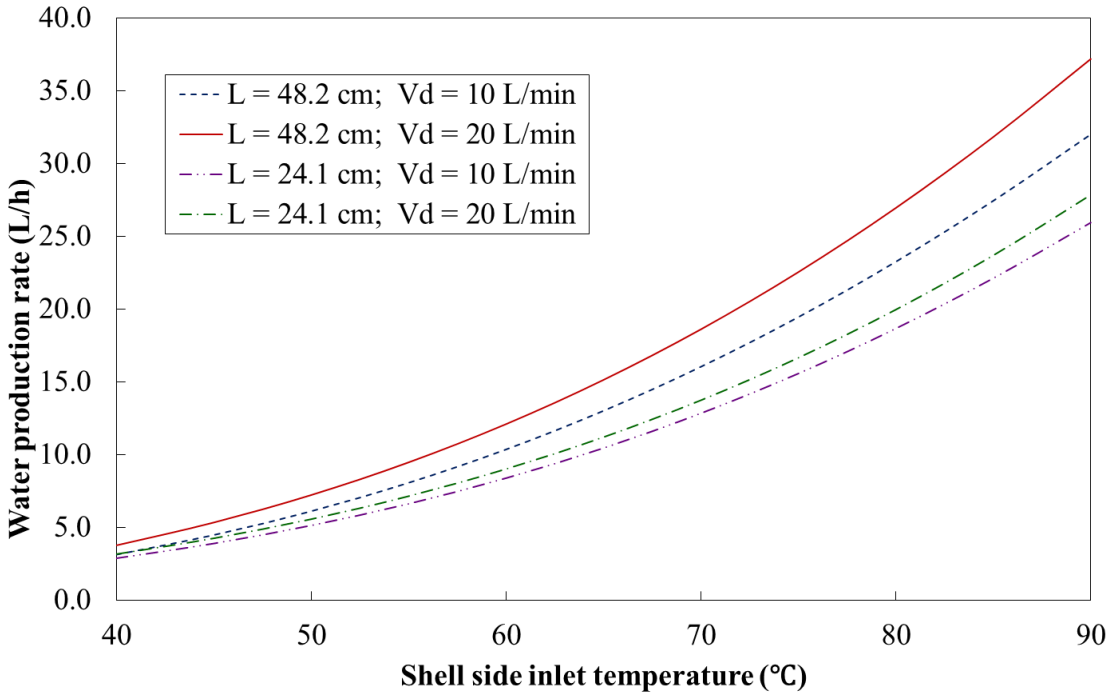

Figure 4.14C Predicted water production rate at shell side inlet temperature from 40℃ to 90℃ at two sets of tube side flow rate V_{d0} = 10 L/min and V_{d0} = 20 L/min. Modeling parameters: d_i, 691 μm; d_o, 925 μm; N, 1275; V_{b0}, 22 L/min; $T_{d0,}$ 20 ℃.

4.5 Concluding Remarks

In order to compete with RO, fouling is a major obstacle that MD technique should overcome and potentially minimize or eliminate. Various membrane module configuration and flow manipulations have been designed and proposed in order to reduce the effect of fouling on membrane performance. Previous studies showed that an application of cross flow and changing the nature of the hydrophobic coating on the surface of a large pilot scale hollow fiber module and oscillations of hollow fibers created results with no precipitation based fouling.

On the basis of previous model described for this hollow fiber module, an enhanced model was developed in this dissertation. To reduce the tube side pressure

drop, the model further simulated the performance of hollow fiber module that had larger hollow fiber ID. Module configuration (total number of hollow fiber, number of fiber per layer) and operating conditions (tube side flow rate) were systematized to compare with the original model on an equivalent basis. It would be useful to use this model as a starting point for further larger DCMD plant design and process optimization.

CHAPTER 5

GENERAL CONCLUSIONS AND RECOMMENDATIONS FOR FUTURE WORK

Eight different flat membranes of two different materials, PVDF and ePTFE with considerable variations in membrane thickness, pore size, etc. were studied for DCMD and VMD in this dissertation. Wilson plot was employed to determine boundary layer heat transfer resistance(s) in the membrane cell and membrane surface temperature(s) in DCMD and VMD. Maximum pore size and tortuosity were characterized and employed in checking out model assumptions and model results for water vapor transport models developed in Chapter 2 and Chapter 3. The performance estimates for larger hollow fiber-based MD devices were also analyzed using mathematical models developed and numerically solved in MATLAB. Good agreements (within 5% deviation) of almost all of the membrane mass transfer coefficient of water vapor and the observed water vapor fluxes were obtained between the experimental values and the simulated results predicted for either the Knudsen regime or the transition region in DCMD and VMD. Pore size distribution (PSD) does not matter if the membrane pore size variation falls entirely in the Knudsen diffusion or the transition regime. However, for membranes having nominal pore size $\cong$ 0.1 μm, $K_n \cong 1$, PSD plays an important role in DCMD. Prediction model for water vapor flux mentioned in Chapter 2 was applied to enhance the performance estimates for larger hollow fiber-based MD devices whose performances were also analyzed using mathematical models developed and numerically solved in MATLAB.

Module configuration and operating conditions were systematized to compare with the previous model on an equivalent basis.

In general, the membrane used in the MD system should have low resistance to mass transfer and low thermal conductivity to prevent heat loss across the membrane. In addition, the membrane should have good thermal stability in extreme temperatures, high resistance to chemicals, such as acids and bases and good mechanical strength and flexibility.

The ideal membrane properties for DCMD are large pore size, high porosity, and low membrane thickness (~20 μm) to achieve high water vapor flux while balancing thermal efficiency in DCMD. There is conductive heat loss due to temperature difference of two sides of the membrane surface. The larger the temperature difference, the larger the conductive heat loss hence the lower the thermal efficiency. For higher thermal efficiency, a larger thickness ~150 - 200 μm is necessary when temperature difference on two sides of the membrane is larger than 10 ℃. To achieve high thermal efficiency for thin membranes around 10 ~ 20 μm, the temperature difference on two sides of the membrane should be quite low. In DCMD, 100% of salt rejection is achieved in this dissertation.

The ideal membrane properties for VMD are high porosity, low membrane thickness and suitable pore size to achieve high water vapor flux while balancing the potential risk of salt leakage in larger pores. Generally, the larger pores of the membrane, the lower the LEP. At higher brine flow rate, when an extra above-atmosphere pressure

of brine is added to the vacuum level, it may exceed the liquid entry pressure for the membrane. For membranes having smaller pore size (0.05 μm ~0.1 μm), 100% salt rejection is achievable for high brine inlet temperature and pressure. Unlike DCMD, thermal efficiency is almost 100%, and heat transfer resistance on the vacuum side is negligible.

Thin and porous membranes should be studied in the future to check the utility of the prediction models for water vapor flux and thermal efficiency. Electron beam nano-sculpting of suspended graphene sheets may be a way of manufacturing thin and porous membrane. Studies of super hydrophobic membranes in VMD are promising since the salt leakage will be reduced drastically, water vapor flux will be very high and thermal efficiency is close to 100%. AGMD reduces conductive heat loss because of the presence of air and therefore enhance the thermal efficiency. Future investigation in AGMD is recommended such that the width of air gap can be effective controlled, because air creates additional resistance to mass transfer.

.

APPENDIX A

EXPERIMENTAL DATA IN DCMD AND VMD

Table A.1 Experimental Data for Water Vapor Flux for a Typical Set of Flow Rates for Figure 2.21

Brine temperature (°C)	**Experimental water vapor flux** (kg/m^2-h)
65	21.3
70	34.0
75	38.0
80	42.4
85	49.1

Membrane: ePTFE M-045. Brine out flow rate 385 mL/min; distillate out flow rate 460 mL/min; distillate temperature ~20°C.

Table A.2 Experimental Data for Water Vapor Flux for a Typical Set of Flow Rates for Figure 2.22

Brine temperature (°C)	**Experimental water vapor flux** (kg/m^2-h)
65	17.0
70	21.5
75	25.5
80	30.6
85	32.6

Membrane: ePTFE M-045. Brine out flow rate 136 mL/min; distillate out flow rate 425mL/min; distillate temperature ~20°C.

Table A.3 Experimental Data for Water Vapor Flux for a Typical Set of Flow Rates for Figure 2.23

Membrane	**Brine out flow rate** (℃)	**Experimental water vapor flux** (kg/m^2-h)
PVDF HVHP	250	14.7
PVDF GVHP	260	11.0
PVDF VVHP	290	8.5
ePTFE M-045	285	19.8
ePTFE M-005	290	7.1
ePTFE M-010	265	17.1
ePTFE M-020A	285	19.4
ePTFE M-020B	285	28.0

Distillate out flow rates were kept the same as brine out flow rates; brine temperature ~ 65 ℃; distillate temperature ~20℃.

Table A.4 Experimental Data for Mean Membrane Mass Transfer Coefficients for Figure 2.24

Membrane	**Brine out flow rate** (℃)	**Experimental mean membrane mass transfer coefficient** (kg/m^2-h-Pa)
PVDF HVHP	250	2.136×10^{-3}
PVDF GVHP	260	1.983×10^{-3}
ePTFE M-005	290	7.100×10^{-3}
ePTFE M-010	265	2.491×10^{-3}
ePTFE M-020A	285	4.082×10^{-3}
ePTFE M-020B	285	9.485×10^{-3}
ePTFE M-045	285	3.593×10^{-3}

Distillate temperature ~ 20℃.

Table A.5 Data for Mean Membrane Mass Transfer Coefficients for Figure 2.25

Experimental mean membrane mass transfer coefficient (kg/m^2-h-Pa)	**Predicted mean membrane mass transfer coefficient (Knudsen diffusion)** (kg/m^2-h-Pa)	**Predicted mean membrane mass transfer coefficient (Transition regime)** (kg/m^2-h-Pa)
1.444×10^{-3}	1.970×10^{-3}	1.212×10^{-3}

Membrane: PVDF VVHP. Brine out flow rate, 290 mL/min; distillate out flow rates, 290 mL/min; brine temperature ~ 65 ℃; distillate temperature ~ 20℃.

Table A.6 Experimental Data for Water Vapor Flux for a Typical Brine Out Flow Rate For Figure 3.4

Brine temperature (℃)	**VMD experimental water vapor flux** (kg/m^2-h)	**DCMD experimental water vapor flux (Table A.1; Figure 2.21)** (kg/m^2-h)
65	47.8	21.3
75	116.7	38.0
85	172.9	49.1

Membrane: ePTFE M-045. Brine out flow rate 385 mL/min; vacuum level, 92.5% of full vacuum (7600 Pa).

Table A.7 Experimental Data for Water Vapor Flux and Salt Rejection for Figure 3.5

% Vacuum Level	**Experimental water vapor flux** (kg/m^2-h)	**Salt rejection** (%)
88.2	31.8	100.0
90.0	62.1	98.3
92.5	93.7	97.2
95.0	139.4	94.5

Membrane: ePTFE M-045. Brine out flow rate 280 mL/min; brine inlet temperature 75℃.

Table A.8 Experimental Data for Water Vapor Flux for a Typical Brine Out Flow Rate for Figure 3.9

Membrane	**Experimental water vapor flux** (kg/m^2-h)
PVDF HVHP	26.4
PVDF GVHP	12.1
PVDF VVHP	5.1
ePTFE M-005	18.6
ePTFE M-010	10.1
ePTFE M-020A	24.9
ePTFE M-020B	57.1
ePTFE M-045	38.6

Brine out flow rate 285 mL/min; brine inlet temperature 65℃; vacuum level, 92.5% of full vacuum (7600 Pa).

Table A.9 Experimental Data for Membrane Mass Transfer Coefficient for Figure 3.10

Membrane	**Experimental membrane mass transfer coefficient** (kg/m^2-h-Pa)
PVDF HVHP	9.825×10^{-3}
PVDF GVHP	4.525×10^{-3}
PVDF VVHP	1.953×10^{-3}
ePTFE M-005	6.739×10^{-3}
ePTFE M-010	3.737×10^{-3}
ePTFE M-020A	9.232×10^{-3}
ePTFE M-020B	2.125×10^{-2}
ePTFE M-045	1.427×10^{-2}

Vacuum level, 92.5% of full vacuum (7600 Pa).

APPENDIX B

SAMPLE CALCULATIONS IN DCMD

B.1 Calculation of Experimental Membrane Mass Transfer Coefficient

Membrane: ePTFE M-045 for Figures 2.23 and 2.24.

Membrane area = 11 cm^2 = 0.0011 m^2

F_{bo} = 170 mL/min, F_{do} = 460 mL/min. T_{bi} = 64.4 ℃, T_{bo} = 62.8 ℃. T_{di} = 21.7 ℃, T_{do} = 21.9 ℃; T_{bm} = 63.5 ℃, T_{dm} = 21.8 ℃

Collected permeate mass production rate = 14.41 g/h; Mass flux = 13.1 kg/m^2-h

F_{di} = F_{do} – collected permeate volumetric flow rate

F_{di} = 460 mL/min - (14.4 g/h) / (1g/mL) / (60 min/1h)

F_{di} = 459.76 mL/min= 459.8 mL/min

$Q_d = F_{do}\ \rho\ C_p\ T_{do} - F_{di}\ \rho\ C_p\ T_{di}$

Q_d = 460 mL/min × 1 g/mL × 4.1813 J/K-g × (21.9+273.2)K – 459.76 mL/min × 1 g/mL × 4.1813 J/K-g × (21.7+273.2)K

$Q_t = Q_d$ = 681.9 J/min

$q^t = q^d = Q_d$ / membrane area

q^t = (681.9 J/min) / (0.0011 m^2) / (60s/min) = 10331.4 J/m^2-s = 10331.4 W/m^2

$h_0 = q^t / (T_{bm} - T_{dm})$ = (10331.4 W/m^2) / ((273.2+63.6) K-(273.2+23)K) = 247.2 W/m^2-K

$1/h_0 = 4.404\times10^{-3}$ m^2-K/W

Velocity area = 1/4*3.14* 0.96^2=0.7235 cm^2

$v_b = 170$ mL/min /0.7235 cm^2/ (60 s/min) / (100 cm/ 1 m)= 3.92×10^{-2} m/s

$v_b^{-0.6} = 6.987$

Brine side Wilson plot equation obtained from $1/ h_0$ vs. $v_b^{-0.6}$:

$1/ h_0 = 0.0003\, v_b^{-0.6} + 0.0021$

$1/h_f = 0.0003 \times v_b^{-0.6} = 0.0003 \times 6.987 = 2.096 \times 10^{-3}$

$h_f = 477.1$ W/m^2-K

$v_d = 460$ mL/min /0.7235 cm^2/ (60 s/min) / (100 cm/ 1 m)= 1.06×10^{-1} m/s

$v_d^{-0.6} = 3.072$

Distillate side Wilson plot equation obtained from $1/ h_0$ vs. $v_d^{-0.6}$

$1/ h_0 = 0.0003\, v_d^{-0.6} + 0.0022$

$1/h_d = 0.0003 \times v_d^{-0.6} = 0.0003 \times 3.07 = 0.922 \times 10^{-3}$ m^2-K/W

$h_d = 1085.1$ W/m^2-K

$1/h_m = 1/h_0 - 1/h_f - 1/h_d = 4.404 \times 10^{-3} - 2.096 \times 10^{-3} - 0.922 \times 10^{-3} = 1.386 \times 10^{-3}$ m^2-K/W

$h_m = 721.3$ W/m^2-K

$T_1 = T_{bm} - q^t/ h_f = 63.6$ ℃ –(10331.4 W/m^2)/(477.1 W/m^2-K) = 41.9ºC

$\log_{10}$ (P mmHg) = 8.07-1730.6/(233.4+T(℃))

$P_1 = 61.18$ mmHg = 61.18 mmHg × (133.3 Pa/ 1 mmHg) = 8156.2 Pa

$T_2 = T_{dm} - q^t/ h_d = 21.8$ ℃ – (10331.4 W/m^2)/(1085.1 W/m^2-K) = 31.3 ℃

$P_2 = 34.23$ mmHg = 4563.4 Pa

$k_m = J/ (P_1 - P_2) = 13.1$ kg/m^2-h /(8156.2 - 4563.4) Pa = 3.646×10^{-3} kg/m^2-h-Pa.

B.2 Prediction of Water Vapor Flux and Membrane Mass Transfer Coefficient

$$J_{predicted} = \frac{(\varepsilon/\chi)P_T D_{w-a}}{\sigma R T_m} \ln \frac{D_{Kn}(P_T - P_2) + (\varepsilon/\chi)P_T D_{w-a}}{D_{Kn}(P_T - P_1) + (\varepsilon/\chi)P_T D_{w-a}}$$

$P_T D_{w-a} = (1.895\times10^{-5}) T_m^{2.0272}$

$$D_{Kn} = \frac{4}{3}\frac{\varepsilon d}{\chi}\sqrt{\frac{RT_m}{2\pi m_w}}$$

$T_m = (T_{bm}+T_{dm})/2 = (41.9\,^oC + 31.3\,^oC)/2 = 36.6\,^oC$

$D_{Kn} = 4/3 \times (0.8 \times 0.00000045/1.25) \times \sqrt{(8.314 \times 40.59768/2/3.14/18.01528)}$

$D_{Kn} = 5.80\times10^{-5}\ m^2/s$

$P_T D_{w-a} = (1.895\times10^{-5}) T_m^{2.0272} = (1.895\times10^{-5}) \times 40.59768^{2.0272} = 2.821\ Pa\ m^2/s$

$$\frac{(\varepsilon/\chi)P_T D_{w-a}}{\sigma R T_m} = \frac{(0.8/1.25)\times2.748}{0.000098\times8.314462\times36.6} = 6.968$$

$P_T = 101325\ Pa$

$$\frac{D_{Kn}(P_T-P_2)+(\varepsilon/\chi)P_T D_{w-a}}{D_{Kn}(P_T-P_1)+(\varepsilon/\chi)P_T D_{w-a}} = \frac{5.80\times10^{-5}(101325-4563.4)+(0.8/1.25)\times2.821}{5.80\times10^{-5}(101325-8156.2)+(0.8/1.25)\times2.821} = 1.029$$

$$\ln\frac{D_{Kn}(P_T-P_2)+(\varepsilon/\chi)P_T D_{w-a}}{D_{Kn}(P_T-P_1)+(\varepsilon/\chi)P_T D_{w-a}} = \ln 1.028978 = 0.028$$

$$J_{predicted} = \frac{(\varepsilon/\chi)P_T D_{w-a}}{\sigma R T_m} \ln \frac{D_{Kn}(P_T-P_2)+(\varepsilon/\chi)P_T D_{w-a}}{D_{Kn}(P_T-P_1)+(\varepsilon/\chi)P_T D_{w-a}} = 6.968\times0.028$$

$J_{predicted} = 0.199\ mol/m^2\text{-}s$

$J_{predicted} = (0.199\ mol/m^2\text{-}s) \times (18g/mol) \times (1kg/1000g) \times (3600s/1h)$

$J_{predicted} = 12.89\ kg/m^2\text{-}h$

$J_{experimental} = 13.1\ kg/m^2\text{-}h$

Error: (13.1-12.89)/13.1 = 0.21/13.1=0.016=1.6%

$k_{m\text{-}predicted} = (12.89\ kg/m^2\text{-}h)/(8156.2 - 4563.4)\ Pa = 3.588\times10^{-3}$

$k_{m\text{-}experimental} = 3.646\times10^{-3}\ kg/m^2\text{-}h\text{-}Pa.$

Deviation: $(3.646\times10^{-3} - 3.588\times10^{-3})/\ 3.646\times10^{-3} = 0.0159 = 1.6\%$

B.3 Calculation of Thermal Efficiency

$\eta\%$ = mass flow rate × latent heat of vaporization of water / total rate of heat transferred × 100

$\eta\%$ = 14.4 g/h × 2260 J/g / 681.88 J/min / 60 (min/h) × 100 = 79.5%

B.4 Prediction of Heat Transfer Coefficients

Sieder-Tate equation:

$$\mathrm{Nu} = \frac{\mathrm{hd}}{\mathrm{k}} = 1.86\left(\frac{\mathrm{d}}{\mathrm{L}}\right)^{0.33}(\mathrm{RePr})^{0.33}\left(\frac{\mu}{\mu_{\mathrm{wi}}}\right)^{0.14}$$

$$\mathrm{Re} = \frac{\mathrm{du}\rho}{\mu};\ \mathrm{Pr} = \frac{\mathrm{C_p}\mu}{\mathrm{k}}$$

$$\mathrm{h} = 1.86\left(\frac{\mathrm{d}}{\mathrm{L}}\right)^{0.33}(\mathrm{RePr})^{0.33}\frac{\mathrm{k}}{\mathrm{d}}$$

$$\mathrm{h} = 1.86\left(\frac{\mathrm{d}}{\mathrm{L}}\right)^{0.33}\left(\frac{\mathrm{du}\rho}{\mu}\right)^{0.33}\left(\frac{\mathrm{C_p}\mu}{\mathrm{k}}\right)^{0.33}\frac{\mathrm{k}}{\mathrm{d}}$$

$$\frac{\mathrm{h}_{70^{o}\mathrm{C}}}{\mathrm{h}_{65^{o}\mathrm{C}}} = \left(\frac{\rho_{70^{o}\mathrm{C}}}{\rho_{65^{o}\mathrm{C}}}\right)^{0.33}\left(\frac{\mathrm{C_p}_{70^{o}\mathrm{C}}}{\mathrm{C_p}_{65^{o}\mathrm{C}}}\right)^{0.33}\left(\frac{\mathrm{k}_{70^{o}\mathrm{C}}}{\mathrm{k}_{65^{o}\mathrm{C}}}\right)^{0.67}\left(\frac{\mu_{70^{o}\mathrm{C}}}{\mu_{65^{o}\mathrm{C}}}\right)^{0.14}$$

Using water properties in Table B.1,

Table B.1 Water Properties

T	$\boldsymbol{\rho}$	$\mathbf{C_p}$	**k**	$\boldsymbol{\mu}$
°C	kg/m^3	J/g-K	W/m-K	Pa·s
65	980.45	4.188	0.6573	0.434
70	977.63	4.191	0.6611	0.404
75	974.68	4.194	0.6644	0.378
80	971.6	4.198	0.6671	0.355
85	968.39	4.203	0.6693	0.334

$$\frac{\mathrm{h}_{70^{o}\mathrm{C}}}{\mathrm{h}_{65^{o}\mathrm{C}}} = 0.993$$

Predicted $\mathrm{h}_{\mathrm{f}-70^{o}\mathrm{C}}$=463.707×0.993=460.55 W/m^2-K

Experimental h_{f-70^oC}=477.10 W/m^2-K

Deviation: (477.10 - 460.55) / 460.55 =0.0359= -3.59%

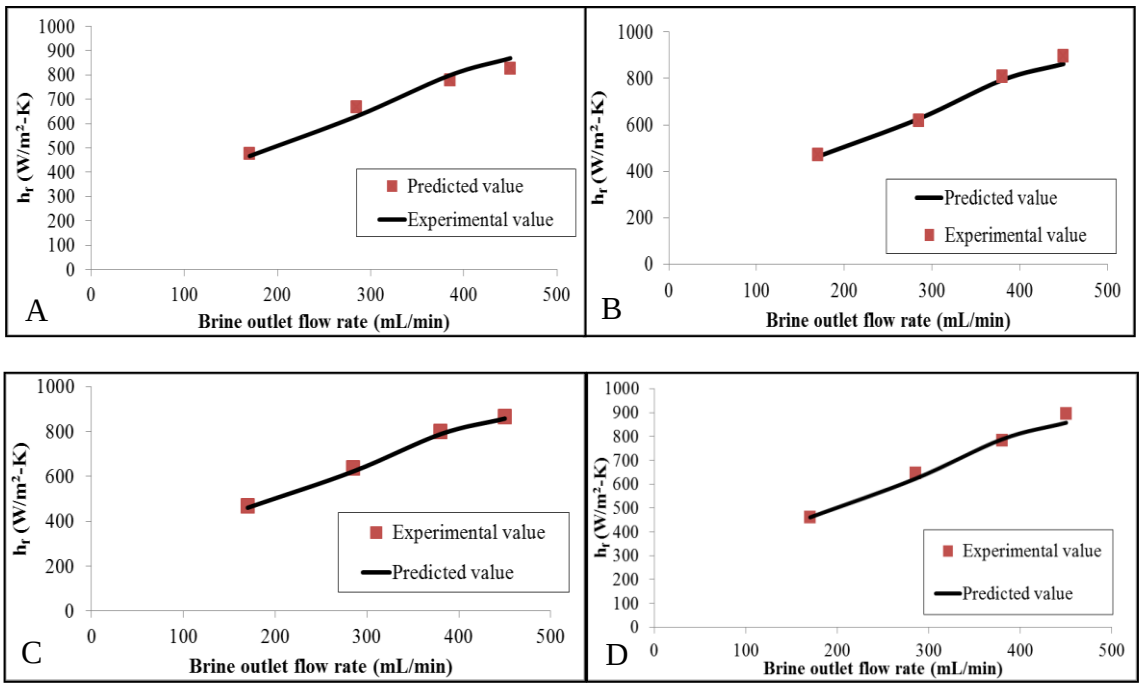

Figure B.1 Experimental and predicted brine side heat transfer coefficients for various brine flow rates for Gore M-045 membrane in CPVC cell. Distillate flow rate 460 mL/min. Distillate inlet temperature 20 ℃. **(A)** Brine-in temperatures 70 ℃. **(B)** Brine-in temperatures 75 ℃. **(C)** Brine-in temperatures 80 ℃. **(D)** Brine-in temperatures 85 ℃. h_f deviation within 5%.

APPENDIX C

SAMPLE CALCULATIONS IN VMD

C.1 Calculation of Experimental and Predicted Water Vapor Flux and Membrane Mass Transfer Coefficient

Membrane area: 0.0011 m^2.

Membrane: PVDF VVHP 047000 (Figures 3.9 and 3.10)

F_{bo} = 510 mL/min, Vacuum level 7600 Pa (92.5% of full vacuum), T_{bi} = 85.4℃, T_{bo} = 85.2 ℃, T_{bm} = 85.3℃

Predicted h_f = 857.3 W/m^2-K (Calculated from Appendix B.4)

Collected permeate mass rate = 33.0 g/h; Mass flux = 30.0 kg/m^2-h

$F_{bi} = F_{bo}$ + collected permeate volumetric flow rate

F_{bi} = 510 mL/min + (33 g/h) / (1g/mL) / (60 min/1h)

F_{bi} = 510.6 mL/min

$Q_b = F_{bi}\ \rho\ C_p\ T_{bi} - F_{bo}\ \rho\ C_p\ T_{bo}$

Q_b = 510.6 mL/min × 1 g/mL × 4.1813 J/K-g × (85.4+273.2)K – 510 mL/min × 1 g/mL × 4.1813 J/K-g × (85.2 + 273.2)K

= 1251.0 J/min

$Q_t = Q_b$ = 1251.0 J/min

q^t =1251.0 / 0.0011 /60= 18955.0 W/m^2

$T_1 = T_{bm} - q^t / h_f$ = 85.3℃ – (18955.0 W/m^2)/(857.3 W/m^2-K) = 63.2℃

$T_1 = T_2 = T_m = 63.2℃$

$\log_{10}(P\ mmHg) = 8.07131 - 1730.63/(233.43 + T(^oC))$

$P_1 = 172.6\ mmHg = 172.6\ mmHg \times (133.322\ Pa / 1\ mmHg) = 23009.0\ Pa$

$P_2 = 7600\ Pa$

$P_{mean} = (P_1 + P_v)/2 = (23009 + 7600)/2 = 15304.5\ Pa$

$K_0 = \varepsilon d_m / 3\chi = 0.8 \times 4.5 \times 10^{-7} / 3 / (1/0.8) = 9.6 \times 10^{-8}$

$B_0 = \varepsilon d_m^2 / 32\ \chi = 0.8 \times (4.5 \times 10^{-7})^2 / 32 / (1/0.8) = 4.05 \times 10^{-15}$

$$J_{predicted} = \frac{1}{RT\delta_M}\left[K_0\left(\frac{8RT}{\pi M_W}\right)^{0.5} + B_0\left(\frac{P_m}{\mu}\right)\right](P_1 - P_v) = 1/8.314/(85.3+273.15)/(1.25 \times 10^{-6})$$

$\times [9.6 \times 10^{-8} \times (8 \times 8.314 \times (63.6+273.15)/3.14/(18/1000))^{0.5} + 4.05 \times 10^{-15} \times 15304.5 / 0.000653] \times (23009-7600) = 0.453\ J/mol\text{-}s = 29.4\ kg/m^2\text{-}h$

$J_{exp} = 30.0\ kg/m^2\text{-}h$

Deviation: $(30.0 - 29.4)/30.0 = 0.02 = 2\%$

$k_{m\text{-}predictied} = J_{predicted}/(P_1 - P_2) = 29.4\ kg/m^2\text{-}h/(23009-7600)\ Pa = 1.908 \times 10^{-3}\ kg/m^2\text{-}h\text{-}Pa.$

$k_{m\text{-}exp} = J_{exp}/(P_1 - P_2) = 30.0\ kg/m^2\text{-}h/(23429-7600)\ Pa = 1.947 \times 10^{-3}\ kg/m^2\text{-}h\text{-}Pa.$

Deviation: $(1.947 \times 10^{-3} - 1.908 \times 10^{-3})/(1.947 \times 10^{-3}) = 0.02 = 2\%$

C.2 Calculation of Thermal Efficiency

$\eta\%$ = mass flow rate × latent heat of vaporization of water / total rate of heat transferred × 100%

$\eta\% = 33\ g/h \times 2260\ J/g / 1251.0\ J/min / 60\ (min/h) \times 100\% = 0.9936 = 99.4\ \%$

APPENDIX D

PROGAMS FOR PERFORMANCE ESTIMATES FOR LARGE HOLLOW FIBER-BASED DCMD DEVICES

```
% This program was originally developed by Song, et al. (2008) for modeling the heat transfer and mass transfer in DCMD processes. It was modified by Lin Li. With hollow fiber properties, inputs of flow rate, temperature of brine and distillate, it will allow one to estimate the fiber inside and outside wall temperature, the values of water vapor flux, water production rate, thermal efficiency and TPC.
%
clc
clear
 % Specifications of fiber dimensions
di = 0.000691; % fiber inside diameter, m
do = 0.000925; % fiber outside diameter, m
dln = (do-di)/log(do/di); % fiber log mean diameter, m
delta = (do-di)/2; % fiber wall thickness, m
L = 0.241; % effective fiber length, m
Arf = do/di; % ratio of outside surface area to inside surface area
Arln = dln/di; % ratio of log mean surface area to inside surface area
Arp = di/di; % ratio of inside surface area to inside surface area
phai = 3.1415; % constant
n = 75; % number of fiber for each layer
m = 17; % number of fiber layer
N = 1275; % total fiber number
 % Internal dimensions of module frame
Lf = 0.241; % frame length, m
Wf = 0.089; % frame width, m
alpha = n*phai*di; % surface area per unit length for each layer, m^2/m
CrossArea_shell = Lf*Wf-do*Lf*n; % open cross section area for shell side liquid flow, m^2
CrossArea_tube = phai/4*di^2*N; % open cross section area for tube side liquid flow, m^2
MemArea = phai*di*L*N; % effective membrane surface area
 %Feed conditions
Cbb = input('shell side feed bulk concentration (mMol):  ');
EVfo = input('shell side flow rate (mL/min):  '); % experimentally shell side flow rate, mL/min
ETfo = input('shell side feed temperature (C):  '); % experimentally shell side feed temperature, C
```

```
EVPo = input('distillate feed flow rate (mL/min):  '); % experimentally tube side flow rate, mL/min
ETpo = input('distillate feed temperature (C):  '); % experimentally tube side distillate feed temperature, C
Vfo = EVfo/1000000*60; % brine feed rate, m^3/h
Tfo = ETfo; % brine feed inlet temperature, C
VPo = EVPo/1000000*60; % distillate feed rate, m^3/h
Tpo = ETpo; % distillate feed inlet temperature, C
Vpopl = VPo/m; % distillate feed rate of each fiber layer, m^3/h
uo = (Vfo/3600)/CrossArea_shell; % interstitial velocity on the shell side, m/s
ui = (VPo/3600)/CrossArea_tube; % linear velocity on the tube side (fiber lumen), m/s
Cp=4.1813; %liquid water heat capacity taken as constant, kJ/kg-C
%calculate heat transfer coefficient on the shell side
% Zukauskus equation
Fc = 1; % correction factor (=1 for fiber layer > 10)
Reo = do*uo*rho(Tfo+273.15)/mu(Tfo+273.15); % Renolds number on the shell side
Pro =Cp*1e3*mu(Tfo+273.15)/kc(Tfo+273.15); % Prandtl number on the shell side at bulk temperature Tfo
Prw = Pro; % Prandtl number at the shell side wall temperature
if Reo <= 40
   hf = kc(Tfo+273.15)/do*(1.04*Reo^0.4*Pro^0.36*(Pro/Prw)^0.25*Fc); % shell-side heat transfer coefficient, W/m^2.K
else
   hf = kc(Tfo+273.15)/do*(0.71*Reo^0.5*Pro^0.36*(Pro/Prw)^0.25*Fc); % shell-side heat transfer coefficient, W/m^2.K
end
 %calculate heat transfer coefficient on the tube side
%Sieder-Tate correlation
muw = mu(Tpo+273.15); % viscosity at the tube side wall temperature
Rei = di*ui*rho(Tpo+273.15)/mu(Tpo+273.15) % Reynolds number on the tube side
Pri = Cp*1e3*mu(Tpo+273.15)/kc(Tpo+273.15); % Prandtl number on tube side
hp = kc(Tpo+273.15)/di*(1.86*(di/L)^0.33*(Rei*Pri)^0.33*(mu(Tpo+273.15)/muw)^0.14); % tube-side heat transfer coefficient, W/m^2.K
%hp=kc(Tpo+273.15)/di*4.36;
kpp = 0.18; % thermal conductivity for PVDF, W/m.K
kair = 0.025; % thermal conductivity for air, W/m.K
poredi=0.6; % membrane pore size, um
poros = 0.8; % membrane porosity
tortuos=1.25; % membrane tortuosity
```

```
hmg = kair/delta; % heat transfer coefficient across the air trapped in membrane pores, W/m^2.K
hms = kpp/delta; % heat transfer coefficient across solid membrane wall, W/m^2.K
hm = poros*hmg+(1-poros)*hms; % heat transfer coefficient through fiber wall and air trapped in the pores, W/m^2.K
 % Loop begins to calculate temprature profiles, stream flow rates, and
% water production flux rate, etc.
h = L/100;              % step size
StepN = L/h;            % loop number
A = hf*Arf*alpha;
B = hp*Arp*alpha;
C = hm*Arln*alpha;
D = 0.0014*deltaH(Tfo+273.15)*Arp*alpha/3.6;
E = 0.0014*Arp*alpha*Cp*h/3.6;
epsilon = 1e-3;
Tpo_old = Tpo;
X(m,StepN)=0;
z(m,StepN)=0;
Tf1(m,StepN)=0;
for j = 1:m               % jth fiber layer
   if j < 2
      mspo = rho(Tpo+273.15)*Vpopl;     % distillate feed inlet mass flow rate per layer, kg/h
      msfo = rho(Tfo+273.15)*Vfo;    % brine feed inlet mass flow rate, kg/h
      for i = 1:StepN
         X(j,i) =j;
         z(j,i) = i*h;
         deltaTfm = 5;
         deltaTpm = 5;
         deltaTp = 5;
         Tf1(j,i) = Tfo; % Tf1 is an array for saving shell side brine feed temperature along the fiber length, K
         Tfm_c = Tf1(j,i);
         Tpm_c = Tpo_old;
         Tp_c = Tpo_old;
         while abs(deltaTfm)>epsilon | abs(deltaTpm)>epsilon | abs(deltaTp)>epsilon
            f1 = A*(Tf1(j,i)-Tfm_c)-B*(Tpm_c-Tp_c);
            f2          =          B*(Tpm_c-Tp_c)-C*(Tfm_c-Tpm_c)-D*(10^3*exp(16.260-3799.89/(Tfm_c+273.15-46.8))-10^3*exp(16.260-3799.89/(Tpm_c+273.15-46.8)));
```

```
        f3 = mspo*Cp*Tpo_old/3.6+B*h*(Tpm_c-Tp_c)-(mspo*Cp/3.6+E*(10^3*exp(16.260-3799.89/(Tfm_c+273.15-46.8))-10^3*exp(16.260-3799.89/(Tpm_c+273.15-46.8))))*Tp_c;
        f11 = -A;
        f12 = -B;
        f13 = B;
        f21 = -C-D*10^3*exp(16.260-3799.89/(Tfm_c+273.15-46.8))*(3799/(Tfm_c+273.15-46.8)^2);
        f22 = (B+C)+D*10^3*exp(16.260-3799.89/(Tpm_c+273.15-46.8))*(3799/(Tpm_c+273.15-46.8)^2);
        f23 = -B;
        f31 = -E*Tp_c*10^3*exp(16.260-3799.89/(Tfm_c+273.15-46.8))*(3799/(Tfm_c+273.15-46.8)^2);
        f32 = B*h+E*Tp_c*10^3*exp(16.260-3799.89/(Tpm_c+273.15-46.8))*(3799/(Tpm_c+273.15-46.8)^2);
        f33 = -B*h-(mspo*Cp/3.6+E*(10^3*exp(16.260-3799.89/(Tfm_c+273.15-46.8))-10^3*exp(16.260-3799.89/(Tpm_c+273.15-46.8))));
        MF = [f1; f2; f3];
        MC = [f11 f12 f13; f21 f22 f23; f31 f32 f33];
        deltaT = -inv(MC)*MF;
        deltaTfm = deltaT(1);
        deltaTpm = deltaT(2);
        deltaTp = deltaT(3);
        Tfm_c = Tfm_c + deltaTfm;
        Tpm_c = Tpm_c + deltaTpm;
        Tp_c = Tp_c + deltaTp;
    end
    dQdx(j,i) = hf*Arf*alpha*(Tf1(j,i)-Tfm_c); % change of heat transfer rate along the fiber length, W/m
    Tfm(j,i) = Tfm_c; % Tfm is an array for saving shell side fiber wall temperature along the fiber length, K
    Tpm(j,i) = Tpm_c; % Tpm_s is an array for saving tube side fiber wall temperature along the fiber lenght, K
    Tp(j,i) = Tp_c; % Tp_t is an array for saving bulk temperature in the distillate side along the fiber length, K
    deltaTfmTpm (j,i) = Tfm_c - Tpm_c; % wall temperature difference between shell side and tube side along the fiber length, K
    Pfm = 10^3*exp(16.260-3799.89/(Tfm_c+273.15-46.8)); % water vapor pressure at the brine side wall temperature, Pa
    Ppm = 10^3*exp(16.260-3799.89/(Tpm_c+273.15-46.8)); % water vapor pressure at the distillate side wall temperature, Pa
```

```
        deltaPfmPpm(j,i)=Pfm-Ppm;
        Nv(j,i) = (poros/ tortuos) * (1.895/100000) * ((Tfm(j,i)+Tpm(j,i))/2+273.2)
^2.072/dln /8.314/((Tfm(j,i)+Tpm(j,i)/2+273.2)* ln (((4/3* (poros/tortuos)
*(poredi/1000000)*(8.314*((Tfm(j,i)+Tpm(j,i))/2+273.2)/2/3.14/0.018)^0.5*(101325-
Pfm(j,i))+ (poros/ tortuos)* (1.895/100000) * ((Tfm(j,i)+Tpm(j,i)) /2+273.2)^2.072))/
((4/3* (poros/tortuos)* (poredi/1000000)* (8.314*((Tfm(j,i)+Tpm(j,i))/2+273.2)
/2/3.14/0.018)^0.5*(101325- Ppm(j,i))+ (poros/ tortuos)*
*(1.895/100000)*((Tfm(j,i)+Tpm(j,i))/2+273.2)^2.072))); % kg/m^2-hr
        msf1(j,i) = msfo; % shell side brine inlet mass flow rate, kg/h
        msf2(j,i) = msf1(j,i)-L*Nv(j,i)*Arp*alpha;
        Tf2(j,i) = (msf1(j,i)*Cp*Tf1(j,i)/3.6-L*dQdx(j,i))/((msf1(j,i)-
L*Nv(j,i)*Arp*alpha)/3.6*Cp);
         Sco=mu(Tfo+273.15)/(Dcaso4(Tfo)*rho(Tfo+273.15));
        Fc = 1; % correction factor (=1 for fiber layer > 10)
        Reo = do*uo*rho(Tfo+273.15)/mu(Tfo+273.15); % Renolds number on the shell
side
          if Reo <= 40
            kd = Dcaso4(Tf2(j,i))/do*(1.04*Reo^0.4*Sco^0.36*Fc); % shell-side heat
transfer coefficient, m/s
          else
            kd = Dcaso4(Tf2(j,i))/do*(0.71*Reo^0.5*Sco^0.36*Fc); % shell-side heat
transfer coefficient, m/s
          end
        CP(j,i)=exp(Nv(j,i)/(Arf*3600*rho(Tf2(j,i)+273.15)*kd));
        Tfmean=0.5*(Tf1(j,i)+Tf2(j,i));
        SI(j,i)=SIAN(Tfmean);
        DeltSI(j,i)=Cbb*(CP(j,i)-1)*0.0224*exp(0.0205*Tfmean);
        SICORR(j,i)=SI(j,i)+DeltSI(j,i);
        SI2(j,i)=SIGYP(Tfmean); % for SI of gypsum
        DeltSI2(j,i)=Cbb*(CP(j,i)-1)*0.049*exp(0.003*Tfmean);
        SICORR2(j,i)=SI2(j,i)+DeltSI2(j,i);
        TPC(j,i) = (Tfm(j,i)-Tpm(j,i))/((Tf1(j,i)+Tf2(j,i))/2-Tp(j,i)); % temperature
polarization coefficient
        eta(j,i) = (Nv(j,i)*Arp*alpha*Hv(Tf1(j,i)))/(3.6*dQdx(j,i)); % change of engergy
efficiency along fiber length, dimensionless
        mspo = mspo+ Nv(j,i)*Arp*alpha*h; % kg/hr
        msp(j,i) = mspo;
        Tpo_old = Tp_c;
      end
      WaterProduct_layer(j) = msp(j,end)-rho(Tpo+273.15)*Vpopl; % water producion
rate for j fiber layer, kg/h
```

```
    WaterProductionFlux_layer(j) = WaterProduct_layer(j)/(MemArea/m);
    eta_average(j) = WaterProduct_layer(j)*Hv(Tp(j,end))/(msp(j,end)*Cp*Tp(j,end)-
rho(Tpo+273.15)*Vpopl*Cp*Tpo);
  else
    mspo = rho(Tpo+273.15)*Vpopl;    % distillate feed inlet mass flow rate per layer,
kg/h
    Tpo_old = Tpo;
    for i = 1:StepN
      X(j,i) =j;
      z(j,i) = i*h;
      deltaTfm = 5;
      deltaTpm = 5;
      deltaTp = 5;
      Tf1(j,i) = Tf2(j-1,i); % Tf1 is an array for saving shell side brine feed temperature
along the fiber length, K
      Tfm_c = Tf1(j,i);
      Tpm_c = Tpo_old;
      Tp_c = Tpo_old;
      while abs(deltaTfm)>epsilon | abs(deltaTpm)>epsilon | abs(deltaTp)>epsilon
        f1 = A*(Tf1(j,i)-Tfm_c)-B*(Tpm_c-Tp_c);
        f2 = B*(Tpm_c-Tp_c)-C*(Tfm_c-Tpm_c)-D*(10^3*exp(16.260-
3799.89/(Tfm_c+273.15-46.8))-10^3*exp(16.260-3799.89/(Tpm_c+273.15-46.8)));
        f3 = mspo*Cp*Tpo_old/3.6+B*h*(Tpm_c-Tp_c)-
(mspo*Cp/3.6+E*(10^3*exp(16.260-3799.89/(Tfm_c+273.15-46.8))-10^3*exp(16.260-
3799.89/(Tpm_c+273.15-46.8))))*Tp_c;
        f11 = -A;
        f12 = -B;
        f13 = B;
        f21 = -C-D*10^3*exp(16.260-3799.89/(Tfm_c+273.15-
46.8))*(3799/(Tfm_c+273.15-46.8)^2);
        f22 = (B+C)+D*10^3*exp(16.260-3799.89/(Tpm_c+273.15-
46.8))*(3799/(Tpm_c+273.15-46.8)^2);
        f23 = -B;
        f31 = -E*Tp_c*10^3*exp(16.260-3799.89/(Tfm_c+273.15-
46.8))*(3799/(Tfm_c+273.15-46.8)^2);
        f32 = B*h+E*Tp_c*10^3*exp(16.260-3799.89/(Tpm_c+273.15-
46.8))*(3799/(Tpm_c+273.15-46.8)^2);
        f33 = -B*h-(mspo*Cp/3.6+E*(10^3*exp(16.260-3799.89/(Tfm_c+273.15-
46.8))-10^3*exp(16.260-3799.89/(Tpm_c+273.15-46.8))));
        MF = [f1; f2; f3];
        MC = [f11 f12 f13; f21 f22 f23; f31 f32 f33];
```

```
        deltaT = -inv(MC)*MF;
        deltaTfm = deltaT(1);
        deltaTpm = deltaT(2);
        deltaTp = deltaT(3);
        Tfm_c = Tfm_c + deltaTfm;
        Tpm_c = Tpm_c + deltaTpm;
        Tp_c = Tp_c + deltaTp;
    end
    dQdx(j,i) = hf*Arf*alpha*(Tf1(j,i)-Tfm_c); % change of heat transfer rate along the fiber length, W/m
    Tfm(j,i) = Tfm_c; % Tfm is an array for saving shell side fiber wall temperature along the fiber length, K
    Tpm(j,i) = Tpm_c; % Tpm_s is an array for saving tube side fiber wall temperature along the fiber lenght, K
    Tp(j,i) = Tp_c; % Tp_t is an array for saving bulk temperature in the distillate side along the fiber length, K
    deltaTfmTpm (j,i) = Tfm_c - Tpm_c; % wall temperature difference between shell side and tube side along the fiber length, K
    Pfm = 10^3*exp(16.260-3799.89/(Tfm_c+273.15-46.8)); % water vapor pressure at the brine side wall temperature, Pa
    Ppm = 10^3*exp(16.260-3799.89/(Tpm_c+273.15-46.8)); % water vapor pressure at the distillate side wall temperature, Pa
    deltaPfmPpm(j,i)=Pfm-Ppm;
    Nv(j,i) = (poros/ tortuos) * (1.895/100000) * ((Tfm(j,i)+Tpm(j,i))/2+273.2) ^2.072/dln /8.314/((Tfm(j,i)+Tpm(j,i)/2+273.2)* ln (((4/3* (poros/tortuos) *(poredi/1000000)*(8.314*((Tfm(j,i)+Tpm(j,i))/2+273.2)/2/3.14/0.018)^0.5*(101325- Pfm(j,i))+ (poros/ tortuos)* (1.895/100000) * ((Tfm(j,i)+Tpm(j,i)) /2+273.2)^2.072))/ ((4/3* (poros/tortuos)* (poredi/1000000)* (8.314*((Tfm(j,i)+Tpm(j,i))/2+273.2) /2/3.14/0.018)^0.5*(101325- Ppm(j,i))+ (poros/ tortuos)* *(1.895/100000)*((Tfm(j,i)+Tpm(j,i))/2+273.2)^2.072))) % kg/m^2.hr
    msf1(j,i) = msf2(j-1,i); % shell side brine inlet mass flow rate, kg/h
    msf2(j,i) = msf1(j,i)-L*Nv(j,i)*Arp*alpha;
    Tf2(j,i) = (msf1(j,i)*Cp*Tf1(j,i)/3.6-L*dQdx(j,i))/((msf1(j,i)-L*Nv(j,i)*Arp*alpha)/3.6*Cp);
    % The following code calculates the concentration polarization
    % on the brine side of the DCMD using a mass transfer analogue
    % of the Zukauskas equation
    Sco=mu(Tfo+273.15)/(Dcaso4(Tfo)*rho(Tfo+273.15));
    Fc = 1; % correction factor (=1 for fiber layer > 10)
    Reo = do*uo*rho(Tfo+273.15)/mu(Tfo+273.15); % Renolds number on the shell side
```

```
            if Reo <= 40
               kd = Dcaso4(Tf2(j,i))/do*(1.04*Reo^0.4*Sco^0.36*Fc); % shell-side heat transfer coefficient, m/s
            else
               kd = Dcaso4(Tf2(j,i))/do*(0.71*Reo^0.5*Sco^0.36*Fc); % shell-side heat transfer coefficient, m/s
            end
         CP(j,i)=exp(Nv(j,i)/(Arf*3600*rho(Tf2(j,i)+273.15)*kd));
         Tfmean=0.5*(Tf1(j,i)+Tf2(j,i));
         SI(j,i)=SIAN(Tfmean);
         DeltSI(j,i)=Cbb*(CP(j,i)-1)*0.0224*exp(0.0205*Tfmean);
         SICORR(j,i)=SI(j,i)+DeltSI(j,i);
         SI2(j,i)=SIGYP(Tfmean); % for SI of gypsum
         DeltSI2(j,i)=Cbb*(CP(j,i)-1)*0.049*exp(0.003*Tfmean);
         SICORR2(j,i)=SI2(j,i)+DeltSI2(j,i);
         TPC(j,i) = (Tfm(j,i)-Tpm(j,i))/((Tf1(j,i)+Tf2(j,i))/2-Tp(j,i)); % temperature polarization coefficient
         eta(j,i) = (Nv(j,i)*Arp*alpha*Hv(Tf1(j,i)))/(3.6*dQdx(j,i)); % change of engergy efficiency along fiber length, dimensionless
         mspo = mspo+ Nv(j,i)*Arp*alpha*h; % kg/hr
         msp(j,i) = mspo;
         Tpo_old = Tp_c;
      end
      WaterProduct_layer(j) = msp(j,end)-rho(Tpo+273.15)*Vpopl; % water producion rate for j fiber layer, kg/h
      WaterProductionFlux_layer(j) = WaterProduct_layer(j)/(MemArea/m);
      eta_average(j) = WaterProduct_layer(j)*Hv(Tp(j,end))/(msp(j,end)*Cp*Tp(j,end)-rho(Tpo+273.15)*Vpopl*Cp*Tpo);
   end
end
Tfstage=Tf2(m,:);
[rown,coln]=size(Tfstage);
for j=1:coln
   Tfstagem(j)=Tfstage(coln-j+1);
end;
% calculate distillate temperature and mass flow rate, average flux rate
msp_in = rho(Tpo+273.15)*VPo; % Overall distillate feed mass flow rate, kg/h
msp_out =0;
QpSum_out = 0;
for k = 1:m
   msp_out = msp_out+msp(k,end);
```

```
   QpSum_out = QpSum_out + msp(k,end)*Cp*Tp(k,end);
end
Tp_out = QpSum_out/(msp_out*Cp);
Tp_out = QpSum_out/(msp_out*Cp);
VP_out = msp_out/rho(Tp_out);
QpSum_in = msp_in*Cp*Tpo;
OverallWaterProduct = msp_out - msp_in; % water production rate, kg/h
Nv_average = OverallWaterProduct/MemArea; % average water production flux rate, kg/m^2.h
eta_overall = OverallWaterProduct*Hv(Tp_out)/(msp_out*Cp*Tp_out-msp_in*Cp*Tpo);
 msf_in = rho(Tfo+273.15)*Vfo;  % overall brine feed inlet mass flow rate, kg/h
msf_out = 0;
QfSum_out = 0;
for t = 1:StepN
   msf_out = msf_out + msf2(m,t);
   QfSum_out = QfSum_out + msf2(m,t)*Cp*Tf2(m,t);
end
msf_out = msf_out/StepN; % shell side brine outlet mass flow rate, kg/h
QfSum_in = msf_in*Cp*Tfo;
QfSum_out = QfSum_out/StepN;
Tf_out = QfSum_out/(msf_out*Cp); % shell side brine outlet temperature, K
Vf_out = msf_out/rho(Tf_out);
Change_msf = msf_in - msf_out;
Change_msp = msp_out - msp_in ;
Change_QpSum = QpSum_out-QpSum_in;
Change_QfSum = QfSum_in-QfSum_out;
fprintf('Tf_inlet=%8.4f C',Tfo)
fprintf(' Tp_inlet=%8.4f C',Tpo)
fprintf('Tf_out=%8.4f C',Tf_out)
fprintf('Tp_out=%8.4f C'; Tp_out)
fprintf('Nv_average=%8.4f kg/m^2.h; '; Nv_average)
fprintf('Overall Water Production Rate=%8.4f kg/h\n',OverallWaterProduct)
fprintf('Overall energy efficiency=%8.4f\n', eta_overall)
fprintf('Loss of brine mass=%8.3f\n', Change_msf)
fprintf('Gain of distillate mass =%8.3f\n', Change_msp)
plot(z(1,:),Tf2(1,:), '-',z(2,:),Tf2(2,:), '+',z(5,:),Tf2(5,:), '--',z(m,:),Tf2(m,:), '+-')
legend('1st layer','33% DS','50% DS','mth layer')
xlabel('Fiber length, m')
ylabel('Brine outlet temperature profile (Tf), K')
 plot(z(1,:),Tfm(1,:), '-',z(8,:),Tfm(8,:), '+',z(16,:),Tfm(16,:), '--',z(26,:),Tfm(26,:), '+-')
legend('1st layer','8th layer','16th layer','26th layer')
```

```
xlabel('Fiber length, m')
ylabel('Fiber outside wall temperature profile (Tfm), C')
plot(z(1,:),Tpm(1,:), '-',z(8,:),Tpm(8,:), '+',z(16,:),Tpm(16,:), '--',z(26,:),Tpm(26,:), '+-')
legend('1st layer','8th layer','16th layer','26th layer')
xlabel('Fiber length, m')
ylabel('Fiber inside wall temperature profile (Tpm), C')
plot(z(1,:),Tp(1,:), '-',z(2,:),Tp(2,:), '+',z(5,:),Tp(5,:), '--',z(m,:),Tp(m,:), '+-')
legend('1st layer','20% DS','50% DS','100% DS')
xlabel('Fiber length, m')
ylabel('Distillate outlet temperature profile (Tp), K')
plot(z(1,:),Tf2(1,:), '-',z(1,:),Tfm(1,:), '+',z(1,:),Tpm(1,:), '--',z(1,:),Tp(1,:), '+-')
legend('Tf','Tfm','Tpm','Tp')
xlabel('Fiber length, m')
ylabel('Temperature profile, K')
title('first layer')
 plot(z(m,:),Tf2(m,:), '-',z(m,:),Tfm(m,:), '+',z(m,:),Tpm(m,:), '--',z(m,:),Tp(m,:), '+-')
legend('Tf','Tfm','Tpm','Tp')
xlabel('Fiber length, m')
ylabel('Temperature profile, K')
title('last layer')
plot(z(1,:),Nv(1,:), '-')
legend('1st layer')
xlabel('Fiber length, m')
ylabel('Water vapor flux (Nv), kg/m^2.h')
```

APPENDIX E

GAS CHROMATOGRAPHY CALIBRATION

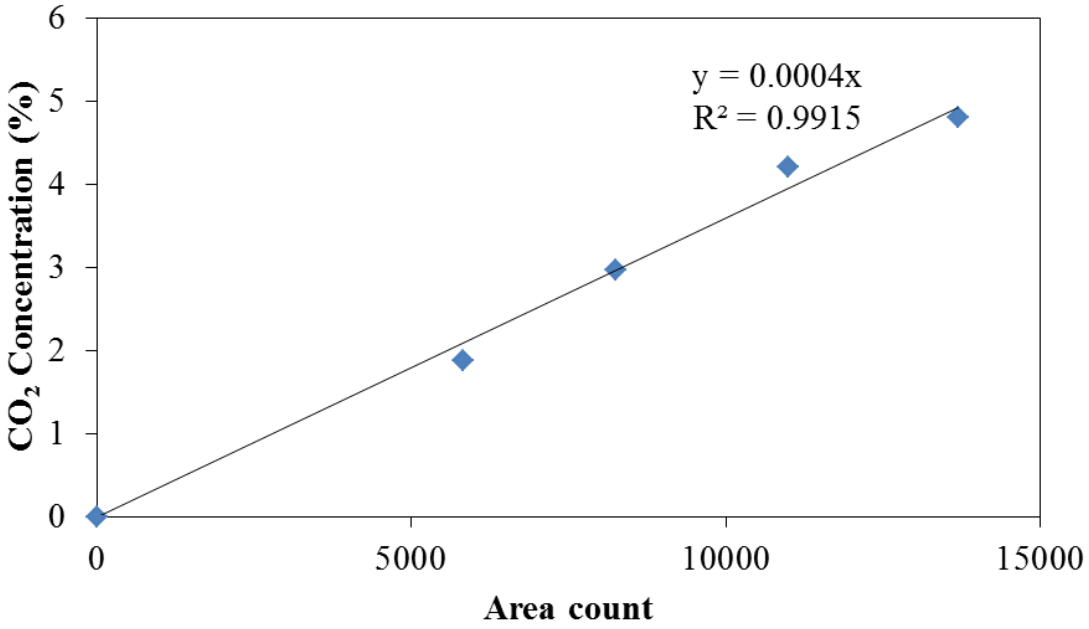

Figure E.1 Gas chromatography calibration (for Sub-section 2.2.2.4).

REFERENCES

[1] K.W. Lawson, D.R. Lloyd, Membrane distillation, J. Membr. Sci. 124 (1997) 1–25.

[2] B. Li, K.K. Sirkar, Novel membrane and device for vacuum membrane distillation-based desalination process, J. Membr. Sci. 257 (2005) 60–75.

[3] S. Bandini, C. Costoli, G.C. Sarti, Separation efficiency in vacuum membrane distillation, J. Membr. Sci. 73 (1992) 217–229.

[4] J.I. Mengual, M. Khayet, M.P. Godino, Heat and mass transfer in vacuum membrane distillation, Int. J. Heat Mass Transf. 47 (2004) 865–875.

[5] M. Khayet, Membrane distillation, in: N.N. Li, A.G. Fang, W.S.W. Ho, T. Matsuura (Eds.), Advanced Membrane Technology and Application, Hoboken, NJ: John Wiley, 2008: pp. 297–360.

[6] K.K. Sirkar, Other new membrane processes, in: W.S.W. Ho, K.K. Sirkar (Eds.), Membrane Handbook, New York, NJ: Van Nostrand Reinhold, 1992: pp. 885–912.

[7] M. Khayet, C. Cojocaru, A. Baroudi, Modeling and optimization of sweeping gas membrane distillation, Desalination 287 (2012) 159–166.

[8] R.R. Bhave, K.K. Sirkar, Gas permeation and separation by aqueous membranes immobilized across the whole thickness or in a thin section of hydrophobic microporous Celgard films, J. Membr. Sci. 27 (1986) 41–61.

[9] H. Chen, A. Kovvali, S. Majumdar, K.K. Sirkar, Selective CO_2 separation from CO_2−N_2 mixtures by immobilized carbonate−glycerol membranes, Ind. Eng. Chem. Res. 38 (1999) 3489–3498.

[10] B.R. Bodell, Silicone rubber vapour diffusion in saline water distillation, U.S. Patent Application Serial. No. 285,032, 1963.

[11] B.R. Bodell, Distillation of saline water using silicone rubber membranes, U.S. Patent Application Serial No. 3,361,645, 1968.

[12] M.E. Findley, Vaporization through porous membranes, Ind. Eng. Chem. Proc. Des. Dev., 6 (1967) 226-230.

[13] D.W. Gore, Gore-Tex membrane distillation, in: 10th Ann. Conf. Trade Fair Water Supply Improv. Assoc., 1982: pp. 1–10.

[14] E.A. Mason, G.M. Watson, Gaseous diffusion in porous media. III. thermal transpiration, J. Chem. Phys. 38 (1963) 1808–1826.

[15] E.J. Hoppinger, M. Altman, Experimental verification of the dusty-gas theory for thermal transpiration through porous media.pdf, J. Chem. Phys. 50 (1969) 2417–2428.

[16] E.A. Mason, A.P. Malinauskas, Gas Transport in porous media: the dusty-gas model, Amsterdam, Netherlands: Elsevier, 1983.

[17] R.W. Schofield, A.G. Fang, C.J.D. Fell, Gas and vapour transport through microporous membrane. I. Knudsen - Poiesuille transition, J. Membr. Sci. 53 (1990) 159–171.

[18] R.W. Schofield, A.G. Fane, C.J.D. Fell, Gas and vapour transport through microporous membranes. II. Membrane distillation, J. Membr. Sci. 53 (1990) 173–185.

[19] A. Ali, F. Macedonio, E. Drioli, S. Aljlil, O.A. Alharbi, Experimental and theoretical evaluation of temperature polarization phenomenon in direct contact membrane distillation, Chem. Eng. Res. Des. 91 (2013) 1966–1977.

[20] A. Tamburini, P. Pitò, A. Cipollina, G. Micale, M. Ciofalo, A Thermochromic Liquid Crystals Image Analysis technique to investigate temperature polarization in spacer-filled channels for Membrane Distillation, J. Membr. Sci. 447 (2013) 260–273.

[21] H. Yu, X. Yang, R. Wang, A.G. Fane, Analysis of heat and mass transfer by CFD for performance enhancement in direct contact membrane distillation, J. Membr. Sci. 405-406 (2012) 38–47.

[22] J. Gilron, L. Song, K.K. Sirkar, Design for cascade of crossflow direct contact membrane distillation, Ind. Eng. Chem. Res. 46 (2007) 2324–2334.

[23] J. Phattaranawik, R. Jiraratananon, A.G. Fane, Heat transport and membrane distillation coefficients in direct contact membrane distillation, J. Membr. Sci. 212 (2003) 177–193.

[24] M. Qtaishat, T. Matsuura, B. Kruczek, M. Khayet, Heat and mass transfer analysis in direct contact membrane distillation, Desalination. 219 (2008) 272–292.

[25] L. Song, B. Li, K.K. Sirkar, J.L. Gilron, Direct contact membrane distillation-based desalination: Novel membranes, devices, larger-scale studies, and a model, Ind. Eng. Chem. Res. 46 (2007) 2307–2323.

[26] H. Yasuda, J.T. Tsai, Pore Size of Microporous Polymer Membranes. J. Appl. Polym. Sci. 18 (1974) 805–819.

[27] J. Phattaranawik, R. Jiraratananon, A.G. Fane, Effect of pore size distribution and air flux on mass transport in direct contact membrane distillation, J. Membr. Sci. 215 (2003) 75–85.

[28] J. Woods, J. Pellegrino, J. Burch, Generalized guidance for considering pore-size distribution in membrane distillation, J. Membr. Sci. 368 (2011) 124–133.

[29] L. Song, Z. Ma, X. Liao, P.B. Kosaraju, J.R. Irish and K. K. Sirkar, Pilot plant studies of novel membranes and devices for direct contact membrane distillation-based desalination, J. Membr. Sci., 323 (2008) 257-270.

[30] R.W. Schofield, A.G. Fane, C.J.D. Fell, R. Macoun, Factors affecting flux in membrane distillation, Desalination. 77 (1990) 279–294.

[31] Cussler E. L., Diffusion: Mass Transfer in Fluid Systems, 3rd ed., New York, NY: Cambridge University Press, 2009.

[32] A.F. Mills, Mass Transfer, 2nd ed., Upper Saddle River, NJ: Prentice - Hall, 2001.

[33] T.E. Kohav, M. Sheintuch, D. Anvir, Steady state diffusion and reactions in catalytic fractal porous media, Chem. Eng. Sci. 46 (1991) 2787–2798.

[34] S.B. Warner, Fiber Science, Englewood Cliff, NJ: Prentice - Hall, 1995.

[35] C.A. Harper, Handbook of Plastics, Elastomers and Composites, 3rd ed., New York, NY: McGraw - Hill, 1996.

[36] D.R. Lide, CRC Handbook of Chemistry and Physics, 84th ed., Boca Raton, FL: CRC Press, 2003.

[37] E.E. Wilson, A basis of rational design of heat transfer apparatus, J. Heat Transfer. 37 (1915) 47–70.

[38] M. Khayet, T. Matsuura, J.I. Mengual, M. Qtaishat, Design of novel direct contact membrane distillation membrane, Desalination 192 (2006) 105–111.

[39] W.J. Thomas, M.J. Adam, Measurements of diffusion coefficients of carbon dioxide and nitrous oxide in water and aqueous solutions of glycerol, Trans. Faraday Soc. 61 (1995) 668–673.

[40] R.H. Perry, C.H. Chilton, Chemical Engineer's Handbook, 5th ed., New York, NY: McGraw-Hill, 1973.

[41] H. Lee, F. He, L. Song, J. Gilron, K.K. Sirkar, Desalination with acascade of cross-flow hollow fiber membrane distillation devices integrated with a heat exchanger, AIChE J. 57 (2011) 1780–1795.

[42] C. Cabassud, D. Wirth, Membrane distillation for water desalination: How to choose an appropriate membrane?, Desalination. 157 (2003) 307–314.

[43] J. Mericq, L. Stephanie, C. Cabassud, Vacuum membrane distillation of seawater reverse osmosis brines, Water Res. 44 (2010) 5260–5273.

[44] T. D. Dao, J.P. Mericq, S. Laborie, C. Cabassud, A new method for permeability measurement of hydrophobic membranes in vacuum membrane distillation process, Water Res. 47 (2013) 2096–2104.

[45] R.W. Schofield, Membrane distillation, Doctor of Philosophy Thesis, The University of New South Wales, Australia, 1989.

[46] E. Guillen-Burrieza, A. Servi, B.S. Lalia, H.A. Arafat, Membrane structure and surface morphology impact on the wetting of MD membranes, J. Membrane Sci. 483 (2015) 94–103.

[47] A.C.M. Franken, J.A.M. Nolten, M.H.V. Mulder, D. Bargeman, C.A. Smolders, Wetting criteria for the applicability of membrane distillation, J. Membrane Sci. 33 (1987) 315–328.

[48] R.B. Saffarini, B. Mansoor, R. Thomas, H.A. Arafat, Effect of temperature-dependent microstructure evolution on pore wetting in PTFE membranes under membrane distillation conditions, J. Membrane Sci. 429 (2013) 282–294.

[49] S. S. Kulkarni, E. W. Funk, Norman N. Li. 1992. Ultrafiltration, in W.S.W. Ho, K.K.Sirkar (Eds.), Membrane Handbook, New York, NY: VanNostrand Reinhold, pp. 885-912.

[50] R. Sheikholeslami, Fouling mitigation in membrane processes, Desalination, 123 (1999) 45–53.

[51] M.S. El-Bourawi, Z. Ding, R. Ma, M. Khayet, A framework for better understanding membrane distillation separation process, J. Membr. Sci. 285 (2006) 4–29.

[52] C.M. Tun, A.G. Fane, J.T. Matheickal, R. Sheikholeslami, Membrane distillation crystallization of concentrated salts-flux and crystal formation, J. Membr. Sci. 257 (2005) 144–155.

[53] S. Goh, J. Zhang, Y. Liu, A.G. Fane, Fouling and wetting in membrane distillation (MD) and MD-bioreactor (MDBR) for wastewater reclamation, Desalination 323 (2013) 39-47.

[54] M. Gryta, Effect of iron oxides scaling on the MD process performance, Desalination 216 (2007) 88–102.

[55] M. Krivorot, A. Kushmaro, Y. Oren, J. Gilron, Factors affecting biofilm formation and biofouling in membrane distillation of seawater, J. Membr. Sci. 376 (2011) 15-24.

[56] S. Goh, Q. Zhang, J. Zhang, D. McDougald, W.B. Krantz, Y. Liu, A.G. Fane, Impact of a bio-fouling layer on the vapor pressure driving force and performance of a membrane distillation process, J. Membr. Sci. 438 (2013) 140-152.

[57] G. Naidu, S. Jeong, S.-J. Kim, I.S. Kim, S. Vigneswaran, Organic fouling behavior in direct contact membrane distillation, Desalination 347 (2014) 230-239.

[58] B.J. Bellhouse, F.H. Bellhouse, C.M. Curl, T.I. MacMillan, A.J. Gunning, E.H. Spratt, S.B. MacMurray, J.M. Nelems. A high efficiency membrane oxygenator and pulsatile pumping system, and its application to animal trials. Trans Am Soc Artif Intern Organs. 19 (1973) 72-79.

[59] H. Bauser, H. Chmiel, N. Stroh and E. Walitza. Interfacial effect with microfiltration membrane, J. Membr. Sci. 11(1982) 321-332.

[60] P.M. Galletti, P.D. Richardson, L.A. Trudell. Oscillating blood flow enhances membrane plasmapheresis. ASAIO Trans 23 (1983) 279-282.

[61] S.M. Finnigan, J.A. Howell. The effect of pulsatile flow on ultrafiltration fluxes in a baffled tubular system. Chem. Eng. Res. Des. 67 (1989) 278-282.

[62] B.B. Gupta, B. Zaboubi, M.Y. Jaffrin. Scaling up pulsatile filtration flow methods to a pilot apparatus equipped with mineral membranes. J. Membr. Sci.80 (1993) 13-20.

[63] E. Goldberg, Handbook of Downstream Processing, London, UK: Blackie Academic & Professional, 1997.

[64] R. Singh, E. Hoffman and S. Judd, Membranes Technology Ebook Collection: Ultimate CD, Elsevier Science, 2008. DOI: http://store.elsevier.com/Membranes-Technology-ebook-Collection/Rajindar-Singh/isbn-9780080915357/

[65] P. Manno, P. Moulin 1, J.C. Rouch, M. Clifton and P. Aptel, Mass transfer improvement in helically wound hollow fibre ultrafiltration modules Yeast suspensions, Separation and Purification Technology, vol.14, pp. 175–182, 1998.

[66] F.He, K.K.Sirkar, J.L. Gilron, Studies on scaling of membranes in desalination by direct contact membrane distillation: $CaCO_3$ and mixed $CaCO_3/CaSO_4$ systems. Chem. Eng. Sci. 64(2009)1844-1859.